An improved signal model for a dual-phase xenon TPC using Bayesian inference and studies on the software trigger efficiency of the XENON1T DAQ system

vorgelegt von
Stefan Michael Schindler
geboren am 20. Juni 1984 in Mainz

Mainz, im September 2020

ii

1. Gutachter:
2. Gutachter:

Tag der mündlichen Prüfung: 21.01.2021

Für meine Eltern.

Erklärung

Hiermit versichere ich gemäß § 12 Abs. 3e der Promotionsordnung des Fachbereichs 08, Physik, Mathematik und Informatik der Johannes Gutenberg-Universität Mainz vom 02.12.2013:

- dass ich die vorgelegte Arbeit selbständig verfasst habe. Es wurden ausschließlich die angegebenen Quellen und Hilfsmittel verwendet. Von der Ordnung zur Sicherung guter wissenschaftlicher Praxis in Forschung und Lehre und vom Verfahren zum Umgang mit wissenschaftlichem Fehlverhalten habe ich Kenntnis genommen.

- dass ich die vorliegende Dissertation nicht als Prüfungsarbeit für eine andere Prüfung eingereicht habe.

- dass ich die vorliegende Abhandlung oder Teile davon noch nicht als Dissertation bei einer anderen Fakultät oder einem anderen Fachbereich eingereicht habe.

Mainz, den 31. August 2020

_____

Stefan Schindler

Abstract

Understanding nature has always been one of the most driving factors for mankind to invest huge amounts of effort and resources into research and development. The most fundamental questions have always been how the universe came to be and in what direction it will develop in the future. To answer these questions, we have to step back and first find the answer to the even more fundamental question: What exactly is our universe made of.

Recent experiments, like the Planck satellite mission [3], gave us already a sophisticated plan on what to expect of the composition of the universe. But even with today's advanced technology, where everybody carries around a powerful computer in his pocket in form of a smartphone, we are only able to grasp less than 5 % of the whole: Ordinary baryonic matter. While studying these ~5 % ordinary matter is still a very active field of research, there is already a rapidly growing community that tries to tackle the next question: What is the rest of the Universe made of and what is Dark Matter? With all the observational evidences being present, the science community has long accepted the fact, that there has to be a form of matter that has not been detected yet. It is also known, that it has a roughly 5 times higher abundance than ordinary baryonic matter. Discovering these next ~25 % would be a major step towards a more substantial understanding of how our universe developed since its sudden appearance after a big bang roughly 14 billion years ago.

This thesis has been written while being part of the XENON Dark Matter search project. This collaboration of scientists is on the hunt for Weakly Interacting Massive Particle (WIMP), one of the most promising candidates for Dark Matter, using time projection champers (TPCs) filled with liquid xenon (LXe). These ultra low background detectors are located in the underground facilities of the Laboratori Nazionali del Gran Sasso (LNGS) in Italy. The most recent generation is the XENON1T experiment, using a total 3.2 t of xenon and being equipped with 248 photo multiplier tubes (PMTs) used for measuring particle interactions through flashes of light. Right now, the commissioning of the next generation experiment XENONnT is already ongoing. It will use even more xenon, will be equipped with additional PMTs and even a novel neutron veto.

This work has two focus topics: First, the data driven determination of the software trigger efficiency of the XENON1T data acquisition (DAQ) system. It has been an important cross-check of the performance and adjustment of the software part of the DAQ system. The trigger efficiency is a main factor, that greatly influences the sensitivity of the detector. If the detector is tuned to be too sensitive in the wrong range, e.g. too much noise from coincidental dark counts would be recorded. On the other hand will a badly tuned efficiency lead to many missed low energy events, which is the main energy region WIMP interactions are expected. The second part of this work deals with the development of an improved signal model and a more general introduction of the signal efficiency together with an extended spatial signal dependence. Dealing with these topics, this work tries to add new pieces to the puzzle and support the efforts of the XENON collaboration to solve the mysteries of Dark Matter.

Zusammenfassung

Die Natur zu verstehen, war schon immer einer der treibenden Faktoren der Menschheit, um viel Aufwand und Ressourcen in Forschung und Entwicklung zu investieren. Eine der fundamentalsten Fragen ist hierbei wie das Universum entstand und in welche Richtung es sich entwickelt. Um diese Fragen zu beantworten, gilt es vorher anzusetzen und die noch fundamentalere Frage zu stellen: Aus was besteht unser Universum überhaupt?

Jüngste Experimente, wie die Planck Satelliten-Mission [3], haben bereits einen Einblick gegeben, wie die Zusammensetzung des Universums beschaffen ist. Aber sogar mit der modernen Technik von heute, in der jeder einen Computer in Form eines Smartphones bei sich trägt, ist man bisher nur in der Lage ca. 5 % des Ganzen zu begreifen; gewöhnliche baryonische Materie. Während die Erforschung dieser 5 % immer noch ein aktives Forschungsfeld darstellt, gibt es mittlerweile eine schnell wachsende Community, die bereits versucht die nächste Frage zu lösen: Aus was besteht der Rest des Universums und welche Rolle spielt die Dunkle Materie? Auf Grundlage der kosmischen Beobachtungen, ist es in der Wissenschaft eine anerkannte Tatsache, dass es eine noch unbekannte Form der Materie geben muss, die eine fünf Mal höhere Abundanz als normale baryonische Materie aufweisen muss. Diese nächsten ~25 % zu entdecken wäre ein großer Schritt in Richtung eines grundlegenderen Verständnisses, wie sich das Universum seit seiner plötzlichen Entstehung nach dem Big-Bang, vor ungefähr 14 Milliarden Jahren, entwickelt hat.

Die vorliegende Arbeit wurde als Teil des „XENON dark matter search projects" angefertigt. Diese Kollaboration von Wissenschaftlern ist auf der Suche nach WIMPs, einem der erfolgversprechendsten Kandidaten für Dunkle Materie. Hierzu werden mit flüssigem Xenon (LXe) gefüllte Zeitprojektionskammern (TPCs) mit besonders geringem Hintergrund genutzt, die sich im Untergrundlabor Laboratori Nazionali del Gran Sasso (LNGS) in Italien befinden. Die aktuellste Generation ist das XENON1T Experiment, mit einer Masse von insgesamt 3.2 t Xenon und 248 Photosensoren (PMTs), die die während der Teilchen-Interaktionen entstehenden Lichtblitze detektieren. Derzeit findet bereits der Aufbau des Nachfolgeexperiments XENONnT statt. Es wird eine noch höhere Masse an Xenon nutzen, mit noch mehr Photosensoren ausgestattet sein und darüber hinaus ein neu entwickeltes Neutronen-Veto besitzen.

Die Arbeit behandelt zwei Schwerpunkte: Zum einen, die datengetriebene Auswertung der Software-Trigger Effizienz des XENON1T Datennahme-Systems (DAQ). Diese Studie liefert einen wichtigen Cross-Check über die Leistung und Einstellung des Systems, da die Trigger-Effizienz ist ein maßgeblicher Faktor für die Sensitivität des Detektors ist. Ist der Detektor falsch abgestimmt, werden unter Umständen wichtige Events im unteren Energiebereich verpasst (hier werden die WIMP Interaktionen erwartet), oder es wird zu viel Hintergrund gemessen, z. B. Koinzidente Dark-Counts. Zum anderen, befasst sich die Arbeit mit der Entwicklung eines verbesserten Signal-Modells in Verbindung mit einer grundlegenderen Behandlung der Signal-Effizienzen und der erweiterten Ortsabhängigkeit des Signals. Die Studien in dieser Arbeit versuchen dem Puzzle ein weiteres Teil hinzuzufügen und unterstützen hierbei auch die Anstrengungen der XENON Kollaboration das Mysterium der Dunklen Materie aufzulösen.

Contents

Introduction and Motivation

Solving the mystery of Dark Matter is a very active field of research. While being five times more abundant than ordinary matter, little is known about its true nature. But there is one thing the majority of the science community is sure of: Dark Matter has to be there, since too many cosmological and astrophysical observations have been made, to be ignored. Multiple models and detection principles have been developed to explain and detect dark matter. Using direct detection and liquid xenon (LXe) filled time projections chambers (TPCs) is one of these approaches. The Weakly Interacting Massive Particle (WIMP), one of the most promising DM candidates, has a small but finite chance to interact with the target material in the detector by creating a small flash of light, which can be detected. To better understand these detectors physically and on the other hand also helping to further develop the model of the expected signal response theoretically, will both be part of this thesis.

This thesis is outlined as follows: Chapter 1 will lay the foundations for the studies of Dark Matter (DM) by looking at observational evidences and the classification of different types of DM in sections 1.1 and 1.2. The Weakly Interacting Massive Particle (WIMP) will be introduced in section 1.4 as the DM candidate of interest throughout this work. The chapter closes by discussing different detection principles, focusing on direct detection, including its theoretical background in section 1.5. The XENON Dark Matter project and its detectors, will be the topic of chapter 2. Here the detection principle of time projection chambers (TPCs) using Liquid xenon (LXe) as the detection medium will be discussed, see sections 2.1 and 2.2. Two different generations of the detectors used by the XENON collaboration, the XENON100 experiment in 2.3 and XENON1T experiment in 2.4, will be presented. A special emphasis will be put on the data acquisition system (DAQ) of the XENON1T experiment in section 2.4.1, since chapter 4 will be dealing with the analysis of the software trigger part of the system. Before coming to the second main topic of this work, chapter 3 introduces Bayesian statistics. It reviews the fundamental (sometimes philosophical) differences between these two most popular approaches to statistics: The frequentist and the Bayesian formulation. Bayes' theorem is derived as a consequence of conditional probability and the application of using it for parameter estimation is shown in preparation to the later chapters.

The first main study, the data driven determination of the software trigger efficiency is performed in chapter 4. A detailed guide of the cleaning and wrangling of the detector data is given in section 4.1, as a preparation to be able to perform the later analysis. After looking at different aspects and comparing different data taking periods, the resulting efficiency is compared to a simulation driven study in section 4.2.

The second focus topic is separated into two chapters. In chapter 5, an improved signal model is developed. While maintaining the spatial signal information in the model

where possible, see sections 5.1 and 5.2, the detector efficiencies are implemented into the model in a novel Bayesian manner, see section 5.3. Finally, chapter 6 deals with performance studies of the previous introduced and improved model. After explaining how signal events are generated in section 6.1, the Bayesian implementation of the efficiency is verified with a Markov chain Monte Carlo (MCMC) study in section 6.2. In section 6.3 the capability of reconstructing the Dark Matter parameters of interest (WIMP mass m_χ and cross-section σ_χ), only having the signal information at hand, is performed. To conclude this chapter, an upper limit for a background-free experiment is calculated in section 6.4.

Chapter 1

Evidences and Theoretical Background of Dark Matter

This first chapter lays the foundations for what is to come in the following ones. After having a look at observational evidences and classification of DM in sections 1.1 and 1.2 we will have a closer look on how to describe it in form of a new particle and introduce the Weakly Interacting Massive Particle (WIMP) in section 1.4. After that, the different detection principles are discussed, focusing on direct detection, including its theoretical background in section 1.5.

1.1. Observational Evidences

To start off, selected astronomical observations are discussed, which can be explained naturally with the introduction of DM. Observations that were recorded decades ago, e.g. the study of the velocity distribution of stars and gas clouds inside of spiral galaxies, gravitational lensing, as well as very recent ones like the millennium simulation, showing how DM influenced the structure formation of the early universe will be reviewed. The final and probably most important observation that has been refined in the last years is the Cosmic Microwave Background (CMB) and its contribution to define and confirm the standard model of big bang cosmology: The Λ-Cold Dark Matter (ΛCDM) model.

1.1.1. Spiral Galaxies

One of the most striking evidences has already been observed in the 1970s. During the spectroscopic measurements of red-shifts to study the velocity of light-emitting objects within spiral galaxies, Vera Rubin et. al [82] noticed a strange behavior. According to Kepler's law, the radial dependent velocity within an isotropic mass distribution should follow the equation

$$v(r) = \sqrt{G\frac{M(r)}{r}} \tag{1.1}$$

where

$$M(r) = 4\pi \int_0^r \rho(r')r'^2 \mathrm{d}r' \tag{1.2}$$

is the mass contained within a radius r that follows the density profile $\rho(r)$. If the majority of the galaxy's mass is contained in the visible parts of the rotating galaxy, the expected velocity distribution $v(r)$ has to fall off towards the edges of the galactic disk as $1/\sqrt{r}$. But this is not what has been observed. As an example, the measured velocity distribution of the spiral galaxy NGC6503 is shown in figure 1.1. The measurements show an almost radius independent behavior at the outer edge of the galaxy. This leads to the conclusion that there should be further invisible mass hidden within radius r that provides the additional gravitational pull to keep the galaxy from dispersion.

Furthermore, the shape an additional mass contribution would have can be deduced. Since the velocity stays constant for outer radii, the mass profile $M(r)$ needs to be proportional to r. This in turn leads to the conclusion that the mass density distribution follows $\rho \propto 1/r^2$ and therefore infers a spherical mass distribution. It is proposed that a spherical halo of DM exists, that extends far beyond the boundaries of the galaxy itself [83].
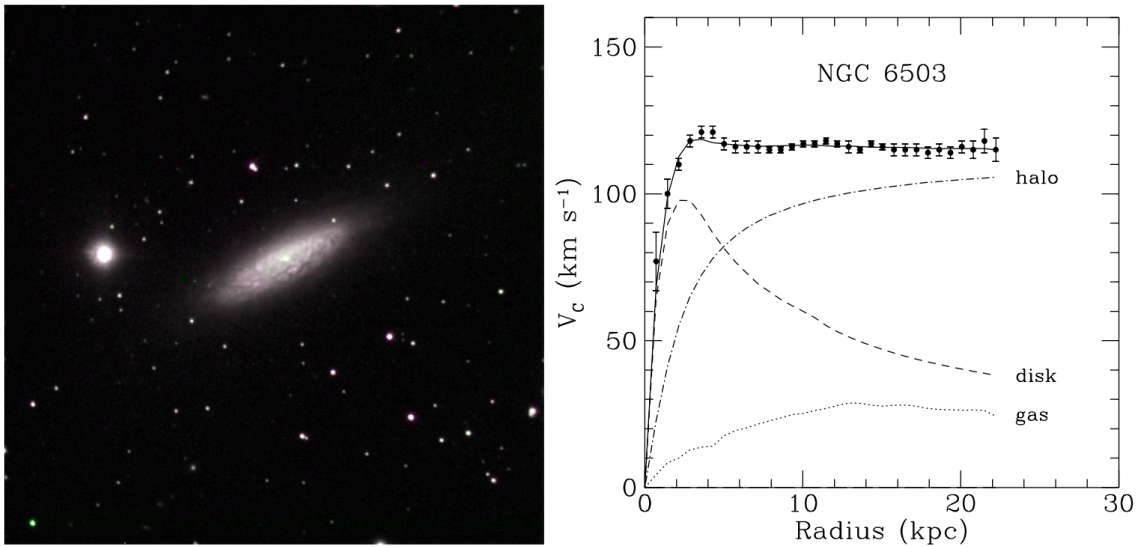
Figure 1.1.: Left: Picture of the dwarf galaxy NGC6503 in the visible light spectrum. Right: rotation speed curve of the same galaxy [21]. The measured data can not be explained by only considering a model with a disk-like (dashed) or gaseous (dotted) mass distribution. By adding a third component, i.e. a halo of DM (dashed-dotted) the data can be explained (solid). (image courtesy of NASA)

1.1.2. Gravitational lensing

A different observation, which also leads to a missing mass problem, is gravitational lensing. Analogous to geometric optics where light is bend during the transition of two different media with different refraction indices, it also gets bend in the presence of massive objects e.g. galaxies, galaxy clusters or black holes while passing their gravitational

field [41]. Figure 1.2 illustrates this effect: For an observer on earth, a distant galaxy seems to be showing up at two positions in space at the same time. This can be explained by a massive object (in this particular case a Quasar) sitting between the observer and the object. The observed object that should be hidden by the massive object in between becomes visible due to the bend path the light is guided on.
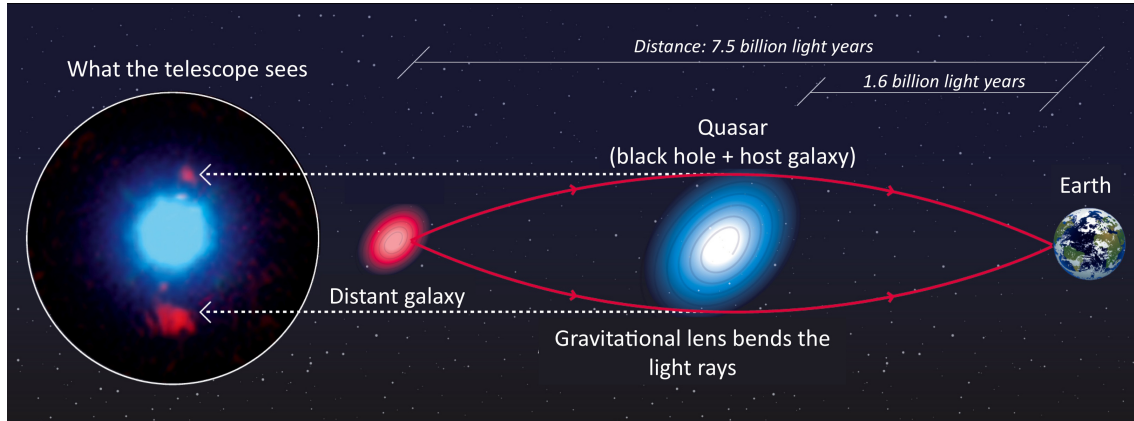
Figure 1.2.: Illustration of gravitational lensing. Light is bend in the presence of massive objects similar to geometrical optics. The object observed from earth seems to appear in two places at once due to the curvature of space-time. (Image credit: F. Courbin et al., Caltech/EPFL/WMKO)

Using this technique, one is able to measure the mass distribution at very large scales compared to a single galaxy, even the mass of whole galaxy clusters can be studied. In the meantime several surveys, e.g. [49] show a consistent results for the mass density profiles of numerous galaxies that all follow the dependence $\rho(r) \propto 1/r^2$.

1.1.3. Cosmic Microwave Background

The evidences discussed so far do not allow to make assumptions on the total amount of DM in the universe. We will see how to extract this information from the analysis of the CMB. In 1964 two radio-astronomers Penzias and Wilson discovered the CMB by a mere accident [77].

The CMB is a relic radiation that was produced around 380000 years after the big-bang, when the universe first became transparent for photons. It is an almost perfect black-body radiation with a temperature of $T = 2.72\,\text{K}$ [35]. It is measured by estimating the relic photons energy. With increasing precision, experiments like the WMAP [58] mission and most recently the Planck satellite mission, [3] revealed small spatial correlated anisotropies in the temperature distribution in the order of $10^{-5}\,\text{K}$ as shown in figure 1.4. The correlation is best visualized as a decomposition of the temperature spectrum into spherical harmonics which is basically a measure for how big the patches of the anisotropies are:

$$\Delta T(n) = \sum a_l^n Y_l^m(n), \tag{1.3}$$

or expressed as an energy power spectrum

$$\mathcal{D}_l = \frac{1}{2l+1} \sum |a_l^m|. \tag{1.4}$$

The power spectrum $\mathcal{D}_l$, dependent on the multi-pole moment l, see figure 1.5, and shows several peaks. The first peak corresponds to the acoustic baryon-photon density oscillation scale in the early universe at the time of decoupling of baryons and photons. The oscillation is a result of the competition between gravitational pull and radiation pressure. Using the first peak, one can deduce information on the curvature of the universe while the ratio between the first and the second peak yields the baryon density in the universe. Finally, the DM density can be calculated by including the the third peak into the calculations.

All this information combined yields the most accurate result of the composition of our universe as of today. Using the parameters from table 1.1 extracted from the most recent Planck publication, see table 4 in [79], as a result we get a composition of the universe as shown in figure 1.3. Our universe, as we know it today, is dominated by Dark Energy (68,5 %), followed by Dark Matter (26,6 %) that itself is roughly 5 times more common than the ordinary baryonic matter (4.9 %).
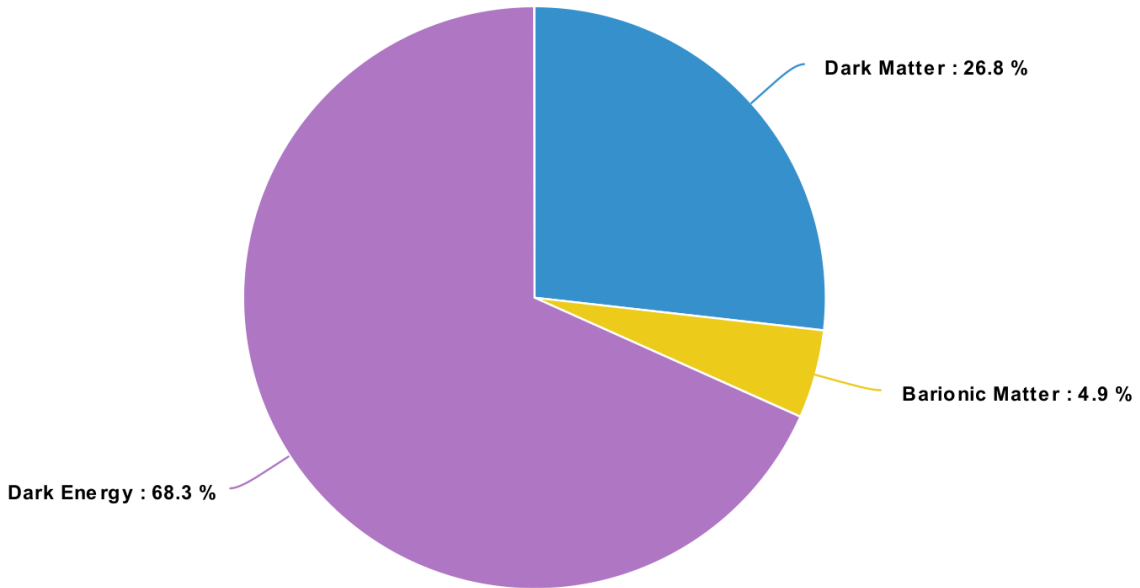

Figure 1.3.: Pie-chart of the universes energy composition as deduced from the analysis of the most recent Planck satellite mission published in 2016. The dominating part is Dark Energy with 68,5 %, followed by DM with 26,6 % and finally "normal" baryonic matter with 4.9 %.

Table 1.1.: Selected parameters and their 68 % confidence limits for the base ΛCDM model from the Planck power spectrum (see figure 1.5). The values were taken from the most recent Planck publication, see table 4 in [79].

Parameter	68 % confidence limits
Ω_λ	0.685 ± 0.013
Ω_m	0.315 ± 0.013
$\Omega_c h^2$	0.1197 ± 0.0022
$\Omega_b h^2$	0.02222 ± 0.00023
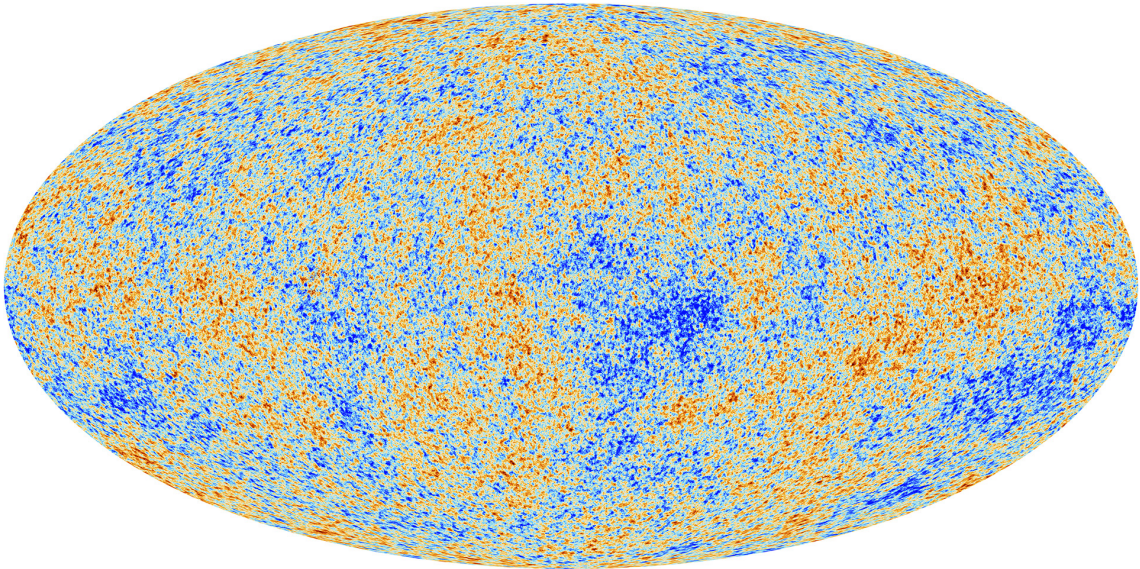
Figure 1.4.: The Cosmic Microwave Background as measured by the Planck satellite mission in 2013. The color scale representing the fluctuations reaches from $-500\,\mu K$ (blue) to $500\,\mu K$ (red) with respect to the CMB temperature of 2.72 K. (Credit: ESA and the Planck Collaboration [42])

1.2. Classification of Dark Matter

Possible DM candidates are depending on the chosen scenario of the universes development. A decision which scenario to pursue has to be made by choosing three possible schemes: The Hot, Warm and the Cold Dark Matter scheme.

Adiabatic density fluctuations are caused by inflation of the expanding universe. Perturbations of small amplitude are following a simple power-law $P(k) \propto k^n$ with spatial frequency k and grow during the expansion. They are regulated by the radiation in the early universe and later by DM. The growth is slowed down during the radiation dominated era as the density fluctuations are encompassed by the cosmological particle horizon. This effect is called the Meszaro effect [70]. A characteristic scale is imprinted, that corresponds to the horizon at the time the universe became matter dominated and

Figure 1.5.: The Planck 2015 temperature power spectrum. The best-fit ΛCDM theoretical spectrum fitted to the Planck likelihood is plotted in the upper panel. Below, the residuals with respect to this model are shown. The error-bars represent the $\pm 1\,\sigma$ uncertainties [79].

for larger k (smaller scales) the power-law bends to $P(k) \propto k^{n-3}$. Caused by random thermal motions, the DM fluctuations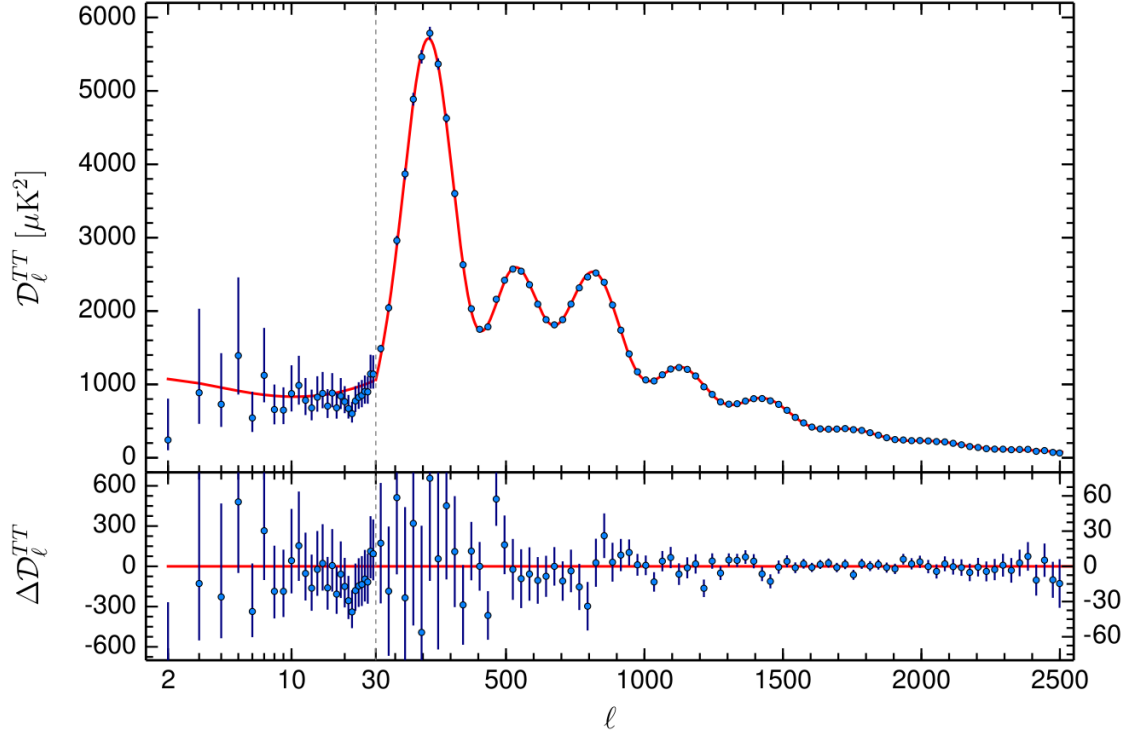 are washed out below a free-streaming scale corresponding to the typical co-moving distance a particle travels in the corresponding age of the universe. This effect varies inversely proportional to the mass of the particle, $\lambda_{fs} \propto 1/m_\chi$ [48]. The free streaming scale directly connects the possible size of structures that can form depending on the mass of the assumed particles. The Hot Dark Matter (HDM) scenario is described by a relativistic equation of state preferring light & relativistic particles with masses of around $m_\chi = 30\,\text{eV}$, whereas the mass for Warm Dark Matter (WDM) is already in the range of $m_\chi = 2\,\text{keV}$. Cold Dark Matter (CDM) follows a non-relativistic equation of state based on heavy & non-relativistic moving particles with around $m_\chi = 100\,\text{GeV}$ [17, 48].

Assuming the CDM approach and its free-streaming scale, first sub galactic structures with the size of planets were formed. For WDM the first structures were in order of the DM halos of dwarf galaxies. Finally the structure scale of HDM is in the order of galaxy super-clusters. Starting with small structures, like for the case of CDM and growing into bigger formations by merging and accretion is called *bottom-up-scenario* [28]. On the other

hand, starting with the scale of super clusters and fragmenting into smaller formations, like in the HDM case, is named *top-bottom-scenario*.

Results of experiments like the Sloan Digital Sky Survey (SDSS) [49]), the 2dF Galaxy Redshift Survey (2dFGRS) [36] or the Center for Astrophysics (CfA) redshift survey [50], which produced a catalog of the galaxy distribution of parts of our universe, are compared to N-Body simulations like the Millennium simulation [87]. Figure 1.6 illustrates these results.

A comparison favors the scenario of CDM together with the introduction of a cosmological constant λ that makes up for the huge amount of Dark Energy. Today's standard model of cosmology is the therefore called the Λ-Cold Dark Matter (ΛCDM) model.

1.3. Alternative Models Without Dark Matter

To promote a new unknown form of matter is not everybody's favorite way of dealing with the problem of missing mass. There are many theories that aim to explain the experimental results, by e.g. searching for massive objects that couldn't be detected so far (e.g. Massive Astrophysical Compact Halo Objects (MACHOs)) or simply by changing Newton's law of gravitation (MOdified Newtonian Dynamics (MOND)).

1.3.1. MOdified Newtonian Dynamics (MOND)

The seemingly simple proposal by Milgrom [71] has some far reaching consequences: If instead of following Newton's law of gravitation,

$$F = m \cdot a \tag{1.5}$$

would rather scale as

$$F_{\text{MOND}} = m \cdot \frac{a^2}{a_0} \tag{1.6}$$

then, for small accelerations ($a \ll a_0 \sim 1.2 \cdot 10^{-10}\,\text{m/s}^2$), it would be possible to explain the observed behavior of gas and stars in rotational galaxies without introducing a new or hidden form of matter. This has been the start of a new framework for gravity and dynamics not obeying Newtonian physics or even general relativity [23].

There have also been relativistic approaches trying to avoid DM but they failed to e.g. explaining gravitational lensing effects. This wasn't satisfactorily solved until 2004 when Bekenstein first proposed a realistic solution [22]. Bekenstein TeVeS (Tensor-Vector-Scalar) theory is potentially flexible enough to not only tackle the problem of gravitational lensing but also the remaining problems of structure formation and the CMB. Yet, there are still observations like the bullet-cluster [31] that challenges existing MOND theories.

1.3.2. Massive Astrophysical Compact Halo Objects (MACHOs)

There is also the possibility that missing mass could be be found in compact not yet discovered non-luminous baryonic matter. Possible candidates that fall into this category
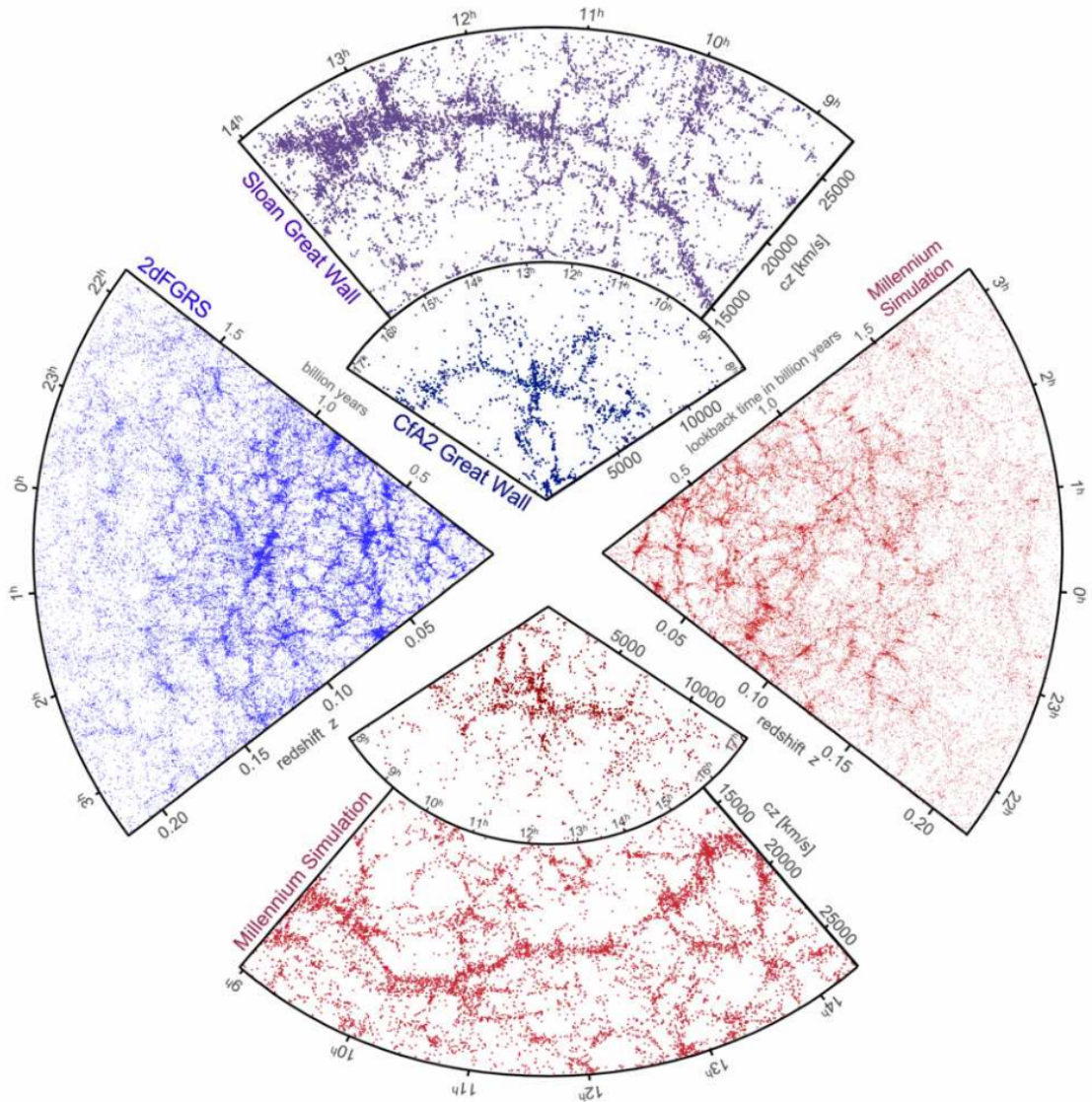
Figure 1.6.: The galaxy distribution obtained from spectroscopic redshift surveys and from mock catalogs constructed from cosmological simulations. The slice at the top shows the CfA2 "Great Wall". Drawn to the same scale is a small section of the SDSS, in which an even larger "Sloan Great Wall" has been identified. The wedge on the left shows one-half of the 2dFGRS, which determined distances to more than 220,000 galaxies in the southern sky out to a depth of 2 billion light years. At the bottom and on the right, mock galaxy surveys constructed from the "Millennium" simulation are shown with matching survey geometries and magnitude limits [87].

are planets, gas giants, brown dwarfs, white dwarfs, neutron stars and black holes. These objects are called Massive Astrophysical Compact Halo Objects (MACHOs).

One of the experiments to investigate the feasibility of MACHOs could be a gravitational micro-lensing surveys as run by the EROS collaboration. The EROS collaboration set an upper limit of 8 % on the halo mass fraction of MACHOs after 6.7 years of collecting data. This means, that at least in the Milky Way's halo, MACHOs would not be dominating the missing mass [62, 92]. Undiscovered MACHOs, like primordial black holes, could provide the necessary mass to explain observed phenomena (velocities of spiral galaxies or the Bullet Cluster). But this is rather unlikely, especially as such objects would contradict CMB results as they consist of baryonic matter.

1.4. Particle Dark Matter

After getting to know some alternative models that try not introduce an additional unknown form of matter, in the next few sections the focus will be on DM and its different possible particle candidates.

Cosmological observations yield some basic requirements that these particles have to fulfill:

- Only gravitational and weakly interacting

- Particles are neutral, carry no charge and do not experience electromagnetic or strong interaction

- Stable or at least very long lived particles

1.4.1. Weakly Interacting Massive Particles

Taking all evidences together, there is a whole class of new particles that all would be possible candidates: Weakly Interacting Massive Particles (WIMPs).

Its name already covers the main attributes the particles should have: They have to be massive i.e. interacting with gravitation and in addition also have to be weakly interacting. Following the ΛCDM model and the recent CMB results [79] the fraction of DM in the universe should be about 27 % of the whole energy, so most of the matter has to be non-baryonic matter. If WIMPs were in thermal equilibrium in the hot early universe, their abundance can be approximated by

$$\Omega_\chi h^2 \approx 2.74 \cdot 10^8 \cdot Y_\chi(x_0) \, \frac{m_\chi}{1\,\text{GeV}} \propto 10^{-27} \, \frac{\text{cm}^3 \text{s}^{-1}}{\langle \sigma_A v \rangle} \tag{1.7}$$

where $Y_\chi(x_0)$ is the current number density of DM species χ and $x_0 = m_\chi / T_0$ an independent variable, which increases with growing time since the temperature of the universe decreases. The index 0 denotes the present temperature of the CMB at $T_0 = 2.73\,\text{K}$ and m_χ the assumed WIMP mass. Taking the standard ΛCDM model into account, WIMPs would decouple from the thermal plasma in the still radiation dominated early universe at a

freeze-out temperature T_F after the annihilation rate drops below the Hubble expansion rate H. In figure 1.7 the dependence of (1.7) on x is shown, assuming a WIMP mass of $m_\chi = 100\,\text{GeV}$ for three different different freeze-out temperatures (red, green and blue line). Since the mass dependence is very small on the logarithmic scale, it is neglected most of the time [39, 88, 61]. One can see that the higher the annihilation cross-section σ_A is, the smaller the relic abundance can be, since the WIMPs can stay longer in thermal equilibrium.

A remarkable aspect of this result is the striking consistency with the annihilation cross-section of a new particle with a weak scale interaction, which happens to be in the same order of magnitude. This coincidence is known as the *WIMP-miracle* [45].
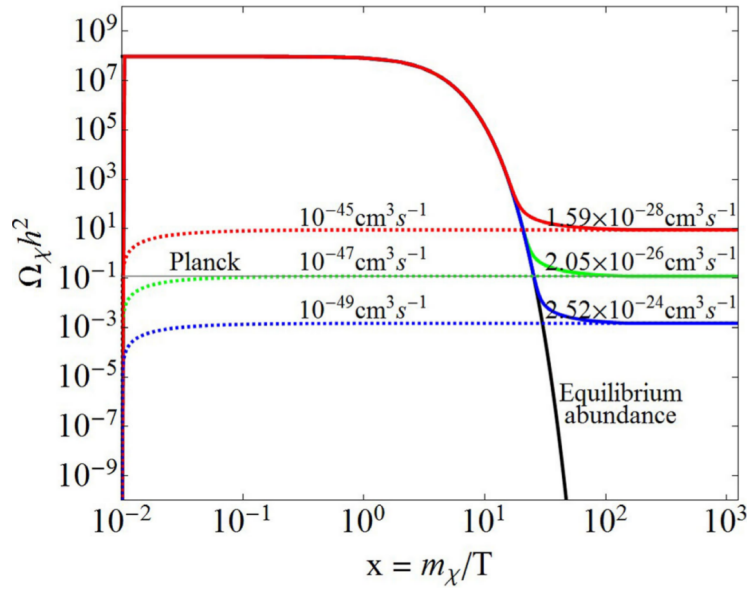
Figure 1.7.: Dependence of the current relic abundance on the annihilation rate for thermal DM that has frozen out (solid lines) for a WIMP mass of $m_\chi = 100\,\text{GeV}$. The black solid line corresponds to the equilibrium abundance. The dotted lines represent the freeze-in scenario which is not discussed in the scope if this work [39]

1.4.2. Dark Matter Particle Candidates

Supersymmetry

Supersymmetry (SUSY), being a possible extension to the standard model of particle physics, is one approach that can provide the needed particles. In SUSY every particle has its supersymmetric partner (every fermion has a supersymmetric bosonic partner and vice versa). The partner can also have a different mass compared to the Standard Model particle (broken symmetry). A SUSY particle that cannot decay into a normal particles should be

a stable Lightest Supersymmetric Particle (LSP). The LSP in this theory, called neutralino, would make an excellent WIMP candidate.

Neutrinos

The only particle in the standard model of particle physics that satisfies all characteristics of a DM particle out of the box is the neutrino. After discovering that it has a non zero mass, it became a natural candidate. However, using a laboratory constraint on the neutrino mass from e.g. Troitsk or Mainz (see e.g. [95]) at 95 % Confidence Limit (CL) of

$$m_\nu < 2.05\,\text{eV} \tag{1.8}$$

and predicting the relic neutrino density following

$$\Omega_\nu^2 = \sum_{i=1}^{3} \frac{m_i}{93\,\text{eV}}, \tag{1.9}$$

where m_i is the mass of the i-th neutrino flavor, this applies an upper bound to the total neutrino relic density of

$$\Omega_\nu^2 \leq 0.07. \tag{1.10}$$

This means the abundance of neutrinos is simply not enough to be the dominant part of DM in our universe.

In addition, observations and calculations showed that neutrinos cannot explain the Universe's large scale structure. Today neutrinos are part of the HDM (relativistic) scenario. Nevertheless they provided an important template for the class of hypothetical particles, the Weakly Interacting Massive Particles (WIMPs) [23].

A different more exotic species of neutrinos is still a possible DM candidate: The sterile neutrino. It has been proposed by Widrow [40] and follows a simple scenario: There could be an additional neutrino flavor that, without the electro-weak interactions experienced by standard model neutrinos, makes up a part of the DM. Aside from gravity, it only interacts through a small mixing angle with the other neutrinos. Such a particle would never have been in thermal equilibrium in the early universe. It would be a product of the oscillations of the other neutrino species. Depending on their mass, such neutrinos could be produced in a wide range of temperatures and thus either contribute to warm ($m_{\nu_s} \sim$ keV) or cold ($m_{\nu_s} \gg$ keV) DM [23].

Axions

Axions are postulated particles that emerge from the attempt to solve the strong-CP problem of Quantum Chromo Dynamics (QCD) by introducing a new global $U(1)$ symmetry that is spontaneous broken [76]. The culprit is the term

$$\mathcal{L}_{\text{QCD}} \subset \bar{\Theta} \frac{g^2}{31\pi^2} G^{a\mu\nu} \tilde{G}_{a\mu\nu} \tag{1.11}$$

of the QCD Lagrangian. Here $G^{a\mu\nu}$ is the gluon field strength tensor and $\bar{\Theta}$ is related to the phase of the QCD vacuum. Later, Weinberg [94] and Wilczek [97] independently came to the conclusion that this implies the existence of a new particle.

Various measurements (e.g. stellar cooling, supernova SN1987A) already constrain the axion mass to be very light and in addition they are also expected to be very weakly interacting with baryonic matter [24]. Although the calculation of the relic density of axions is very uncertain, depending on the production mechanism, there is still a range where axions fulfill all constraints of being a possible DM candidate [81].

1.5. Direct Detection

With the evidence gathered so far (e.g. 1.1.1), we can assume that our planet moves through a halo of DM. There are different Models describing the distribution of DM in our galaxy. This work will focus on the usual Standard Halo Model (SHM) with the assumption of an isotropic and spherical distribution of DM whith its center in the Milky Way's core. The density is only dependent on the distance to the galactic center. As the galaxy is rotating, normal matter and DM is inter-penetrating the whole time. Because of the very small cross-section the interaction rate is expected to be very low. There are three possible channels experiments can use for the search of DM. These channels are illustrated in figure 1.8. Accelerators can be used to produce DM by colliding standard model particles, it can be detected indirectly by studying its Standard Model (SM) secondary particles from DM annihilation, scattering or decay. Finally, one can also use direct detection by measuring scatter rates. The focus of this work will be on the direct detection and the following sections will give an overview in how to calculate the expected scatter rates. As a reference for the following calculations see [63] if not mentioned otherwise. For more information on production or indirect detection, see the later section 1.6.
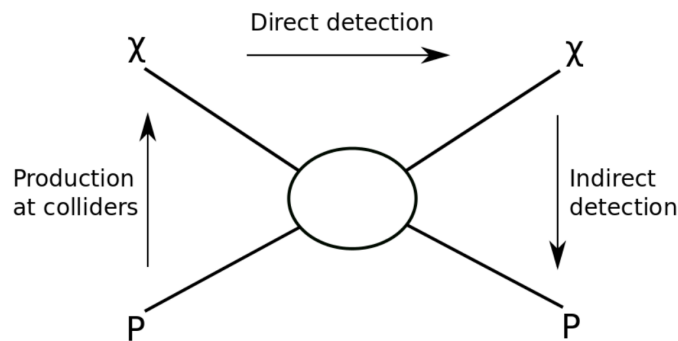

Figure 1.8.: Schematic representation of the different detection channels. DM can either be produced by colliding two SM particles, it can be detected directly by measuring scatter rates of a DM particles scattering of SM particles or it can be detected indirectly by measuring the SM secondary particles produced by e.g annihilation of two DM particles [93].

In direct detection itself, there are different techniques utilizing different physical channels for the detection, see figure 1.9 for example. Most of the Experiments are using two of the channels simultaneously e.g. to increase the discrimination power of different particle interactions, see e.g. chapter 2.2 for the utilization of the light and charge channel in a dual-phase time projection chamber (TPC).
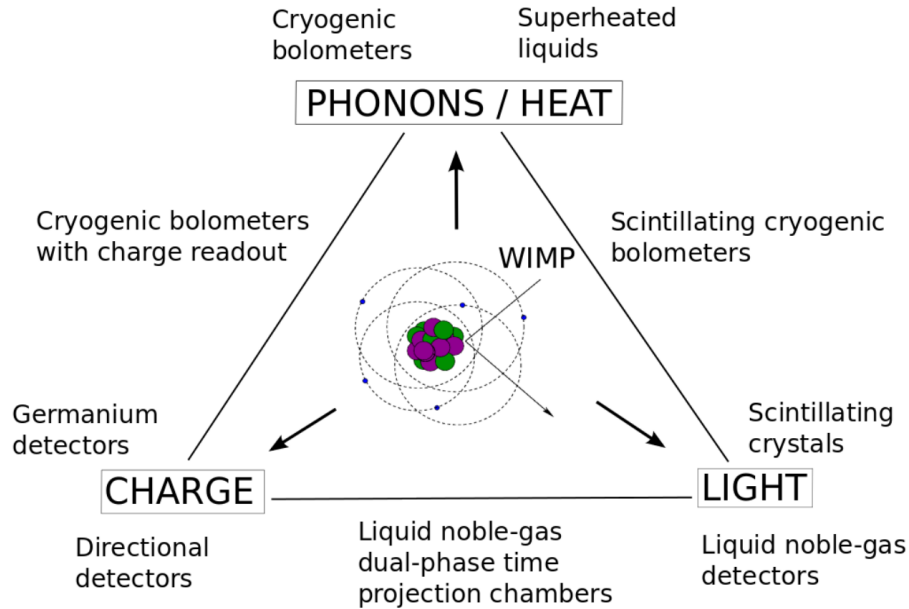

Figure 1.9.: Schematic of possible detection channels that can be measured in direct detection depending on the technology used in the different experiments [93].

1.5.1. Standard Halo Model

Considering an isotropic and spherical density distribution of DM and the radial distance of our solar system to the galactic center, the local DM density according to the standard scenario is assumed to be

$$\rho_D \approx 0.3 \, \frac{\text{GeV}}{c^2 \cdot \text{cm}^3} \tag{1.12}$$

at our spatial position in the galaxy on planet earth [27]. To counter gravity and to provide an equilibrium state DM will not be stationary, the matter has to be in motion and will have a velocity distribution itself. A simple Maxwell-Boltzmann velocity distribution

$$f(\vec{v}, \vec{v}_e(t)) \propto \exp\left(-\left(\frac{\vec{v} - \vec{v}_e(t)}{v_0}\right)^2\right) \tag{1.13}$$

is assumed for the standard model where $\vec{v}$ is the WIMP velocity relative to the target and $\vec{v}_e(t)$ is the velocity of earth ($\vec{v}$ is a 3-dimensional velocity vector) while $v_0 = 220 \, \text{km/s}$ is a reference velocity. To still be gravitationally bound in the potential of the galaxy, the

particle velocity has to have an upper limit. Above this escape velocity $v_{esc} = 544\,\frac{km}{s}$ particles are no longer bound and can escape the galaxy into intergalactic space. The DM halo itself is not supposed to rotate in the galactic rest frame so the sum of all particle velocities has to be zero.

Earth is not only moving around the galactic center but as any planet within a solar system, it also moves around its central star. In the galactic frame earth's velocity can be split into two parts

$$\vec{v}_e(t) = \vec{v}_\odot + \vec{v}(t)_\oplus \tag{1.14}$$

where $\vec{v}_\odot$ is the velocity of the sun around the galactic center and $\vec{v}(t)_\oplus$ describes the movement of the earth around the sun. In particular, earth's motion around the sun can be further broken down to

$$\vec{v}(t)_\oplus = v_\oplus \left[\epsilon_1 \cos(\omega(t - t_1)) + \epsilon_2 \sin(\omega(t - t_1))\right]. \tag{1.15}$$

Here $\epsilon_{1,2}$ are the directions of the earth's velocity in the galactic coordinate system during the spring equinox and summer solstice used to describe the elliptic orbit [84]. Furthermore ω is the angular speed of earth's rotation, t_1 denotes the fraction of the year before March 21 (Spring equinox) and $v_\oplus = 29.8\,km/s$ is earth's speed on its orbit.

1.5.2. Rates and Spectra

WIMPs will only interact very rarely with baryonic matter because of its assumed nature. Thus a detector with a very low Background is essential. Interactions from natural radioactivity is expected to be orders of magnitude higher than the sparse WIMPs interactions. Understanding the WIMP signature in the detector is therefore very important.

To measure the rate of events R, a detector has to have the capability to measure the recoil energy E_r that is deposited in the detection medium after an interaction. The resulting measurement will be the differential energy spectrum $\frac{dR}{dE_r}$. In general, the recoil spectrum can be expressed as

$$\frac{dR}{dE_r} = R_0 \cdot S(E_r) \cdot F^2(E_r) \cdot I, \tag{1.16}$$

where R_0 is the unmodified rate if earth was sitting stationary within the DM halo, see (1.23) for details. $S(E_r)$ represents an energy-dependent factor which includes the detector thresholds, velocity effects or other instrumental dependencies. The desired interactions occur with the target nucleus so there will also be a dependence on the nuclear form factor $F(E_r)$. As the nature of DM is unknown, a spin dependent interaction of the interacting particles has also to be considered. This is expressed with an additional factor I used in spin dependent searches.

The scatter rate R for particles with density number n and uniform velocity distribution v can be described by

$$R = \sigma n v \tag{1.17}$$

with σ being the cross-section i.e. the probability for an interaction [69]. For the velocity distribution $f(\vec{v})$ of the incoming particles the differential scatter rate is obtained with respect to $\mathrm{d}\vec{v}$:

$$\mathrm{d}R = \sigma n v \cdot f(\vec{v})\mathrm{d}^3 v = \sigma \cdot v \mathrm{d}n, \qquad (1.18)$$

where $\mathrm{d}n$ is the differential particle density that is expressed as

$$\mathrm{d}n = \frac{n_0}{k} f(\vec{v})\mathrm{d}^3 v. \qquad (1.19)$$

Here $n_0 = \rho/M_D$ is the local DM particle density for a WIMP of mass M_D in the laboratory frame and

$$k = \int\limits_0^{2\pi} \mathrm{d}\Phi \cdot \int\limits_{-1}^1 \mathrm{d}\cos\Theta \cdot \int\limits_0^{v_{esc}} f(\vec{v})v^2 \mathrm{d}v \qquad (1.20)$$

is a normalization factor such that by integrating over all velocities up the the escape velocity v_{esc} the local DM is preserved

$$\int\limits_0^{v_{esc}} \mathrm{d}n = n_0. \qquad (1.21)$$

For a Maxwell-Boltzmann velocity distribution of the DM particles in the halo (see (1.13)), truncated at a velocity of $v = |\vec{v} - \vec{v}_e| = v_{esc}$, k can be written as

$$k = k_0 \left[\mathrm{erf}\left(\frac{v_{esc}}{v_0}\right) - \frac{2 \cdot v_{esc}}{\sqrt{\pi} \cdot v_0} \cdot \exp\left(\frac{-v_{esc}^2}{v_0^2}\right) \right], \qquad (1.22)$$

with $k = k_0 = (\pi v_0^2)^{2/3}$ for $v_{esc} \mapsto \infty$. For the velocity of earth $v_e = 0$ and $v_{esc} \mapsto \infty$ the total scatter rate is reduced to the expression

$$R_0 = \int\limits_{v=0}^{\infty} \sigma \cdot v \mathrm{d}n = \frac{2}{\sqrt{\pi}} n_0 \sigma v_0. \qquad (1.23)$$

For velocities $v_e \neq 0$ (1.18) yields

$$R = R_0 \frac{k_0}{k} \frac{1}{2\pi v_0^4} \int v f(\vec{v})\mathrm{d}^3 v. \qquad (1.24)$$

A detector located on earth will observe a WIMP velocity $\vec{v}_{\mathrm{obs}}$ with respect to earth's position. Considering this, (1.24) has to be expressed as

$$R(v_e, v_{esc}) = R_0 \frac{k_0}{k} \frac{1}{2\pi v_0^4} \int f(\vec{v}_{\mathrm{obs}} + \vec{v}_e)\mathrm{d}^3 v. \qquad (1.25)$$

After performing the integration in (1.25) for different assumptions of the velocities - only WIMPs with a velocity of $v_e < v < v_{esc}$ can be detected in a target on earth - we get R with respect to v_e and v_{esc}:

$$\frac{R(0, v_{\text{esc}})}{R_0} = \frac{k_0}{k}\left[1 - \left(1 + \frac{v_{\text{esc}}^2}{v_0^2}\right)\exp\left(\frac{-v_{\text{esc}}^2}{v_0^2}\right)\right],$$

$$\frac{R(v_e, \infty)}{R_0} = \frac{1}{2}\left[\sqrt{\pi}\left(\frac{v_{\text{e}}}{v_0} + \frac{1}{2}\frac{v_{\text{e}}^2}{v_0^2}\right)\text{erf}\left(\frac{v_{\text{e}}}{v_0}\right) + \exp\left(\frac{-v_{\text{e}}^2}{v_0^2}\right)\right],$$

$$\frac{R(v_e, v_{\text{esc}})}{R_0} = \frac{k_0}{k}\left[\frac{R(v_e, \infty)}{R_0} - \left(\frac{v_{\text{esc}}^2}{v_0^2} + \frac{1}{3}\frac{v_{\text{e}}^2}{v_0^2} + 1\right)\exp\left(\frac{-v_{\text{esc}}^2}{v_0^2}\right)\right]. \tag{1.26}$$

A WIMP with an incoming kinetic energy of $E_{\text{k}} = \frac{1}{2}M_D v_{\text{obs}}^2$ the resulting recoil energy of the target nucleus is

$$E_{\text{r}} = E_{\text{k}} \cdot r(1 - \cos\Theta)/2 \tag{1.27}$$

where Θ is the scattering angle and r is a kinematic factor that can be expressed as

$$r = \frac{4 M_D M_T}{(M_D + M_T)^2}. \tag{1.28}$$

Here M_T is the mass of the target nucleus and M_D being the WIMP mass.

Introducing the dependence on the recoil energy E_r and assuming a uniform distribution in the range of $0 \leq E_r \leq E_k \cdot r$ the differential recoil energy rate can be expressed as

$$\frac{\text{d}R}{\text{d}E_r} = \int_{E_{min}}^{E_{max}} \frac{1}{E_k \cdot r}\text{d}R(E_k) = \frac{1}{E_0 \cdot r}\int_{v_{min}}^{v_{max}} \frac{v_0^2}{v^2}\text{d}R(v_{\text{obs}}). \tag{1.29}$$

The minimal DM particle velocity v_{min} corresponds to $E_{min} = E_r/r$ and $E_0 = \frac{1}{2}M_D v_0^2$. E_{min} is the smallest energy to give a recoil energy E_r where v_{min} is given by

$$v_{\text{min}} = \sqrt{2E_{\text{min}}/M_D} = v_0\sqrt{E_r/E_0 r}. \tag{1.30}$$

Together with (1.18) the differential recoil rates for different velocities can finally be written as

$$\frac{\text{d}R(0, v_{esc})}{\text{d}E_r} = \frac{k_0}{k}\frac{R_0}{E_0 \cdot r}\left(\exp\left(\frac{-E_r}{E_0 \cdot r}\right) - \exp\left(\frac{-v_{esc}^2}{v_0^2}\right)\right), \tag{1.31}$$

$$\frac{\text{d}R(v_e, \infty)}{\text{d}E_r} = \frac{R_0}{E_0 \cdot r}\frac{\sqrt{\pi}}{4}\frac{v_0}{v_e}\left[\text{erf}\left(\frac{v_{min} + v_e}{v_0}\right) - \text{erf}\left(\frac{v_{min} - v_e}{v_0}\right)\right], \tag{1.32}$$

$$\frac{\text{d}R(v_e, v_{esc})}{\text{d}E_r} = \frac{k_0}{k}\left[\frac{\text{d}R(v_e, \infty)}{\text{d}E_r} - \frac{R_0}{E_0 \cdot r}\exp\left(\frac{-v_{esc}^2}{v_0^2}\right)\right]. \tag{1.33}$$

In the usual convention R_0 is normalized with standard numerical values, $v_0 = 230\,\text{km/s}$, $\rho_D = 0.4\,\text{GeV/c}^2/\text{cm}^3$ and is expressed in the units events/kg/day:

$$R_0 = \frac{503}{M_D M_T}\left(\frac{\sigma_0}{1\cdot 10^{-36}\,\text{cm}^2}\right)\left(\frac{\rho_D}{0.4\,\text{GeV/c}^2/\text{cm}^3}\right)\left(\frac{v_0}{230\,\text{km/s}}\right) \tag{1.34}$$

with M_D, M_T in GeV/c^2.

With rising momentum transfer $q = \sqrt{2M_T E_r}$ the de Broglie wavelength $\lambda = h/q$ is no longer large compared to the size of the target nucleus, resulting in a dropping cross-section. This is represented by the form factor that introduces a q-dependence to the cross-section:

$$\sigma(qr_n) = \sigma_0 \cdot F^2(qr_n) \tag{1.35}$$

where r_n is the effective nuclear radius. In more detail, considering an isotropic density and the plane wave approximation, the Form Factor is the Fourier Transform of the charge density distribution described as

$$F(q) = \int_V \rho(r) e^{i\vec{q}\vec{r}} d^3x \tag{1.36}$$

$$= \frac{4\pi}{q} \int_0^\infty r \sin(qr) \rho(r) dr. \tag{1.37}$$

One of the most popular density profiles was suggested by Helm [57] already in 1956:

$$\rho(r) = \int_V \rho_0(\vec{r'}) \rho_1(\vec{r} - \vec{r'}) \tag{1.38}$$

where

$$\rho_0(r) = \begin{cases} \frac{3}{4\pi r_n^3} & r < r_n \\ 0 & r > r_n \end{cases}, \text{ and} \tag{1.39}$$

$$\rho_1(r) = \frac{1}{(2\pi s^2)^{2/3}} e^{-(qs)^2/2}. \tag{1.40}$$

For large atomic masses, e.g. $A = 131$ for ^{131}Xe, this effect becomes quite significant. Therefore it is important to understand the form factor. Here, the nucleus is described as a sphere with a solid core density and a Gaussian falling density on the outside, called the skin with thickness s. With this the form factor is obtained:

$$F(qr_n) = 3 \cdot \frac{j_1(qr_n)}{qr_n} \cdot \exp\left(\frac{-(qs)^2}{2}\right) \tag{1.41}$$

where $j_1(qr_n)$ is the first order spherical Bessel function and $s = 1$ fm is the skin thickness parameter and $r_n = \sqrt{r_v^2 - 5s^2}$ where $r_v = 1.2A_T^{1/3}$ fm. An advantage of this formulation lies within its analytical solvability. In figure 1.10 the behavior of the squared Form Factor is illustrated for different target nuclei as a function of the recoil energy E_r in keV.

Combining the rate calculations with the form factor yields the complete description of the differential recoil energy spectrum before any detection efficiencies or threshold effects. In figure 1.11 the result is shown for different target materials for a WIMP mass of $100\,GeV$ and a reference cross-section of $10^{-45}\,cm^2$. Xenon yields the highest rates in the low energy region between 0 and ~35 keV. This is also the region where nuclear recoils of WIMPs are expected and so xenon becomes the preferred target for most DM direct search
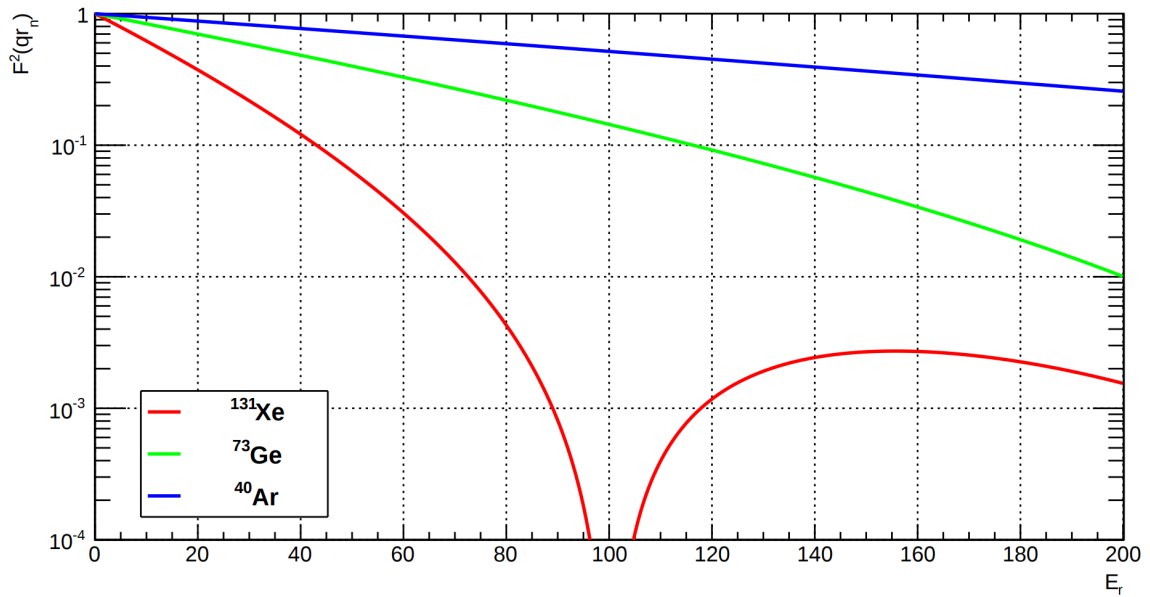
Figure 1.10.: Behavior of the squared Form Factor for different target materials [85].
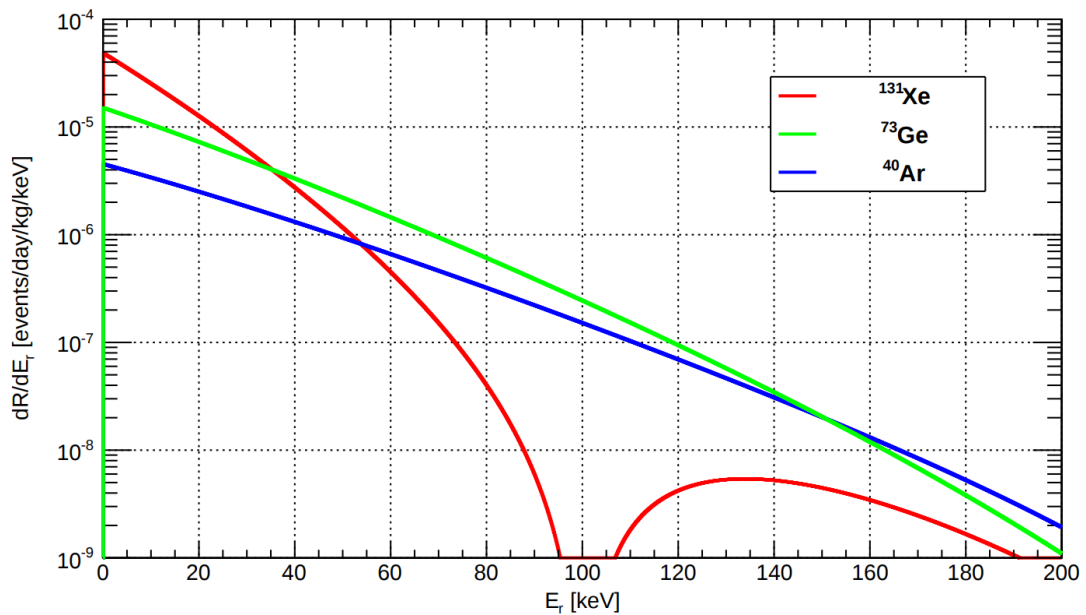

Figure 1.11.: Differential recoil energy spectrum for different target materials for a WIMP with $m_\chi = 100\,\text{GeV}$ and a reference cross-section $\sigma_\chi = 10^{-45}\,\text{cm}^2$ [85].

experiments. Figure 1.12 shows the impact of different WIMP masses with a reference cross-section of $10^{-45}\,\text{cm}^2$ and liquid xenon as detection material.

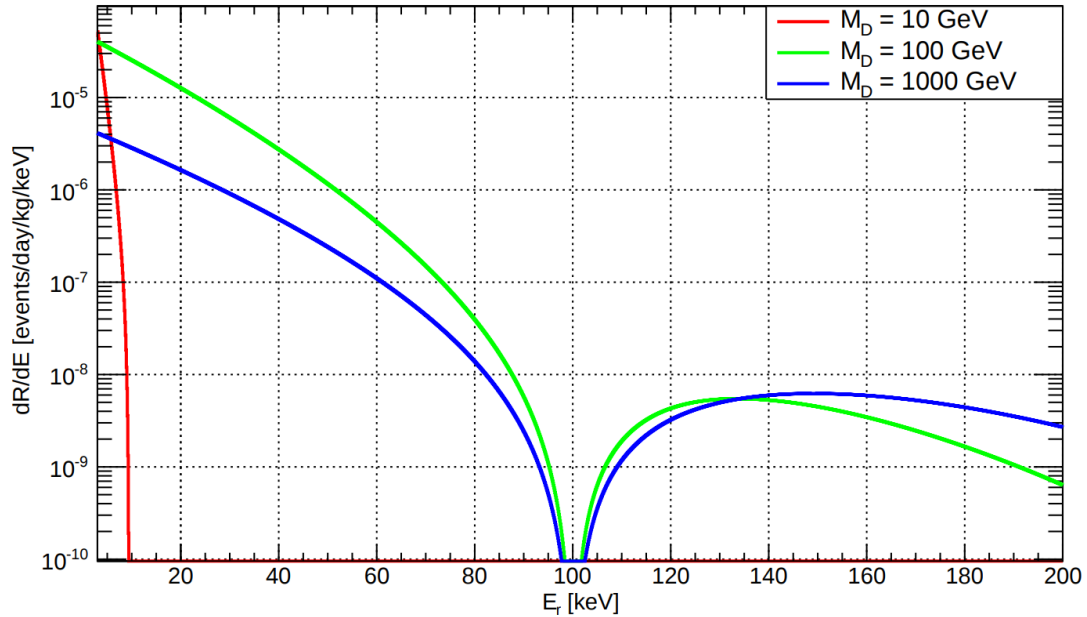One of the most common ways to express the differential recoil energy rate for the spin

Figure 1.12.: Differential recoil energy spectrum for different WIMP masses with a reference cross-section $\sigma_\chi = 10^{-45}$ cm^2 and liquid xenon as detection material [85].

independent case follows as

$$\frac{\mathrm{d}R}{\mathrm{d}E}(E,t) = \frac{\rho_D}{2\mu_A^2 \cdot m_\chi} \sigma_0 \cdot A^2 \cdot F^2 \int_{v_{min}}^{v_{esc}} \frac{f(\vec{v},t)}{v} \mathrm{d}^3 v. \tag{1.42}$$

This will be the basis all the later analyses will inherit from.

1.6. Other Detection Principles

Apart from direct detection, there are also other approaches in the search for DM [93]. Since the focus of this work is on the direct detection, the other approaches will only be discussed briefly for completeness of the theory part of this thesis.

1.6.1. Indirect Detection

The galactic center and halo, close galaxy clusters or dwarf galaxies, also called dwarf spheroidals, are the favored sources to search for indirect signals since DM gravitationally accumulates in these astrophysical objects. The latter locations are very popular due to their large measured mass to light ratio and their small background. The increased DM density in these regions leads to an enhanced self-annihilation, scattering or decay into standard model particles. A measurable particle flux of secondary particles (see e.g. [89]

21

for a more detailed description) could be produced. The measurement of these secondary particles is usually denoted as indirect detection.

Examples of possible annihilation channels, which produce a secondary particle that can be detected are

$$\chi\bar{\chi} \rightarrow \gamma\gamma, \gamma Z, \gamma H \tag{1.43}$$
$$\chi\bar{\chi} \rightarrow q\bar{q}, W^-W^+, ZZ. \tag{1.44}$$

Some of the products also decay further into e^-e^+, pp, γ-rays or neutrinos.

A second process to generate charged particles and anti-particles or photons and neutrinos can be observed from the decay of DM. In contrast to self-annihilation processes, where the production rate shows a characteristic quadratic dependence on the DM density, the decay only scales linearly, see e.g. [59].

In addition, DM particles might be gravitationally captured inside the Sun due to elastic scattering with its nuclei inside the core. The annihilation of these captured DM particles can also produce neutrinos which are capable of propagating out of the Sun and therefore might be detectable with Earth-bound neutrino telescopes like e.g. the IceCube detector and its upgrades which is located at the geographical south pole [55].

1.6.2. Production

Since 2008 and the start of the Large Hadron Collider (LHC) runs at CERN, many of the operating experiments like CMS [34] or ATLAS [19] have been searching for new particles in proton-proton collisions at a center-of-mass energy of up to 13 TeV, which has been reached in 2018. The two experiments have studied a number of new particle signatures exploring different parameter spaces of different e.g. supersymmetric and also extra-dimensional models. The presence of a DM particle would only be inferred by observing events with a missing transferred momentum and energy. Therefore, events with, e.g. an energetic jet and an imbalanced momentum transfer are picked for further analysis. Reactions of the type

$$pp \rightarrow \chi\bar{\chi} + x \tag{1.45}$$

are investigated, where x represents a hadronic jet, a photon or a Z or W boson decaying through the leptonic channel. The published results up to now are consistent with the SM expectations, see e.g. [18, 33, 32].

For given particle masses, the bounds can be translated into upper limits on the cross-section. Bounds arising from accelerator searches are most constraining below roughly 5 GeV and a few hundreds of GeV for spin-independent and spin-dependent interactions, respectively. With the high luminosity upgrade coming in the near future, the LHC will keep searching for DM and further searches will be performed.

Chapter 2

The XENON Project

Materials that show luminescence, i.e. emitting light of a certain characteristic after the absorption of a particle, are called scintillators. This production of photons, combined with ionization is one of the well established mechanisms used in (single) particle detection. The detectors of the XENON project [90] are designed to make maximum usage of these processes (scintillation & ionization) using liquid xenon as a detection medium. In section 1.5.2 the expected interaction rates for nuclear recoils using different detection materials has been calculated. Together with the expected range for nuclear recoil energies that a WIMP will transfer, xenon seems to be the best choice to cover the low energy region. The most recent XENON detector XENON1T is already the third generation utilizing this detection technique, steadily increasing the volume of the active detection material since the start of the project in 2007.

This chapter will introduce why xenon is one of the best choices for direct DM search purposes. Apart of the highest expected scatter rates, the working principle of dual phase Time Projection Chambers (TPCs) are introduced and their realizations in the XENON100 and XENON1T detectors will be shown.

2.1. Xenon as Detection Material

WIMPs are supposed to interact with normal matter by depositing a small amount of energy as they scatter elastically on a target nuclei. To measure such small energies a detector with a very low background is needed. Because of natural radioactivity, only very pure materials can be used and thus a lot of effort is put into selecting and screening them already prior of building the detector [15, 5].

There are many physical and chemical reasons why xenon is very interesting for the usage as a detection medium. The main advantages are discussed in the following sections:

2.1.1. Radio Purity

Xenon can be produced with a very high radio purity as a byproduct of distilling air to obtain oxygen and nitrogen. Naturally it is consisting of 8 stable isotopes and one

radioactive isotope ^{136}Xe which has a very high half-life of $2.11 \cdot 10^{21}$ years.

2.1.2. High Atomic Number

For coherent scattering the cross section is proportional to the square of the atomic mass number of the target nuclei A_T^2. With a A=54, xenon yields the highest rates for low nuclear recoil energies in comparison with other commonly used detection materials, see section 1.5.2. On the other hand the rate drops more quickly due to nuclear form factor effects. Since the recoil energies of interest in a direct search DM experiment are supposed to be very low, xenon is the optimal target material.

2.1.3. High Density

In addition of being the heaviest non radioactive noble gas, liquid xenon is also very dense. Its density of $2.85 \, \text{g/cm}^3$ (that varies slightly with pressure) is ~3 times higher than that of water. This also leads to high self-shielding properties against the radioactivity from the detector materials and surroundings within the inner xenon volume of a detector.

2.1.4. Cryogenics

On the cryogenic side, liquid Xenon (LXe) is also relatively easy to handle. It can be liquefied at a sufficient pressure, can easily be cooled by e.g. a Pulse Tube Refrigerator (PTR) and also can be handled with liquid nitrogen in emergency situations like a power outage. See figure 2.1, for the full phase curve of xenon.
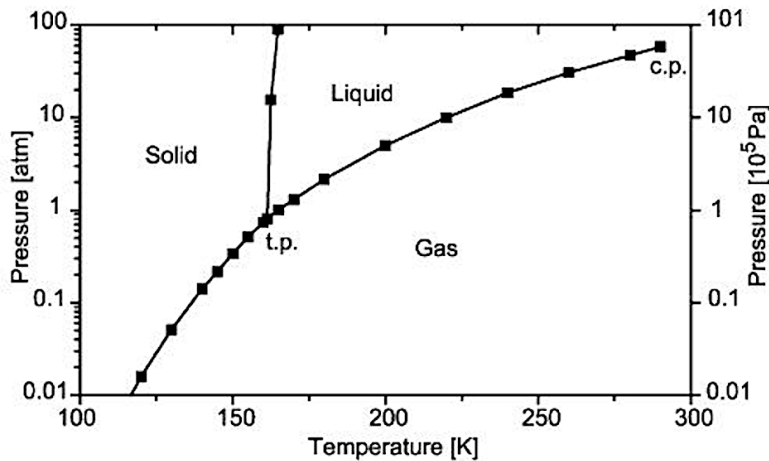

Figure 2.1.: Phase diagram of xenon [29]. For a sufficient pressure xenon can already be liquefied with relative low technical effort.

2.1.5. Scintillation and Ionization of Xenon

An interaction in xenon results in two processes: excitation (Xe^*) and ionization (Xe^+). The excited xenon atoms combine with ground state atoms to form excimers

$$Xe^* + Xe \longrightarrow Xe_2^*, \tag{2.1}$$

where the ionized xenon atoms form dimers

$$Xe^+ + Xe \longrightarrow Xe_2^+. \tag{2.2}$$

The excimer decays by emitting photons (scintillation) that lie in the VUV range with a wavelength of 175 nm (~7 eV)

$$Xe_2^* \longrightarrow 2\,Xe + \hbar\mu, \tag{2.3}$$

while the dimers recombine with in the earlier process produced free electrons and are reduced to excimers and heat

$$Xe_2^+ + e^- \longrightarrow Xe_2^* + \text{heat}. \tag{2.4}$$

These secondary excimers also decay following (2.3). Since xenon does not have an energy gap matching the emitted VUV photons of 7 eV, it is transparent to its own scintillation light. An illustration of these processes can be found in figure 2.2.

If an external electrical field is applied while the above mentioned processes take place, there are additional effects to consider: The charged particles (electrons) are drifting away from the interaction side following the direction of the electrical field. This reduces the recombination rate of the ionized xenon atoms (2.4) since less electrons remain in the area and thus the photons produced from the secondary excimers (2.3) are suppressed. This reduction in scintillation light is called electric field quenching. The lack of the atomic energy gap matching, makes it possible to build detectors up to a very large scale without losing much of the scintillation light through absorption.

2.2. Xenon Dual Phase Time Projection Chamber

After looking at the processes that lead to a signal, the following sections will describe how to measure these signals in detail. To extract the maximum on information from the interactions that happen in the liquid xenon, a dual phase Time Projection Chamber (TPC) is used. This detection technique is capable of measuring both, light (photons) and the charge (electrons) that is produced during an interaction.

In figure 2.3 the typical structure of a TPC plus its signal measurement process is shown [15]. It is equipped with two arrays of photo sensors to detect the scintillation light. The Photomultiplier Tubes (PMTs) sit on top (pointing downwards) and on the bottom (pointing upwards) of a cylindrical chamber which contains the liquid xenon. The walls of the cylinder are optically reflective to provide a better light collection efficiency. The electrical field, to enable electron drift, is applied between several metallic meshes (or
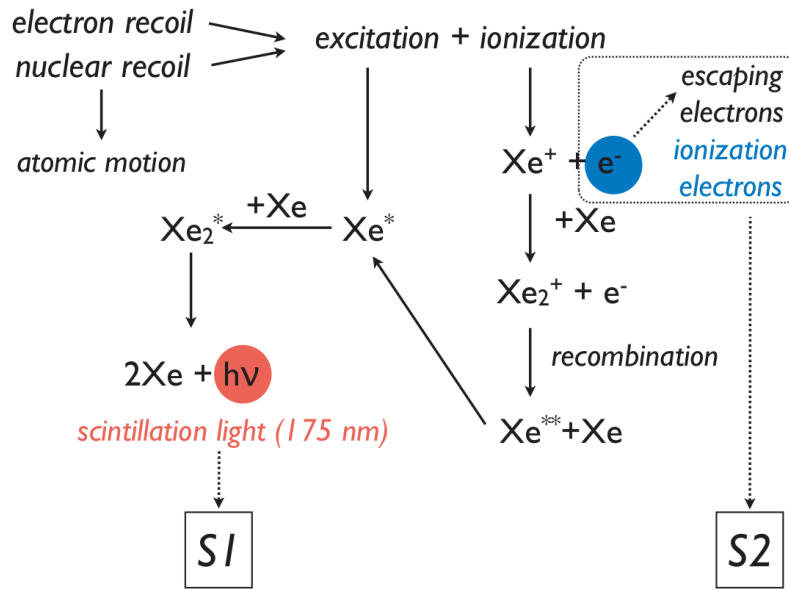
Figure 2.2.: Schematic of the processes after an energy deposit in liquid xenon. After an initial loss in atomic motion (heat), a nuclear recoil splits into two channels: excitation and ionization. These two channels in their respective ends lead to the primary scintillation signal (S1) via excitation and the proportional scintillation signal (S2) via ionization. Additional losses occur by e.g. recombination [66].

grids). The cathode mesh is positioned on the bottom above the light sensors and the anode mesh is located a few millimeters above the liquid surface. The anode (cathode) is connected to a positive (negative) high voltage. There are additional meshes placed above and below (already in the liquid) the anode, which are both connected to ground potential. These extra meshes close up the electrical field towards the liquid (below) and gas phase (above). The mesh below the anode is called the gate-mesh. Choosing the polarity in the given configuration lets the electrons, which have been produced at the interaction site, drift upwards towards the liquid-gas interface.

An incoming particle hitting the LXe starts the processes described in 2.1.5 leading to prompt scintillation photons and ionization electrons. The prompt scintillation photons hitting the PMTs (which convert the photons into charge) are detected as the primary (or first) scintillation signal called *S*1. A certain amount of the electrons produced at the interaction site drift away because of the presence of the applied electrical field. The voltage of the electrical field directly influences the amount of electrons that are able to escape before recombining with the ionized xenon atoms. The stronger the field, the less excited dimers are present that are able to produce light during their decay (see (2.4)). The strength of the field therefore has to be chosen to balance the light and charge yield. The electrons that reach the liquid-gas interface are extracted into the gas phase by an even stronger field present between the gate and the anode meshes. In the gaseous phase
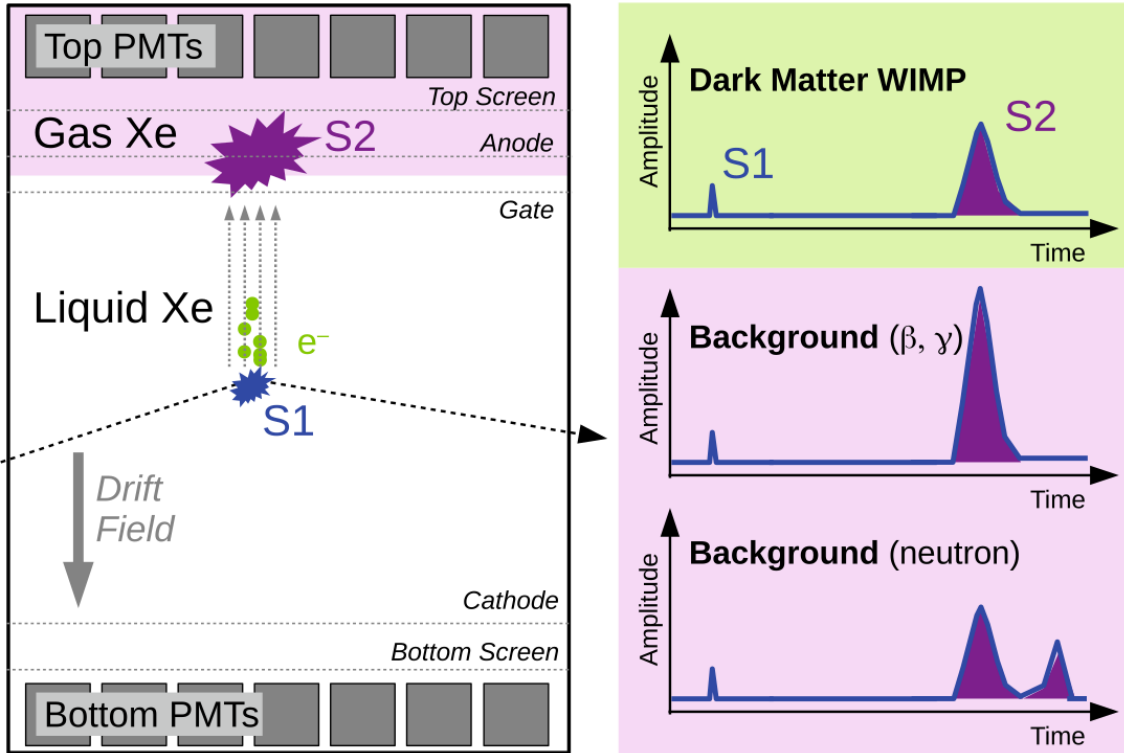
Figure 2.3.: Left: Scheme of the working principal of a xenon dual phase TPC. An incoming particle creates two signals, the direct scintillation light S1 and the proportional charge induced, delayed scintillation signal S2. Right: Nuclear and electronic recoils lead to a different ratio of the charge (S2) and light (S1) signal. This is used for background discrimination purposes. The main part of the Background consists of electronic recoils from β or γ interactions. But also double scatters from neutrons can be found [15].

the electrons are accelerated because of the different relative permittivities and densities of the gaseous xenon and excite gaseous xenon atoms to produce the proportional scintillation light. The light produced and detected by the PMTs during this second scintillation process is called proportional scintillation signal or short $S2$.

Because of the known drift velocity of the electrons, the time difference between the $S1$ and $S2$ signal can directly be translated into the interaction depth z inside the detector. The x-y-position is inferred by the proportional scintillation hit pattern on the top PMT array using various algorithms.

The ability to have a full 3D position reconstruction of the vertex allows to define a fiducial volume within the target volume to e.g. select regions of lower background. Since xenon is very dense, it has very good self-shielding properties which causes most background events from the surrounding materials and external radiation to be stopped already in the outer parts of the detector volume. This way also interactions that produce

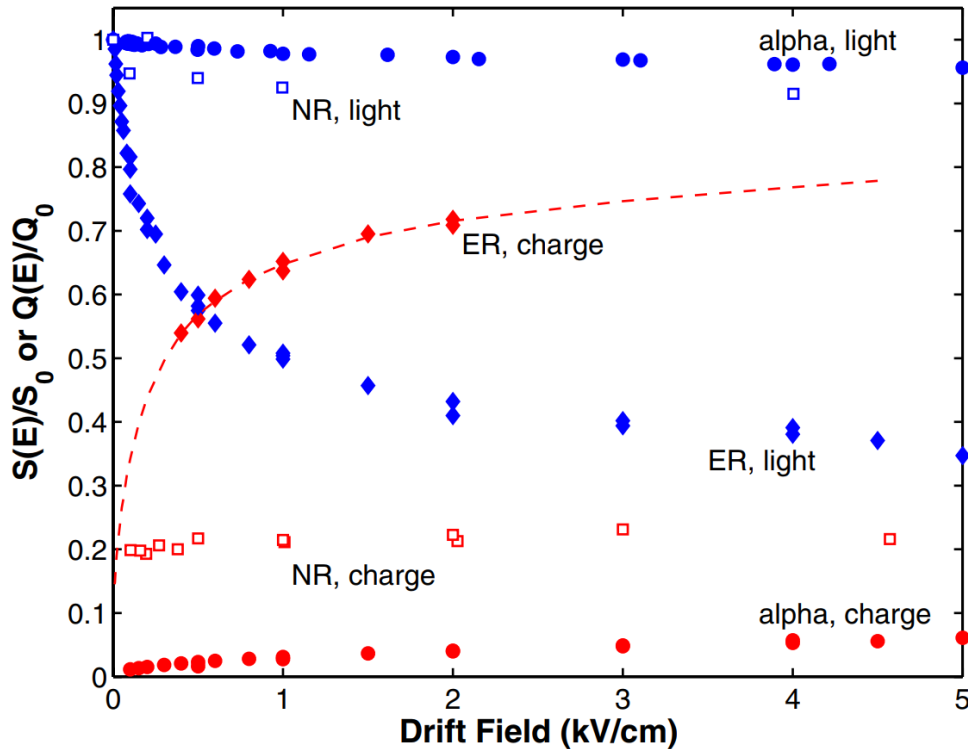double scatters can be discriminated because WIMPs will only interact once.

Figure 2.4.: Field dependence of scintillation and ionization yield in LXe for 122 keV electron recoils (ER), 56.5 keV$_r$ nuclear recoils (NR) and 5.5 MeV alphas, relative to the yield with no drift field [14].

For the direct search of Dark Matter most important form of interactions are nuclear recoils (NR), which are induced by WIMPs or neutrons. This makes neutrons one of the most dangerous backgrounds since the signal signature resembles that of a WIMP. On the other hand, neutrons can be used to calibrate the signal response of the detector (see right side of figure 2.3 for an example). Other backgrounds like the interactions of γ- or β-radiation sources produce electronic recoils (ER), where only the electron clouds of the target material atoms participate in the signal process. These two kind of interactions, NR or ER, lead to a different signal response. Utilizing this feature, the different signal ratios S2/S1 deliver a way to discriminate between NR and ER which is already a good and simple tool to separate signal from background events, see the right part of figure 2.3 for illustration.

In this work, the production of electrons and photons of a signal event are described as independent statistical processes. This is a good approximation that is still widely used since the anti-correlation between the electron and photon channel for nuclear recoils is small [14, 6]. Figure 2.4 shows measurements of the ionization and scintillation yield for electronic and nuclear recoils at different drift fields. While there is a strong anti-

correlation for ER, no visible dependence can be seen for the NR case. This is the reason the above mentioned approximation can be used in the signal case.

For a nuclear recoil, the probability P to get N_γ photons and N_e electrons from a recoil energy E_r can therefore be written as independent processes, following the scheme in figure 2.2:

$$P(N_\gamma, N_e | E_r, \mathcal{E}) \approx \text{Poi}(N_\gamma | n_\gamma) \text{Poi}(N_e | n_e),\tag{2.5}$$

where $\mathcal{E}$ is the strength of the applied electrical drift field and n_γ (n_e) are the expectation values of the generated photons (electrons). Further, these expectation values can be expressed as

$$n_\gamma(E_r, \mathcal{E}) \approx \frac{E_r}{W_\gamma(E_r, \mathcal{E} = 0)} S_r(\mathcal{E})\tag{2.6}$$

$$n_e(E_r, \mathcal{E}) \approx \frac{E_r}{W_e(E_r, \mathcal{E}_{ref} \to \infty)} T_r(\mathcal{E})\tag{2.7}$$

where $S_r(0) = 1$ and $T_r(\infty) = 1$. Here average energies needed to create a photon or an electron are expressed with the effective W-values W_γ and W_e. These values themselves depend on the interaction type (either NR or Er), the drift field and the deposited energy E_r. An additional effect called field-quenching reduces the light yield is expressed as $S_r(\mathcal{E})$ and the factor $T_r(\mathcal{E})$ accounts for the charge loss due to recombining electrons. For the nuclear recoil energy calibration, signals from known γ-ray lines are compared to dedicated measurements of the functions W_γ and S_r or W_e and T_r which differ for NR or ER. To model the detector response, historically the reverence source ^{57}Co with its 122 keV$_{ee}$ line is used, where keV$_{ee}$ is the electronic-equivalent recoil energy. To establish the energy scale at low γ and nuclear recoil energies, the in-situ light and charge yields at 122 keV$_e e$ can be used as fix points by using the ratios of the W-values relative to the ^{57}Co line and involving the functions $S_r(\mathcal{E})$ and $T_r(\mathcal{E})$ respectively [7].

Since for nuclear recoils the W_γ-value has been measured to lower energies, the standard analysis for XENON100 only used the primary scintillation light (S1) to infer the deposited energy in the earlier publications. One of the main efforts of this work will be to include also the proportional scintillation light (S2) into the energy estimation and the full spatial information, see section 6.3.2.

2.2.1. Primary Scintillation Light

In terms of charge, the primary scintillation signal in PMT$_i$ can be expressed as

$$s1_i^q(\vec{r}) = n_\gamma(E_r, \mathcal{E}) \gamma_i(\vec{r}) \eta_i g_i = n_\gamma(E_r, \mathcal{E}) \mu_i(\vec{r}) g_i\tag{2.8}$$

where q highlights the fact that the value is still presented in units of charge, g_i is the gain and η_i is the product of quantum and collection efficiency of PMT$_i$ [7]. The combination of γ_i and η_i is called the light collection efficiency $\mu_i(\vec{r})$ which is measured separately with the lines of γ-ray calibration sources.

The data processor converts the charge to a signal in the standard units of photoelectrons (pe). The expectation value on a single PMT_i, with spatially dependent light collection efficiency $\mu_i(\vec{r})$, is given as

$$s1_i(\vec{r}) \approx n_\gamma(E_r, \mathcal{E}) \mu_i(\vec{r}). \tag{2.9}$$

with n_γ from (2.6). This leads to a total expectation value for a NR of

$$s1(\vec{r}) = \sum_{i=1}^{M} s1_i(\vec{r}) \approx n_\gamma(E_{nr}, \mathcal{E}) \mu(\vec{r}) \tag{2.10}$$

$$= E_{nr} \mathscr{L}_y(E_{ee} = E_{ref}, \mathcal{E}, \vec{r}) \times \mathscr{L}_{\text{eff}}(E_{nr}, \mathcal{E} = 0) \frac{S_{nr}(\mathcal{E})}{S_{ee}(\mathcal{E})} \tag{2.11}$$

where M is the number PMTs and $\sum_i \mu_i(\vec{r}) = \mu(\vec{r})$. S_{ee} and S_{nr} are the field dependent nuclear quenching factors that describe the reduction of light yield for nuclear (nr) or electronic (ee) recoils in the presence of an electric field relative to zero field. E_{ref} is the energy of a reference γ-ray, historically the 122 keV$_{ee}$ line of the ^{57}Co decay and $\mathscr{L}_y$ is the measured light yield in units of PE/keV$_{ee}$ for a given drift field $\mathcal{E}$ and position $\vec{r}$ defined as

$$\mathscr{L}_y(E_{ee} = E_{ref}, \mathcal{E}, \vec{r}) = \frac{S_{ee}(\mathcal{E}) \mu(\vec{r})}{W_\gamma(E_{ee} = E_{ref}, \mathcal{E} = 0)}. \tag{2.12}$$

For nuclear recoils the relative scintillation efficiency $\mathscr{L}_{\text{eff}}$, with respect to the reference γ-ray line at zero drift field ($\mathcal{E} = 0$)is given as

$$\mathscr{L}_{\text{eff}}(E_{nr}, \mathcal{E} = 0) = \frac{W_\gamma(E_{ee} = E_{ref}, \mathcal{E} = 0)}{W_\gamma(E_{nr}, \mathcal{E} = 0)}. \tag{2.13}$$

The XENON100 analysis is done in the spatially independent data space. Here the light yield $\mathcal{L}_y$ as been spatially averaged over the detector volume. In this case the expression for the expectation value changes to

$$cs1 = E_{nr} \langle \mathscr{L}_y \rangle \mathscr{L}_{\text{eff}}(E_{nr}) \frac{S_{nr}}{S_{ee}} \tag{2.14}$$

where $\langle \mathscr{L}_y \rangle$ is the average detector light yield. This relation directly connects the energy deposit of a nuclear recoil to the expected amount of photoelectrons measured by all the PMTs of the detector.

The conversion of the expectation value n_γ to the observed value N_γ is a statistical process and follows a Poisson process which itself is followed by the Binomial process of the photons hitting the PMT cathodes and producing (or not) a photoelectron via the photoelectric effect. These photoelectrons are accelerated towards the anode by passing several dynode stages inside the PMT where they experience even further acceleration. In each dynode stage more and more electrons are produced when they hit the dynode material with increased kinetic energy. This amplification process inside a PMT is usually modeled as a Gaussian distribution with mean N_{pe} and width $\sigma_{PMT}\sqrt{N_{pe}}$. The single

photoelectron width σ_{PMT} is a PMT intrinsic parameter which is obtained through calibration. This model of the different components of the signal generation can be written as a pdf

$$
\begin{aligned}
p_{S1,i}(S1_i|n_\gamma(E_r,\mathcal{E}))\mathrm{d}S1_i &= \sum_{N_{pe,i}}\sum_{N_\gamma} p_{pmt,i}(S1_i|N_{pe,i})\mathrm{d}S1_i \\
&\times \mathrm{Binom}(N_{pe,i}|N_\gamma \cdot \mu_i(\vec{r})) \\
&\times \mathrm{Poi}(N_\gamma|n_\gamma(E_r,\mathcal{E})) \\
&= \sum_{N_{pe,i}} p_{pmt,i}(S1_i|N_{pe,i})\times \mathrm{Poi}(N_{pe,i}|n_\gamma\mu_i(\vec{r}))\mathrm{d}S1_i \\
&= \sum_{N_{pe,i}} \mathcal{N}_{S1,i}(N_{pe,i},\sigma^2_{PMT,i}N_{pe,i})\times \mathrm{Poi}(N_{pe,i}|n_\gamma\mu_i(\vec{r}))\mathrm{d}S1_i, \quad (2.15)
\end{aligned}
$$

where the relationship

$$
\sum_{k=n}^{\infty} \mathrm{Binom}_k(n,p)\mathrm{Poi}_k(\lambda) = \mathrm{Poi}_n(\lambda p) \tag{2.16}
$$

and the definitions

$$
\mathrm{Poi}(n|\lambda) = \mathrm{Poi}_n(\lambda) = e^{-\lambda}\frac{\lambda^n}{n!} \tag{2.17}
$$

and

$$
\mathrm{Binom}(k|n,p) = \mathrm{Binom}_k(n,p) = \binom{n}{k}p^k(1-p)^{n-k} \tag{2.18}
$$

have been utilized. In addition $p_{pmt,i}$ has been approximated by a normal distribution $\mathcal{N}_{S1,i}$. The total corrected S1 signal is obtained by further assuming an average detector response $\mu(\vec{r}) = \langle\mu\rangle$ and the same average PMT response $\sigma_{PMT} = 0.5$, which yields the final form of the total spatial corrected signal pdf as

$$
p_{cS1}(cS1|n_\gamma(E_r,\mathcal{E})) \approx \sum_{N_{pe}}\mathcal{N}_{cS1}(N_{pe},\sigma^2_{PMT}N_{pe})\times \mathrm{Poi}(N_{pe}|n_\gamma\langle\mu\rangle). \tag{2.19}
$$

2.2.2. Secondary (Proportional) Scintillation Light

While the electrons drift upwards towards the liquid-gas interface, following the direction of the applied drift field, some electrons get lost due to the attachment to impurities. The characteristic time until such a loss occurs is called the electron lifetime τ_e [7]. The surviving electrons on the other hand are extracted into the gas phase with a efficiency κ that depends on the extraction field $\mathcal{E}_{gas}$. Electrons still in the extraction field, but already in the gas phase are accelerated and collide with the gas atoms, resulting in a proportional scintillation with an amplification factor Y. This light signal is named S2. Considering these effects, the expectation value for a PMT$_i$ to see this secondary scintillation light is given by

$$
s2_i(\vec{r}) \approx n_e(E_n,\mathcal{E}) \cdot e^{-t_d/\tau_e} \cdot \kappa(\mathcal{E}_{gas}) \cdot Y(\frac{\mathcal{E}_{gas}}{\rho},h_g) \cdot \beta_i(x,y) \cdot \eta_i \tag{2.20}
$$

where ρ is the gas density, h_g is the size of the gas gap between the liquid surface and the anode mesh. $\beta_i(x,y)$ is the probability of a photon that has been created at position (x,y) to reach the photo-cathode of PMT$_i$. Like in the S1 case, η_i represents the product of the quantum and collection efficiency of PMT$_i$.

With the help of γ-ray line calibration only the product $\delta_i(x,y) = \kappa Y \beta_i \eta_i$ can be measured. In XENON100 this factor was measured for the sum over the PMTs, resulting in an estimate of $\delta(x,y) = \sum_i^M \delta_i(x,y)$. This reduces (2.20), while summing over all PMTs and also applying (2.7), to

$$s2(\vec{r}) = E_r \cdot Q_y(E_r)e^{-t_d/\tau_e}\delta(x,y), \tag{2.21}$$

where $\mathcal{Q}_y = T_{nr}(\mathcal{E})/W_e(E_{nr}, \mathcal{E}_{ref})$ is the measured charge yield for nuclear recoils at a given reference drift field $\mathcal{E}_{ref}$.

As already discussed in the previous section of the primary scintillation light S1, the same statistical processes have to be considered to get from the expectation value of electrons produced at the interaction site to the measured signal in units of photoelectrons. Analogous to (2.19) the pdf for the proportional (secondary) scintillation signal can be written as

$$p_{S2}(S2|n_e(E_r,\mathcal{E}))\mathrm{d}cS2 = \sum_{N_{pe}}\mathcal{N}_{S2}(N_{pe},\sigma_{PMT}^2 N_{pe}) \times \mathrm{Poi}(N_{pe}|n_e,\delta(x,y))\mathrm{d}cS2. \tag{2.22}$$

Following this expression, the spatially corrected signal cS2 can be calculated as

$$cS2 = S2(\vec{r})e^{t_d/\tau_e}\frac{\langle\delta\rangle}{\delta(x,y)} \tag{2.23}$$

where $\langle\delta\rangle$ is the average of $\delta(x,y)$.

2.2.3. Wavelength-Dependent Double Photon Emission

Recent studies showed that the emission of photoelectrons from the PMT cathodes is wavelength dependent, see [44]. 18-24 % of the time, when struck with a deep UV photon of 175 nm two photoelectrons are emitted. In figure 2.5 the measured spectrum is shown. This finding is relevant when estimating the amount of photons that contribute to a signal from its observed charge signal. Since this behavior also holds for the XENON1T R11410 PMTs [20, 13], this effect has to be taken care of when extending the later introduced framework to the XENON1T configuration. A first qualitative study to confirm this effect has been discussed in [1].

2.3. The XENON100 Detector

The XENON100 detector is located at the Laboratori Nazionali del Gran Sasso (LNGS) underground laboratory in Italy, see figure 2.7 for an impression of the laboratory surroundings.
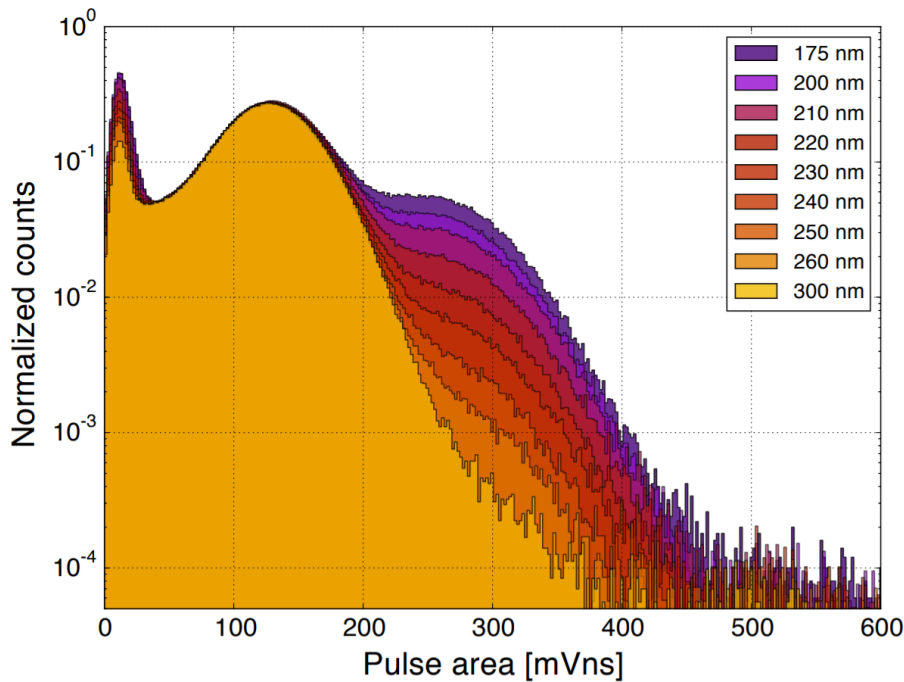
Figure 2.5.: Response of a R11410 PMT illuminated with different wavelengths. The spectra are normalized in the same range to make them comparable. With smaller wavelength and thus higher energy, the probability a single photon will produce two photo electrons rises (orange to purple) [44].

It is a two-phase Time Projection Chamber (TPC) with liquid Xenon (LXe) as a detection medium. The detection chamber is about 30 cm in height and also about 30 cm in diameter, see innermost part in figure 2.6a. The whole detector holds about 161 kg of LXe which separates in 62 kg active material and 99 kg of a self-shielding and active veto. In addition, the TPC is also shielded by different passive materials like PTFE, copper and water, see figure 2.6b. Both channels, light and charge, are used to extract information on the deposited energy and nature of the particle interaction, i.e. electronic (ER) or nuclear recoils (NR). Its ability of the 3-D position reconstruction, using the time difference of primary and secondary scintillation signal to determine the z position and the PMT hit-pattern to derive the x,y position, is used to e.g. reduce the electromagnetic background from external sources by defining an inner very quiet fiducial volume [5]. With all its capabilities the XENON100 detector has been the most sensitive experiment in direct search for WIMP Dark Matter over several years.

Its best performance of excluding WIMP interactions was archived in 2014 by combining three of its science runs to a total of 477 live days, which resulted in a total exposure of $48 \, \text{kg} \times \text{yr}$ [100]. The minimum of the upper limit archived was at $1.1 \times 10^{-45} \, \text{cm}^2$ for a WIMP mass of $50 \, \text{GeV}$ at 90% confidence level. Up to now, it has been the longest running detector of its kind and explored many new technologies that are a standard as of today.
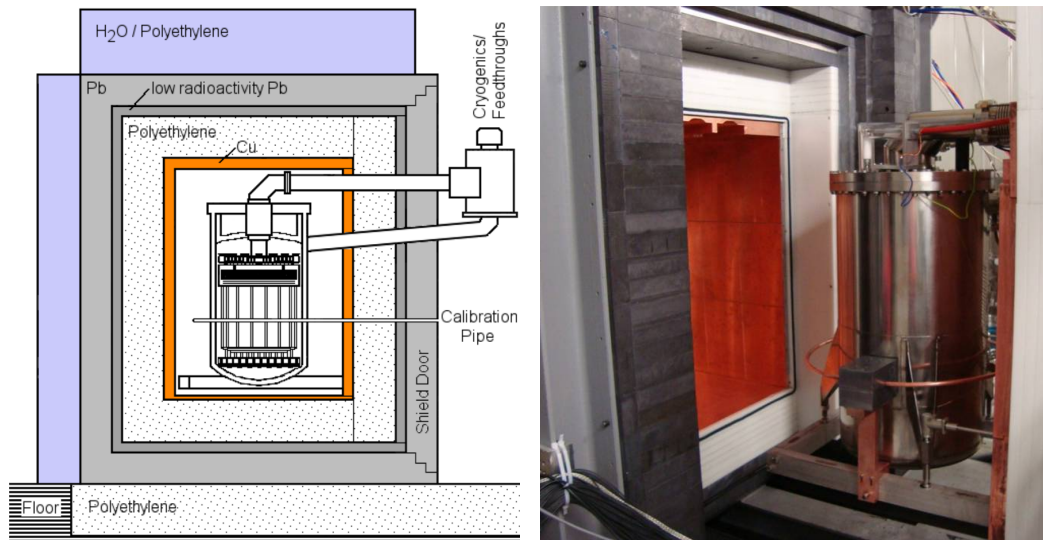
(a) Schematic drawing of the structure of the XENON100 experiment. The outer cryostat holds the TPC, whose liquid level is controlled by a diving bell system. It sits inside several layers of passive shielding material.

(b) Photo of the XENON100 experiment with opened shield. Clearly visible is the outer cryostat with its copper ring used to bring radioactive sources near the detector for calibration purposes.

Figure 2.6.: Schematic drawing (a) and picture (b) of the XENON100 experiment [5].

XENON100 was decommissioned in 2016 and its successor, the XENON1T experiment, see the description in the next section, was successfully running from 2016 to 2018.

2.4. The XENON1T Detector

With a total mass of roughly 3200 kg of ultra-pure liquid xenon, which is about $20\times$ more than used in XENON100, it is the first detector to surpass the 1 t mark of an active fuducial volume. Like the XENON100 detector before, it is located at the Laboratori Nazionali del Gran Sasso in Italy in Hall B, see figure 2.7. The rock of the massif above corresponds to an average depth of 3600 m water equivalent. The cylindrical TPC is approximately 97 cm long, 96-cm-wide and encloses (2004 ± 5) kg of liquid xenon, see figure 2.3 for illustration, while another ~1200 kg provides an additional shielding. The XENON1T vessel is mounted at the center of a water tank which has a diameter of 9.6 m and a height of 10 m, see figure 2.10b. In addition to shielding the TPC from the ambient radioactivity, the tank is also equipped with PMTs and acts as a muon detector and such as an active veto [8]. Next to the water tank an adjacent service building houses the xenon storage, the cryogenics plant, the data acquisition, and the slow control system as well as a small office for scientists staying underground, see figure 2.8.

The TPC operates equipped with 248×3 inch Hamamatsu R11410-21 PMTs arranged

Figure 2.7.: Illustration of the Underground lab inside the mountains of the Gran Sasso massif. The lab is reachable by car, taking a restricted exit inside the A24 highway tunnel after 6 km when entering in the direction towards L'Aquila. The XENON100 experiment was stationed on a side tunnel, XENON1T and its whole infrastructure is located in Hall B [64].

in two arrays above and below the liquid xenon target [10, 20], see figure 2.10a. Since this is a work with a focus on data analysis, only the parts needed during the analysis will be described in more detail in the next sections.

2.4.1. Data Acquisition and Software Trigger

The trigger of a data acquisition (DAQ) system is a submodule that decides if data should be recorded and stored or discarded. Usually data enters the DAQ as a continuous stream and the trigger is one of the first instances to reduce the amount of data that needs to be processed and/or stored. This makes the trigger an essential part of the whole system, since its decisions are final i.e. data without a trigger is lost forever.

In XENON1T, the trigger is implemented as a subsystem of the *event builder*. The event builder has to segment and encode the data stream, which is a nontrivial task, especially for the various types of calibration data or identifying double scatters or products of

Figure 2.8.: Picture of the the whole XENON1T experiment, situated in Hall B of the Laboratori Nazionali del Gran Sasso (LNGS) in Italy. On the left hand side the water tank is visible which sits right next to the three story service building with its glass walls. The ground floor holds the xenon storage system ReStoX and the purification column [15]. In the first floor are the DAQ system and slow control together with an office. The upper floor is home to the gas system [12].

whole decay chains like ^{214}BiPo. The event building ensures that events can be processed independently at a later stage. The whole trigger system in XENON1T is software, so the implementation of new features, extensions like monitoring tools is straight forward and can be done in a fast manner. The "untriggerd" data remains within the event builder pipeline for minutes to hours, depending on the data rate. So it is possible to also store data between two trigger windows. This way it is possible to compare to e.g. external triggers for diagnostic purposes.

Levelmeter (long)
Top PMT array
Diving Bell
Top TPC electrodes
Copper field shaping electrodes
PTFE reflector
Cable tray
PTFE pillars
PTFE HV screen
Bottom PMT array
Cathode
Cu/PTFE PMT support

0 10 20 30 40 50 cm
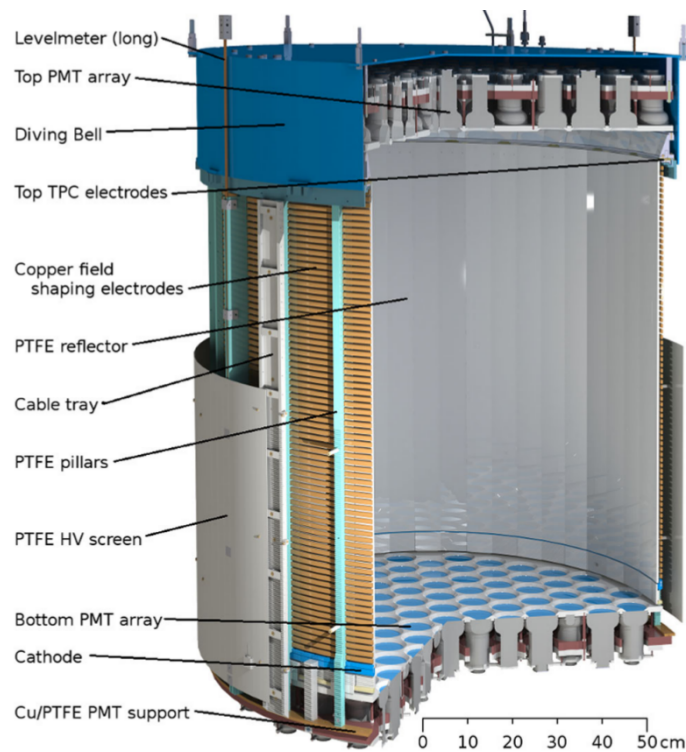
Figure 2.9.: Schematic drawing of the XENON1T TPC [15].

2.4.2. The Event Builder

A schematic of the whole DAQ system is illustrated in figure 2.11, showing most of the many subsystems and data flow. The arrow size and contrast are representative for the data transfer volume between the subsystems.

Following this illustration, the initial stages are the *digitizers*. There is one digitizer for each of the 248 PMT channels, that sends the pulses to the eight reader PCs. A pulse is the most fundamental signal in the XENON1T DAQ. It represents a short ~1 μs block of samples from a digitizer. The software running on the reader PCs is *Kodiaq* [37]. It manages the readout processes and already computes some basic quantities for each pulse, e.g. the baseline or the integral. The calculated quantities are stored along with the actual pulse data into a database which runs *mongoDB*. mongoDB is a multi-host no-SQL type database, which is open source [72]. There are three instances of mongoDB running on different machines. Each reader is assigned to one of these databases to ensure the consistency of write and read operations that happen simultaneously in most cases.

The next stage is called the event builder. It consists of several subsystems itself. The software runs multiple times as processes distributed over different machines. It reads the "untriggered" data from the mongoDB instances, looks for a trigger (which is usually an S2) an stores all the pulses in a defined window around around the trigger time into a raw data file. The event builder has three stages to manage this:
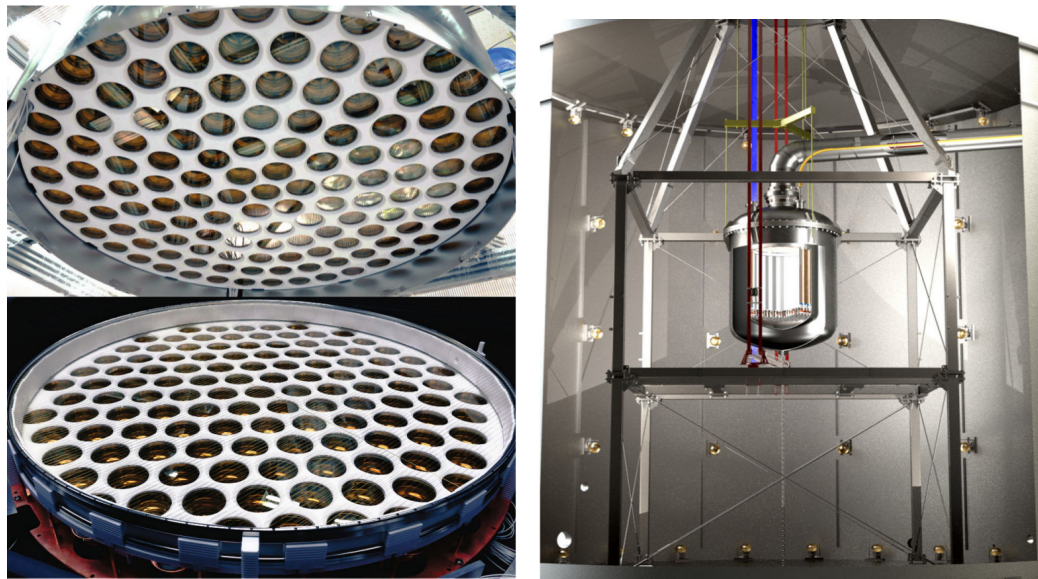
(a) Picture of the upper (top) and lower (bottom) PMT arrays of the XENON1T detector.

(b) Cryostat hanging inside the water tank surrounded by a support structure holding it in place.

Figure 2.10.: Pictures of the PMT arrays (a) and the cryostat inside the water tank (b) [15].

1. Input and trigger decision

2. Reading the data and compressing it

3. Writing the data to disk

In the *first stage* the event builder reads the summarized pulse information that has been provided by Kodiaq over mongoDB, i.e. the pulse start times, the PMT channels and, in cases it is available, also the integrated amplitude of the pulse's charge. With this basic information, the decision to keep or discard (trigger or not) the events is made in the trigger plugin. In the *second stage* several workers, i.e. processes waiting to receive event ranges to build, on several machines using several cores to pull the pulse information associated with the triggered event from mongoDB and encode as well as compress the data into the XENON1T's raw data format. The *third and final stage* is responsible for writing the triggered events to the storage disks. This is a single process that also restores the chronological order of the events that were distributed over several workers. In addition this stage also handles the deleting of old pulse data during calibration with high data throughput to maintain integrity and sufficient storage capacity.

Even for the low rate DM search data, not all information of the pulses is kept. The pulses just deliver the base for the calculations of higher level quantities. This is a separate process which is not further described in the scope of this work.

There are some additional components integral to the DAQ that are not shown in figure 2.11. These are mainly helpers and monitoring tools that support the main modules,
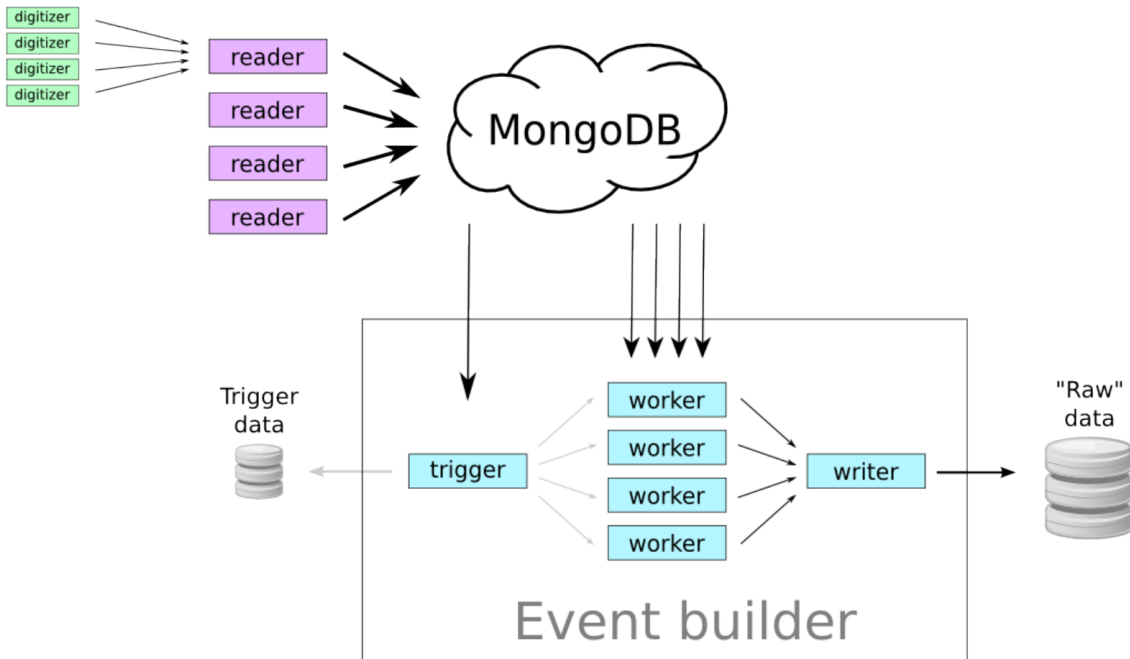
Figure 2.11.: Schematic representation of the XENON1T DAQ data flow. Arrow size represents the bandwidth and data transfer volume [1].

e.g. the rabbitMQ broker [80], a back-end that manages interprocess communication inside the event builder, or the runs database that is fed with the meta-data of the whole data taking procedure (e.g. date, time, operating shifters etc.).

There is also a *high energy veto*, an FPGA based board that monitors the data flow in real time. Its purpose is to throttle the digitizers (if needed) during high rate calibrations to be able to handle the dead-time more efficiently [16].

2.4.3. Trigger Data Structure and Pipeline

As already mentioned in the previous section, the pulse is the most fundamental unit of information in the data. It is a short block of samples coming from a single channel (digitizer). In contrast to the common DAQ configurations of other low background/sparse event experiments, the digitizers will send a pulse to the readers whenever a configurable threshold is exceeded in a single channel. This operation style is called self-triggering or trigger-less readout.

After processing, the essential unit of the data is the *event*. An event is a collection of pulses from all participating channels. The processing of data is also stateless, meaning that the processing of an individual event gives the same result as processing it in the middle of a dataset. For this to work, the time period that is allocated for an event has to be large enough to include all relevant signals. Only in that case the interpretation of the main physical interaction, in particular the pairing of S1 and S2, can be decided in a

unique manner.

The trigger consists of several plugins and itself is a plugin of the event builder discussed before. It has a pipeline like structure where each stage adds some information contributing to the final trigger decision. The abstraction grows in each stage: The first stage e.g. handles individual starting pulse times, where later stages already handle summarized information of grouped pulses.
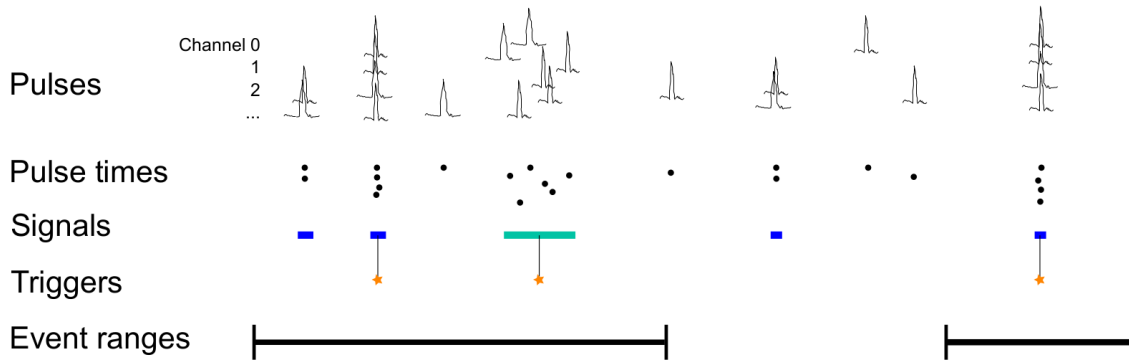
Figure 2.12.: Software trigger pipeline of the XENON1T trigger subsystem. The start times of the pulses are grouped into signals. Blue indicates an S1 like signal, cyan an S2 like signal. The stars denote a signal, which caused a trigger [1].

Figure 2.12 shows these different stages that lead to the final trigger decision:

1. In the initial stage *Pulses*, the trigger reads the prepared summarized information of the previous event builder stage. Here, only the pulse start times are relevant, all the other pulse information is not yet requested.

2. The *Pulse times* are grouped into *Signals*. Signals consist of pulses closely clustered in time. To separate a signal from the next, two successive pulses have to exceed the threshold of $1\,\mu s$, which is currently set in the trigger configuration. Otherwise the acquisition window is extended and the pulses are added to the same signal. This timing is already too generous to split close and large S2s or e.g. high energy S1s coming from ^{83m}Kr. But since the interest is to have a trigger decision and not to finally classify and separate single interactions this is still fine. It is a later task in the processing chain to separate these signals. Though it does explain, why in the end there are more peaks (grouped and classified clusters of pulses identified by the processing software PAX [60]), than there are signals in the trigger.

3. In the next step of the trigger pipeline, basic properties like the total number of contributing channels and the standard deviation of the pulse start times are computed. A classification of the different signals is done using just these two quantities. Signals get tagged as *S1*s candidates (blue in figure 2.12), *S2*s candidates (green in figure 2.12) or as *unknown*.
To be classified as an S1 or S2 signal, at least 10 pulses have to be involved. This

is still small enough to tag the roughly 22 pulses big single electron S2s but is already big enough to avoid the categorization of coincident PMT noise. The trigger logic is able to identify S1 and S2 signals by comparing the time coincidence, which is around 100 ns for S1 signals, in contrast to the broader distributed S2 signals. Of course, XENON1T is still sensitive to smaller S1s, but these will be found and tagged via the corresponding S2 trigger at a later step in the processing chain.

4. Now, that the signals are tagged, the decision if the signal will causes a trigger is made. An S1 candidate has to have at least 50 individual pulses to cause a trigger, S2 candidates on the other hand must already include more or equal to 60 pulses. This choice was made to avoid constant triggers due to pile-up of e.g. single electrons during the delayed extraction tails of large S2s, while still keeping the S2 threshold as low as possible.

5. The final step is to define a range around the trigger to group nearby triggers together. Roughly 1 ms before and after the trigger is stored. This is a little bit more than the maximum drift time an electron can have inside the XENON1T TPC for a very deep interaction. Events that overlap are grouped together as a result of this configuration and have to be disentangled at a later stage.

The information of the trigger, the classification tag and the actual trigger flag is stored as part of the event. The raw pulse data is omitted since this would be in contrast to the reduction of the amount of data that has to be handled [1].

2.4.4. Recent Results of the XENON1T Direct DM Search

Closing this chapter, the most recent results of the XENON1T Dark Matter search will be presented. As of today, the XENON1T detector is the most sensitive and biggest detector of its kind. In the summer of 2018 a study using 278.8 days of collected data utilizing a fiducial mass of (1.30 ± 0.01) t, resulting in a 1 t×year exposure was published [9]. Sadly no statistical significant signal has been measured. The data, see figure 2.13, was consistent with the background only hypothesis using a profile likelihood analysis. Nevertheless the most stringent upper limit for the WIMP-nucleon spin independent elastic cross-section for WIMP masses above 6 GeV could be archived, with a minimum of 4.1×10^{-47} cm^2 at 30 GeV and 90 % confidence level, see figure 2.14.
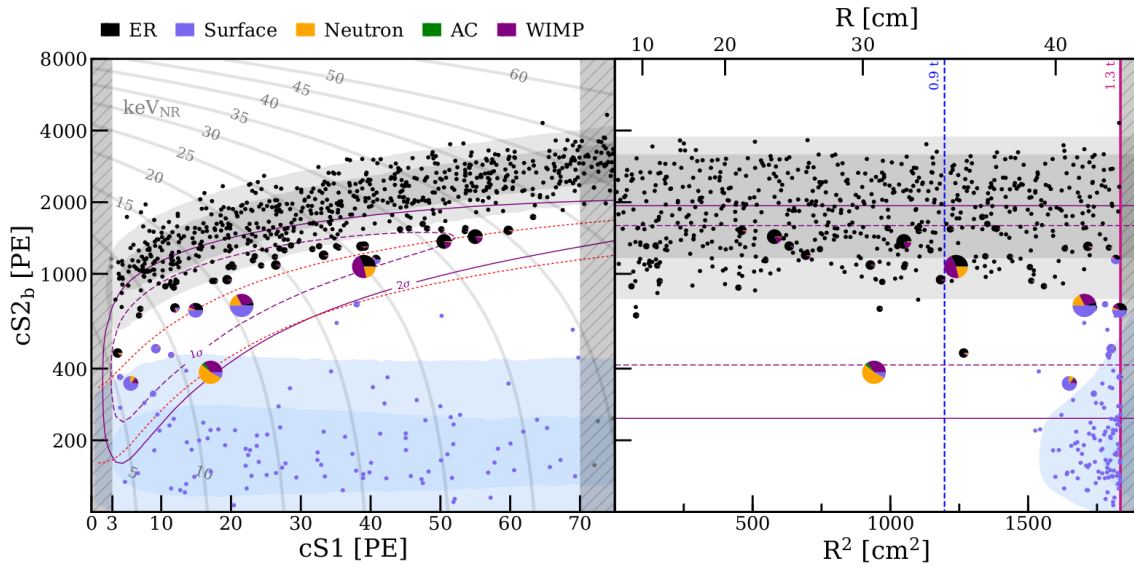
Figure 2.13.: DM search data in the 1.3 t fiducial volume distributed in cS1-cS2$_b$ (left) and R^2-cS2$_b$ (right) parameter spaces. Events that pass all selection criteria and are within the fiducial mass are drawn as pie charts representing the relative probabilities of the background and signal components for each event under the best-fit model with color code given in the legend. Small charts (mainly single-colored) correspond to unambiguously background-like events, while events with larger WIMP probability are drawn progressively larger. Shaded regions show the surface (blue) and ER (gray) background components for SR1. The 1σ (purple dashed) and 2σ (purple solid) percentiles of a 200 GeV/c^2 WIMP signal are overlaid for reference. Vertical shaded regions are outside the region of interest. The NR signal reference region (left, between the two red dotted lines) and the maximum radii (right) of the 0.9 t (blue dashed) and 1.3 t (magenta solid) masses are shown. Gray lines show iso-energy contours in NR energy [9].
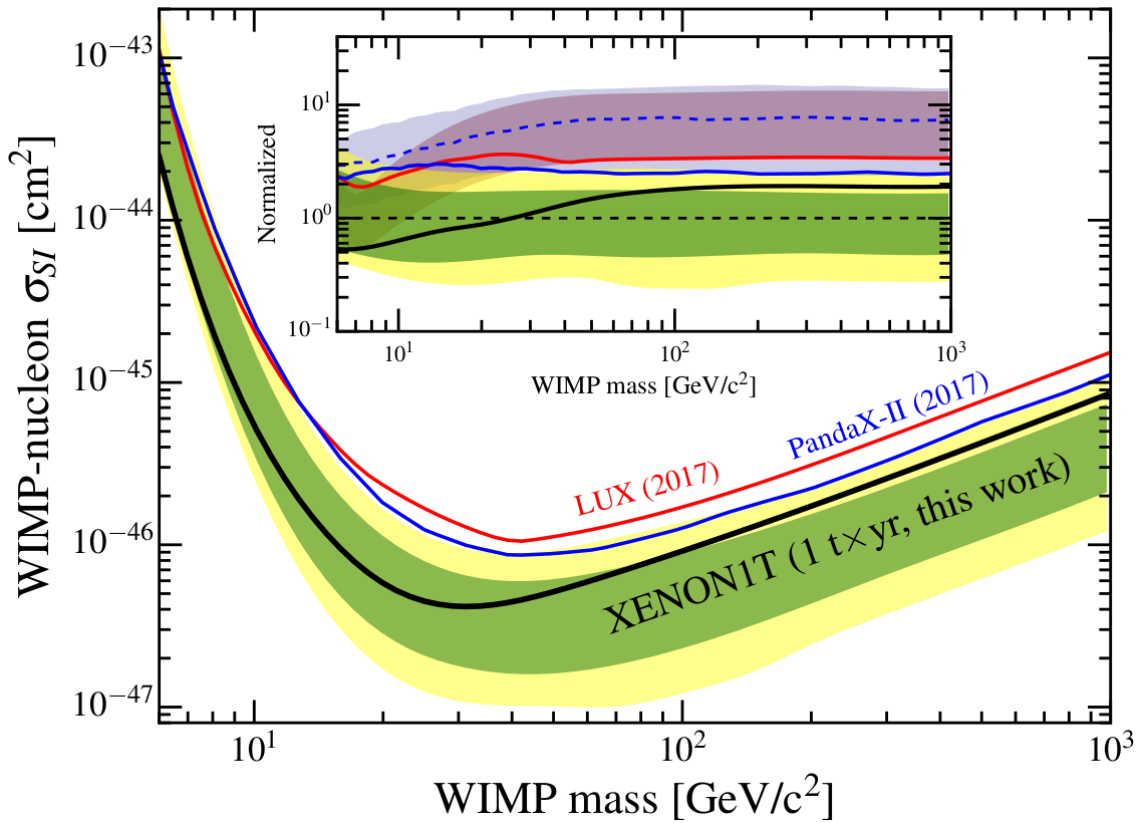
Figure 2.14.: 90% confidence level upper limit on the spin independent cross-section σ_{SI} (thick black line) with the 1σ (green) and 2σ (yellow) sensitivity bands. Previous results from LUX [65] and PandaX-II [75] are shown for comparison. The inset shows these limits and corresponding $\pm 1\sigma$ bands normalized to the median of the sensitivity band. The normalized median of the PandaX-II sensitivity band is shown as a dotted line [9].

Chapter 3

Statistical Inference

Statistical inference is an approach to deduce an underlying probability distribution using various techniques of data analysis. There are two main approaches to describe the statistics used in these analyses: The frequentist, often called the classical approach (since it has been the standatd approach for a long period in the past), and the Bayesian way. The terms "Bayesian" and "frequentist" stabilized already in the second half of the 20th century [46]. While being fundamentally different in their philosophies, both approaches still have a lot in common. Today, Bayesian inference is also a well established approach to statistics. The classical approach was developed also as a reaction to the (Bayesian) probability and the controversial principle of indifference [53]. That said, the classical interpretation of probability is Bayesian, but classical statistics is frequentist, since the this approach is the one referred to in current language most of the time when talking about statistics.

In Bayesian Inference some calculations that need to be performed, like numerical integration in higher dimensions, are computationally expensive and it just recently (in the last 10 years) became feasible to tackle problems using this method to its full extent. Since today computing power is not a limiting factor anymore, more and more scientists and also several sectors of industry are already using Bayesian statistics.

In this chapter the (philosophical) differences between the two approaches are discussed. Later, Bayes' theorem is derived as a consequence of conditional probability and the approach of how to use this for parameter estimation is shown.

3.1. Frequentist (classical) Inference

The common and often the first contact to statistics is to start with the frequentist point of view. The main aspects and ideas of this approach are [25]:

- The model parameters are fixed but unknown constants. They represent the numerical characteristics of the observed population.

- The interpretation of probability is always a relative frequency for a large set of measurements.

- The performance of statistical procedures is determined in the limit of an infinite number of hypothetical repetitions of an experiment.

To be able to make a statement about the probability of a variable, it has to be a random quantity. Since the parameters are unknown constants, no actual statement on their probability can be made. First, a sample statistic is needed that is randomly drawn from the population. A sampling distribution is created by considering all possible random samples. The parameter of the population will also be a parameter of the sampling distribution. A confidence statement about the parameter is made by converting the probability statement that is based on the statistic of the sampling distribution. The confidence is based on the average behavior of the procedure considering all possible samples.

3.2. Bayesian Interpretation of Probability

A basic characteristic of Bayesian methods to quantify uncertainty in inferences based on statistical analysis is the direct use of probability. There are three main steps that are involved in the process of Bayesian data analysis [51]:

1. A *full probability model*:
   There is a joint probability distribution for all observable and unobserved quantities in a problem. The knowledge of the underlying scientific problem and the data collection process should be consistent with the model.

2. Conditioning on observed data:
   The conditional probability distribution of the unobserved quantities of interest, given the observed data by calculating and interpreting the appropriate *posterior distribution*.

3. Evaluating the implications of the resulting posterior distribution and the fit of the model:
   Making statements on how well the model fits to the data, are the conclusions reasonable and how sensitive is a model to the assumptions from step 1? If needed, the model can be expanded or altered and the three steps can be repeated.

The main aspects that differ from the classic frequentist method can be summarized as follows:

- The model parameters themselves are also random variables due to the uncertainty about their true value.

- Inferences about the parameters are made by direct application of the rules of probability.

- Statements about the probability of a parameter must be interpreted as "degree of belief". Without further knowledge, the prior distribution should be subjective. Every person can have their own priors, also considering different weights of the

values of the parameters that are considered by each person. Though there are approaches using "non-informative" and "maximum-entropy" priors, this is out of the scope of this work and will not be explained any further.

- After getting new or additional data, the beliefs on the parameters are updated by using Bayes'theorem. This leads to an updated posterior distribution, which comes from two sources: The prior distributions and the observation of different, additional or new data.

This approach yields a consistent way of updating the beliefs about the parameters by looking at real data that has actually been measured. In contrast to the conventional frequentist approach with a fixed set of parameters, the inference is based on the data that has actually been observed and is not based on an ensemble of possible datasets that might have occurred or not. Since given the actual data, there is nothing random left with fixed parameters and only confidence statements can be made. So in this sense, allowing a parameter to be a random variable leads to probability statements posterior to the data.

The handling of nuisance parameters, parameters that are needed to describe the model but are of no interest, is done in a general straight forward manner. There is no general way of dealing with this in the frequentist statistics. There are of course also frequentist approaches that handle nuisance parameters, e.g. the profile likelihood method. Here the parameter dimensionality is reduced by expressing the nuisance parameters as functions of the parameters of interest [73].

What makes Bayesian statistics predictive, unlike the conventional way, is the possibility to easily find the conditional probability distribution of the next observation given the already measured sample data [25].

3.2.1. Conditional Probability and Bayes'Theorem

Consider two events, A and B, in the universe U, where

$$B_1 \cup B_2 \cup \cdots \cup B_n = U \tag{3.1}$$

and

$$B_i \cap B_j = \varnothing \text{ for } i \neq j. \tag{3.2}$$

Now the question is, if event A has occurred, what influence can this have on the probability of event B occurring? This is a typical question of conditional probabilities.

Assuming event A has occurred, everything outside the universe of A is no longer possible, the whole universe U has been reduced to $U_r = A$. Now, only the part of B that also lies in the reduced universe of A, i.e. $A \cap B$ can occur (see Fig. 3.1a).

The probability of B given A is the unconditional probability of the part of B that is also in A normalized by the scale factor $P(A)$ since the total probability in the reduced universe U_r has to remain 1. This leads to the conditional probability of B given A:

$$P(B|A) = \frac{P(A \cap B)}{P(A)}. \tag{3.3}$$
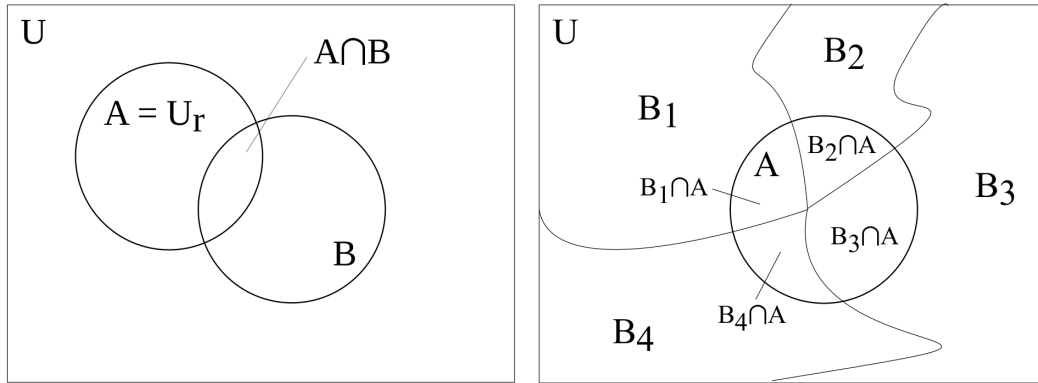
(a) Universe U reduced by Event A to U_r. Now only the parts of B also lying in $A = U_r$ can occur.

(b) Universe U divided by $n = 4$ events. Only parts of B_i (where $i = 1, \ldots, 4$) also lying in A can occur.

Figure 3.1.: Conditional probability [25]

With the conditional probability given and knowing that for independent events

$$P(B \cap A) = P(A) P(B) \tag{3.4}$$

we can also write (3.3) as

$$P(B|A) = P(B). \tag{3.5}$$

Assuming A and B are independent, the probability of B occurring is not affected by the knowledge that A already occurred. This can be turned around of course, so the result of A given B can be written as

$$P(A|B) = \frac{P(A \cap B)}{P(B)}. \tag{3.6}$$

However, the conditions on A and B can be different. Assume B is an unobserved event, so there is nothing known about the occurrence or nonoccurence of B. A on the other hand is an observable event that can either occur with B or its complement $\bar{B}$. The probability that A occurs may depend on the occurrence of B or $\bar{B}$. After clearing the fractions, (3.3) leads to the relationship for the conditional probability of an observable given an unobserved event, which leads to the joint probabilities

$$P(A \cap B) = P(B) P(A|B) \text{ and} \tag{3.7}$$
$$P(A \cap \bar{B}) = P(\bar{B}) P(A|\bar{B}). \tag{3.8}$$

This is also called the multiplication rule for probability. With conditional probability in mind, it is known that the marginal probability of event A is the sum over its disjoint parts:

$$P(A) = P(A \cap B) + P(A \cap \bar{B}). \tag{3.9}$$

Using this expression and plugging it into (3.3) yields

$$P(B|A) = \frac{P(A \cap B)}{P(A \cap B) + P(A \cap \bar{B})}. \tag{3.10}$$

Further, using the multiplication rule from (3.7) and (3.8), the final equation

$$P(B|A) = \frac{P(A|B) \, P(B)}{P(A|B) \, P(B) + P(A|\bar{B}) \, P(\bar{B})}. \tag{3.11}$$

is also known as *Bayes' theorem* describing a single event.

The two events B and $\bar{B}$ partition the universe, since $B \cup \bar{B} = U$ but also the events itself are distinct. Bayes' theorem can be generalized to n events, dividing the universe into n parts, see also Fig. 3.1b:

$$P(B_i|A) = \frac{P(A|B_i) \, P(B_i)}{\sum_{j=1}^{n} P(A|B_j) \, P(B_j)}. \tag{3.12}$$

This is Bayes' theorem as published posthumously in 1763, named after its discoverer Thomas Bayes, an English mathematician and Presbyterian minister.

3.2.2. Bayes'Theorem for Parameter Estimation

For later use we identify the different parts of Bayes' theorem to match our problem, introduce further terminology and make it ready to handle continuous variables and distributions. It will be used to estimate the parameters to match a measured dataset or, in other words, the probability of the parameters $\vec{\Theta}$ given the data X, the *posterior* probability:

$$\mathcal{P}(\vec{\Theta}|X) = \frac{\mathcal{L}(X|\vec{\Theta}) \, \pi(\vec{\Theta})}{\int \mathcal{L}(X|\vec{\Theta}) \, \pi(\vec{\Theta}) \mathrm{d}\vec{\Theta}}. \tag{3.13}$$

It equals the probability of the data given the parameters $\mathcal{L}(X|\vec{\Theta})$, the *likelihood*, times the initial probability of the parameters $\pi(\vec{\Theta})$, the *prior* probability. It is normalized by the integral of the likelihood times the prior probability over the allowed range of all parameters, $\int \mathcal{L}(X|\vec{\Theta}) \cdot \pi(\vec{\Theta}) \mathrm{d}\vec{\Theta}$. Note that now continuous values are assumed, resulting in the integral in (3.13) instead of the sum in (3.12).

It can be considered as a process of learning, as the prior knowledge about the parameters is updated in the light of new data gathered resulting in posterior knowledge,see figure 3.2 for the illustration of the influence of the prior and the likelihood on the posterior.

The handling of nuisance parameters in Bayesian inference is straight forward. In the process of sampling with Markov Chain Monte Carlo (MCMC) the parameters are integrated out. Let

$$\pi(\vec{\Theta}, \vec{\lambda}) = \pi(\vec{\Theta})\pi(\vec{\lambda}|\vec{\Theta}) \tag{3.14}$$
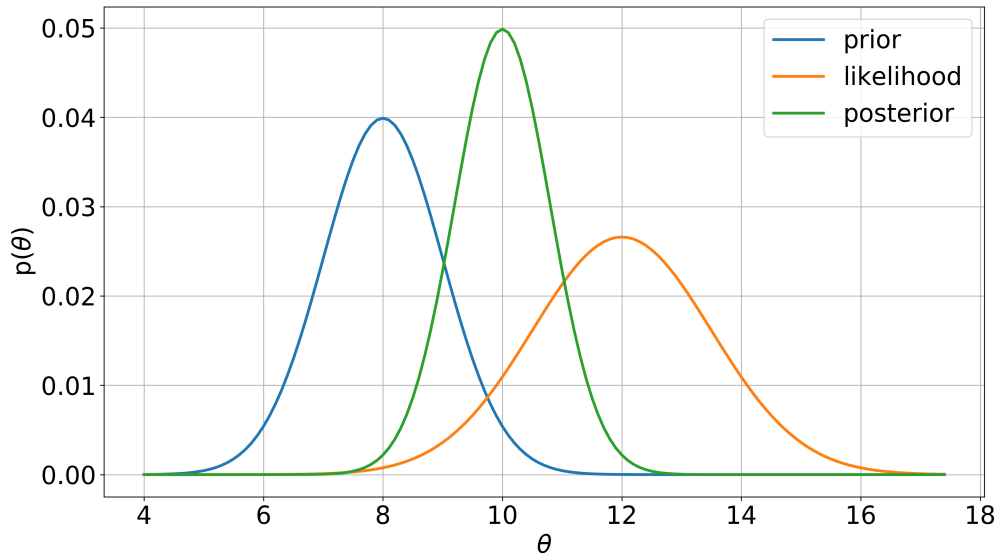
Figure 3.2.: Illustration of the influence of the prior probability density function (pdf) and likelihood on the posterior pdf. The likelihood, which describes the probability of the data given a model, is clearly influenced by the prior, which could e.g. a former measurement.

be the prior pdf. The inference then will be based on the marginal posterior of $\vec{\Theta}$ given the data X:

$$\mathcal{P}(\vec{\Theta}|X) = \frac{\pi(\vec{\Theta}) \int_{\vec{\lambda}} \mathcal{L}(X|\vec{\Theta}, \vec{\lambda}) \pi(\vec{\lambda}, \vec{\Theta}) d\vec{\lambda}}{\int_{\vec{\Theta}, \vec{\lambda}} \mathcal{L}(X|\vec{\Theta}, \vec{\lambda}) \pi(\vec{\Theta})) \pi(\vec{\lambda}, \vec{\Theta}) d\vec{\lambda} d\vec{\Theta}}. \tag{3.15}$$

This "tool" allows us to integrate out a large dimension of the nuisance parameter vector $\vec{\lambda}$ to make inference on the parameter of interest $\vec{\Theta}$ which can be multidimensional itself.

3.3. Markov Chain Monte Carlo (MCMC)

Markov Chain Monte Carlo methods are a well established tool for the simulation of stochastic processes having probability densities known up to a constant in many scientific disciplines. In the situation being unable to find or simulate independent realizations of some complicated stochastic process, it is most of the time as useful to be able to simulate dependent realizations and forming an irreducible Markov chain having the distribution of interest as its stationary distribution [52]. MCMC techniques are used to solve problems like integration or optimization in high dimensional space. In Bayesian inference, this can be found in the need for normalization (Bayes-Factor), in marginalization to get the posterior probability distribution or to calculate an expectation value.

Each of these applications share the need to solve integrals, often in high dimensional space which is only feasible numerically [4].

3.3.1. Markov Chains

A Markov chain is a model for stochastic systems whose states are governed by a transition probability. The states can be continuous or discrete. The current state in a Markov chain only depends on the most recent previous states, i.e. for a first order Markov chain only on the immediate previous one, see figure 3.3 for illustration. One of the most common Markov chains are Markovian random walks.
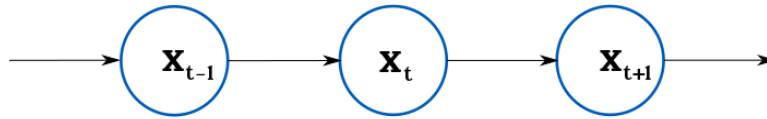
Figure 3.3.: Illustration of a first order Markov chain. The state x_t only depends on the state x_{t-1} and so on.

Mathematically speaking a Markov chain on finite state spaces x_t can only take s discrete values $x_t \in \mathcal{X} = \{x_1, x_2, \ldots, x_s\}$. This stochastic process fulfills the equation

$$p(x_t|x_{t-1}, \ldots, x_1) = T(x_t|x_{t-1}). \tag{3.16}$$

This chain is homogeneous if T remains invariant for all t with

$$\sum_{t=1,\ldots,S} T(x_t|x_{t-1}) = 1, \tag{3.17}$$

for any chosen t. In other words, the evolution of the chain in space $\mathcal{X}$ depends solely on the current state of the chain and a fixed transition matrix.

The following example will illustrate this even more: Consider a Markov Chain with 3 states, $S = 3$. The transition graph, in contrast to the previous first order graph in 3.3, is shown in figure 3.4.

The transition matrix for this graph is

$$T = \begin{bmatrix} 0 & 1 & 0 \\ 0 & 0.1 & 0.9 \\ 0.6 & 0.4 & 0 \end{bmatrix}. \tag{3.18}$$

Now a randomly initialized probability vector is chosen, e.g. $\mu(x_1) = (0.5, 0.2, 0.3)$. Applying the transition matrix a first time yields $\mu(x_1)T = (0.2, 0.6, 0.2)$ and after several more iterations $\mu(x_1)T^t$ the product converges to $p(x) = (0.2, 0.4, 0.4)$. For any given random starting point, the chain will converge to the invariant distribution $p(x)$, as long as T is a transition matrix that follows the properties:
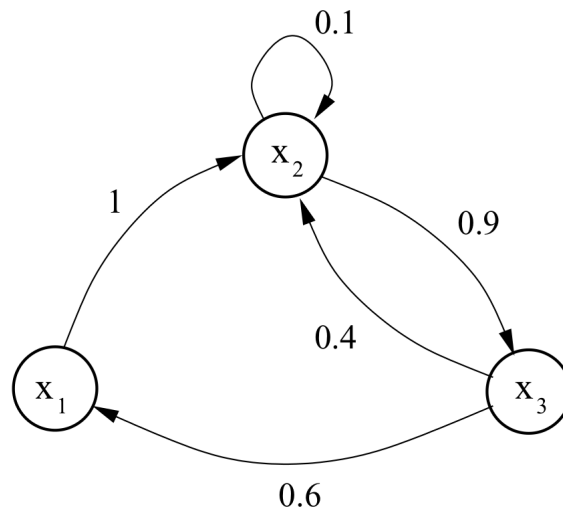
Figure 3.4.: Transition matrix for a Markov chain for $S = 3$ states with $\mathcal{X} = \{x_1, x_2, x_3\}$ [4].

1. Irreducibility:
   There is a positive probability that all other states are visited for any state of the Markov chain. This induces, that T can not be reduced to separate smaller matrices, which is the same statement as demanding that the transition graph is connected.

2. Aperiodicity:
   The Markov chain is not allowed to be trapped in infinite cycles.

These properties play a fundamental role in MCMC simulations, since a sampler has to be an irreducible and aperiodic Markov chain that has the target distribution as the invariant distribution [4].

In this context, also the term "Monte Carlo" can be explained: It is a general purpose technique for generating (simulating) fair samples from a probability distribution in (but not necessarily) high-dimensional space, using random numbers drawn from a uniform probability in a predefined range. In addition, by simulating a large enough sample, the mean, variance or any other characteristic of the desired function, e.g. the function itself, can be obtained to a desired degree of accuracy if the sample size is chosen large enough, see e.g. [43] for additional explanations.

3.3.2. Metropolis Hastings Algorithm

The Metropolis Hastings MCMC approach [56] is a popular and simple but still very powerful algorithm. It consists of the following steps to approximate the function $f(\vec{x})$ by finding its invariant (stationary) distribution:

1. The chain is initialized at a random position $\vec{x}_t$.

2. From the proposal distribution $q(\vec{y}|\vec{x}_t)$ a point $\vec{y}$ is generated.

3. The point $\vec{y}$ is accepted with the probability $\alpha(\vec{x}_t, \vec{y})$, where

$$\alpha(\vec{x}_t, \vec{y}) = \min\left(1, \frac{f(\vec{y})q(\vec{x}_t|\vec{y})}{f(\vec{x}_t)q(\vec{y}|\vec{x}_t)}\right). \tag{3.19}$$

4. If the point is accepted, then $\vec{x}_{t+1} = \vec{y}$ otherwise $\vec{x}_{t+1} = \vec{x}_t$ and the chain does not move.

As an illustration of the Metropolis Hastings algorithm, assume a Gaussian proposal distribution $q(\vec{y}|\vec{x}_t) = \mathcal{N}(\mu = \vec{x}_t, \sigma^2 = 100)$ and a bimodal target distribution $f(\vec{x}) \propto 0.3 \exp(-0.2x^2) + 0.7 \exp(-0.2(x-10)^2)$. The distribution together with four different stages of sampling up to 5000 iterations is shown in figure 3.5. It is clearly visible, that the sampled distribution converges towards the target distribution $f(\vec{x})$.
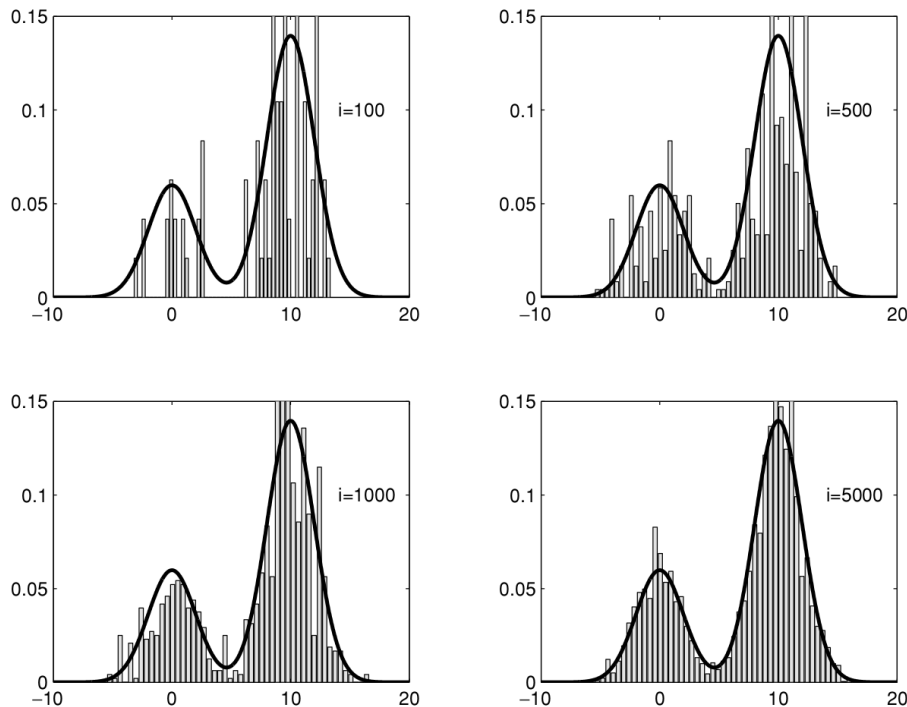
Figure 3.5.: Illustration of the Metropolis Hastings algorithm. The black line is the bimodal target distribution $f(\vec{x})$, the histogram shows the samples from the MCMC using the Metropolis Hastings algorithm. After i=5000 iterations it is obvious that the stationary state resembles the target distribution [4].

3.3.3. Ensemble Sampler with Affine Invariance

The family of Markov Chain Monte Carlo methods, whose performance is unaffected by affine transformations of space are called Ensemble Sampler with Affine Invariance.

While requiring almost no additional computational overhead, they should be very useful for sampling badly scaled distributions. Sometimes the underlying algorithm is also called the *stretch-move*.

This approach tries to tackle the following problem: Trial step-sizes that work well for a probability density $\pi(x)$, with $x \in \mathbb{R}$, may have a very poor performance for badly scaled densities, e.g.

$$\pi_\lambda(x) = \lambda^{-n} \pi(\lambda x), \tag{3.20}$$

if λ is very large or very small. To solve this issue a sampler that is independent of the scaling factor has to be found. Such a sampler was suggested in [54], which uses a family of many particle (ensemble) MCMC samplers, called walkers, with the affine invariance property. This invariance implies that the method should be independent of the aspect ratio in highly anisotropic distributions. Assume, e.g.,the two dimensional Gaussian distribution described by

$$\pi(x) \propto \exp\left(-\left[\frac{(x_1 - x_2)^2}{2\epsilon} + \frac{(x_1 + x_2)^2}{2}\right]\right), \tag{3.21}$$

which is drawn in figure 3.6.
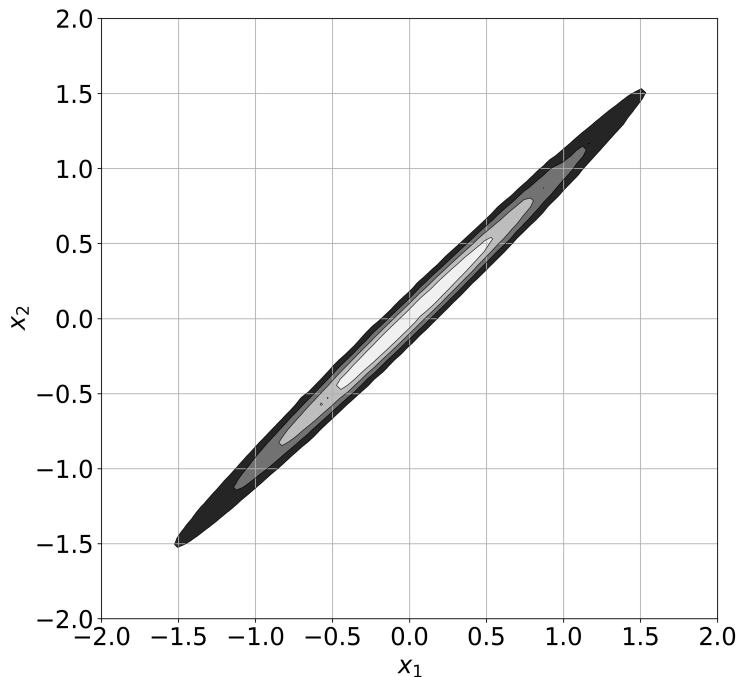
Figure 3.6.: Example of the Gaussian density defined in equation (3.21) for $\epsilon = 0.01$.

Since ϵ is a very small number greater zero, the distribution is very skewed in one dimension. Many standard samplers would have a bad performance with such a distribution e.g. the single variable Metropolis algorithm sampler that would be forced to perform perturbations of the order $\sqrt{\epsilon}$ and would be able to only slowly approach equilibrium.

The solution is to first apply an affine transformation. This transformation is an invertible mapping from $\mathbb{R}^n$ to $\mathbb{R}^n$ of the form

$$y = Ax + b. \tag{3.22}$$

If X has the probability density $\pi(x)$, the affine transformed density $Y = AX + b$ will take the form

$$\pi_{A,b}(y) = \pi_{A,b}(Ax + b) \propto \pi(x) \tag{3.23}$$

For the example distribution from equation (3.21) this would lead to the modified and much easier expression

$$\pi_A(y) \propto \exp(\frac{-(y_1 + y_2)^2}{2}) \tag{3.24}$$

after applying the affine transformation to its parameters of the form

$$y_1 = \frac{x_1 - x_2}{\sqrt{\epsilon}} \text{ and } y_2 = x_1 + x_2. \tag{3.25}$$

Equation (3.24) describes a well scaled density and does not require any further customization. From the point of the affine invariant sampler both distributions, (3.21) and (3.24), are equally difficult to sample from since the performance of its scheme is independent of ϵ.

After having learned about the affine transformation the next step is to introduce the concept of ensemble sampling. An ensemble X consists of L walkers, which can be seen as a vector on the n dimensional parameter space. An ensemble MCMC algorithm is a Markov chain on the state space of ensembles [54]. It requires to simultaneously evolve an ensemble of L walkers $X = \{X_1, X_2, \ldots, X_L\}$, where the proposal distribution for one walker l is based on the current position of the $L - 1$ walkers in the complementary ensemble $X_{[l]} = \{X_i \forall i \neq l\}$. In this case the term position refers to a vector in the n-dimensional parameter space.

The state of a walker at position X_l is updated by drawing one of the walkers X_i randomly from the remaining walkers $X_{[l]}$ and proposing a new position

$$X_l(t) \rightarrow Y = X_i + Z[X_l(t) - X_i], \tag{3.26}$$

where Z is drawn from a distribution $g(Z = z)$. If g satisfies

$$g(Z^{-1}) = z \cdot g(z) \tag{3.27}$$

the proposal is symmetric. The actual form of $g(z)$ is advocated to be

$$g(z) \propto \begin{cases} \frac{1}{\sqrt{z}}, & \text{if } z \in [1/a, a] \\ 0, & \text{otherwise} \end{cases}, \tag{3.28}$$

where a is an adjustable scale parameter that is e.g. set to 2 [54]. In this case the chain will satisfy detailed balance if the proposal is accepted with the probability

$$q = \min\left(1, Z^{n-1}\frac{p(Y)}{p(X_l(t))}\right), \tag{3.29}$$

where n again stands for the dimension of the parameter space. This process is then repeated for each walker in the ensemble one after another (in series) following the algorithm:

For $l = 1, \ldots, L$ do

1. Draw one of the walkers X_i from the ensemble X

2. $z = Z \sim g(z)$,following (3.28)

3. $Y = X_i + z[X_l(t) - X_i]$

4. $q = z^{n-1}p(Y)/p(X_l(t)$ (computationally most expensive step)

5. Draw u from $Uniform([0,1])$

6. If $u \le q$,see (3.29)
   $\rightarrow X_l(t+1) = Y$

7. else
   $\rightarrow X_l(t+1) = X_l(t)$

This algorithm is implemented in the python package emcee: The MCMC Hammer [47] and is the sampler of choice in the later analysis of Dark Matter parameter reconstructions in chapter 5.

Chapter 4

Data Driven Determination of the Software Trigger Efficiency for XENON1T

The XENON1T data acquisition system (DAQ) can be configured to trigger on S1 signals, S2 signals or any logical combination between those two signals. Since the interest lies in the detection of low energy events, the S2 trigger is of much more importance. For low energy events the single S1 signals of the interactions are too small to cause a reliable trigger, as we will see later in this chapter. The corresponding S2 signals, which are much bigger by detector design with its charge amplification, play the leading role in the trigger efficiency of low energy events. Knowing the S2 trigger efficiency is of particular interest to estimate the lower S2 analysis threshold. Within the analysis chain of the experiment, there are two methods used to determine the trigger efficiency: Running the trigger on simulated S2 wave forms, using a waveform simulator, and the data driven approach using collected calibration data. This work deals with the data driven approach, for the results using simulated wave forms see e. g. [1].

4.1. Method

The data structure after processing is slightly different than the structure that has been used in the event builder description. Sometimes the same syntax with different meaning is used, so one has to be especially careful. The event builder discussed earlier, starts from the bottom with fundamental information of the signals and builds up the event structure. In contrast, after processing, the data is available in a top-bottom structure starting with rather abstract information. The first level layer of the data is the *event*. It holds the abstract high-level information about the triggered event. Each event consists of at least one S1, S2 signal pair that has been reconstructed inside the active TPC volume. Pairs of grouped peaks are called *interactions*. The individual single S1 and S2 signals are stored as *peak* objects, which are a group of nearby *hits* across one or more PMT channels. The hits themselves are defined as a significant upward fluctuations in a single PMT channel. The lowest level of information is the *pulse*, which is a region of raw digitizer data, that is hardly used in analyses. For a detailed description of the event builder and processed data structure, see [16, 60].

To determine the trigger efficiencies using the processed data, the most important quantities are the trigger flags and the corresponding classifications that are stored as lists inside each event in one of the deeper levels of the data structure. The classification and peak finding inside the data processor and on the other hand the classification inside the trigger module are independent from each other. It is not possible to directly relate an S2 classified in the trigger with an S2 that has been identified by the data processor. The trigger only tells the DAQ to record and store data but it does not bias the classification of the data processor.

4.1.1. Obtaining and Selecting the Data

For each event the list of triggers with their corresponding classification is read and set into relationship with the main interaction of this event. There are four possible categories:

1. *Only an S1* trigger was recorded

2. *Only an S2* trigger was recorded

3. Both, *S1 and S2* triggers have been recorded

4. An *S1 or an S2* trigger has been recorded (all data)

Each trigger information is stored along with additional information of the first interaction of an event. In particular, the quantities needed at a later point of this analysis will be:

- s1, s2, cs1, cs2, event_number, run_number, trigger, trigger_flavor, z_position

To obtain the data of the corresponding main events, there is the possibility to select only the needed quantities in the data and store a subset for further analysis. These subsets of data have been labeled as minitrees. Minitrees are small, flat and tree like objects with one entry per event. They are generated from the data processor's native file format, have a standardized structure and contain a collection of previously selected standard quantities that are usually used in the XENON1T data analysis. Most analyses do not need all the information down to the level of individual pulses, so this information is omitted during the minitree creation to save storage space. Every analyst can access the standard minitrees, which are usually produced and stored by default at the different analysis facilities used by the XENON collaboration. From there on, each analyst can easily create their own custom minitrees, only containing the quantities needed for the specific analysis but at the same time keep the standardized format so everybody can use it afterwards to e. g. continue a study or perform a cross-check analysis.

The XENON1T analysts are also provided with many helper libraries, that have been (and still are) developed in a joint effort of the whole collaboration. The heavily used "Handy Analysis for Xenon" - *HAX* library is one of them. It contains a collection of tools and handy functions used throughout the whole analyses chain. HAX also provides the

needed functionality to read and write the above mentioned minitrees and also to add custom made minitree-makers for the use in a non-standard analysis like the one performed in this work. It reads the ".root" files that have been produced by the "Processor for Analysing Xenon" - *PAX* [60, 96] and usually hands back a pandas data frame [68]. Data frames are the commonly used data containers in the analysis and already provide a huge tool-set to manipulate or select data while being capable of handling huge amounts of data at the same time and still maintaining an acceptable performance.

A different library besides PAX and HAX is the "Lichens for Analysing Xenon" - *LAX*. It provides the interface to access the separately developed *data quality cuts*. But LAX does not just omits the data that did not pass a cut, it rather appends a column for each selected cut that is filled with a Boolean to the existing data frame. This gives the analyst the information if an event did (True) or did not (False) pass a quality cut. Using HAX again, events can be selected or omitted using dedicated cut functions that e.g. provide a full history of the cuts that have been applied.

Cuts have to be applied on the standard minitrees, since here all the needed quantities used by the cut functions are available. The resulting cleaned dataset will be used as a mask to select the corresponding data chosen from the custom minitree. This procedure is necessary since only the custom selected data contains the additional trigger information. The events are selected by their unique run and event id.

4.1.2. Custom Data Extractor (Tree-Maker) for the XENON Data Processor

To access the low level information of the trigger, a custom minitree maker had to be developed and fed into the HAX library. Even if it extracts much fewer quantities than the standard minitree maker it still has to crawl through much lower levels of the processed data, which in turn makes it much slower in performance compared to the standard one. For each event the list of trigger flags (1 for a signal that caused a trigger, 0 for a signal that did not) and the trigger classification (0 for "unknown", 1 for an identified S1 trigger and 2 for an S2 trigger) are extracted and saved along with e.g. event id and run number. In particular, the trigger classification is done by checking the spread (RMS) of start times of participating pulses:

```
def classify_signals(signals, s1_max_rms, s2_min_pulses):
    """
    Set the type field of signals to 0 (unknown), 1 (s1)
    or 2 (s2). Modifies signals in-place.
    """
    for signal_i, s in enumerate(signals):
        sigtype = 0
        if s.time_rms > s1_max_rms:
            if s.n_pulses >= s2_min_pulses:
                sigtype = 2
        else:
            sigtype = 1
        signals[signal_i].type = sigtype
```

where s1_max_rms= 70 and s2_min_pulses= 10 is set in the trigger configuration. This

separation is chosen, since the prompt scintillation light of an S1 signal shows much less spread than an S2 signal.

To make a statement on the efficiency of low energy events, the ^{241}AmBe calibration data was chosen. This is a commonly used neutron source with energies in the range of 2-10 MeV. This should produce nuclear recoils in the liquid xenon down to a few keV through elastic scattering. A calibration with this source is always done before a long dark matter search period, called a *sciencerun*. This work will look at two calibration datasets i.e. from sciencerun0 and sciencerun1 ^{241}AmBe data. Right from the beginning, the data is restricted to a low energy region, meaning only data with S1s < 100 pe and S2s < 10000 pe is extracted when using the various minitree makers. This can already be specified as an argument to the minitree maker function and saves a lot of computation time. Figures 4.1a and 4.1b show the uncut data in the even lower and more relevant energy region. It is clearly visible that, for both scienceruns, there is a strong population of events around cS1 = ~5 pe, cS2 = ~120 pe that also show tails in the horizontal and vertical direction. This is most probably junk due to pile up of single electrons or after pulses.

(a) Data from sciencerun0 ^{241}AmBe calibration

(b) Data from sciencerun1 ^{241}AmBe calibration
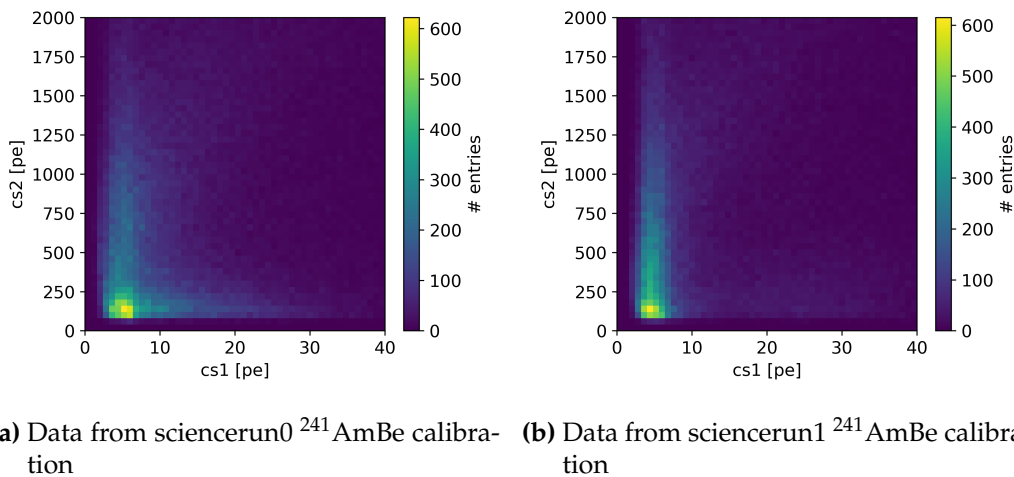
Figure 4.1.: Low energy region of the ^{241}AmBe dataset with no quality cuts applied yet. For both scienceruns there is a huge population of events around cS1 = ~4 pe, cS2 = ~120 pe. There is also a horizontal and vertical smearing of this population, which is probably due to pileup of single electrons and/or after pulses.

Single electrons that are extracted into the gas phase of the TPC generate signals of typically ~20-22 pe. They are very common signals in liquid xenon TPCs. It is already knwon from the XENON100 detector that single electrons are especially prominent after large signals and are caused by the photo ionization of impurities, photo ionization on exposed metal parts (e.g. the meshes inside the TPC) and also probably due to delayed extraction of charge out of the liquid after ordinary signals [2, 11]. A second known and common issue are after pulses of the PMTs. They appear after residual gas molecules

inside the vacuum part of the PMTs get ionized by photo electrons, drift towards the photo cathode and generate an additional weaker signal, following the signal which has been generated by the original interaction [30].

These hypotheses will be checked in the next section by applying several fundamental data quality cuts that have been designed to handle and get rid of these kind of known issues. In figures 4.2a and 4.2b again the uncut data is plotted, but this time using a logarithmic color scale. Here, possible substructures are better visible and strengthen the hypothesis that the nuclear recoils we are interested in are superimposed with a lot of unwanted background events (called "junk" in the following).
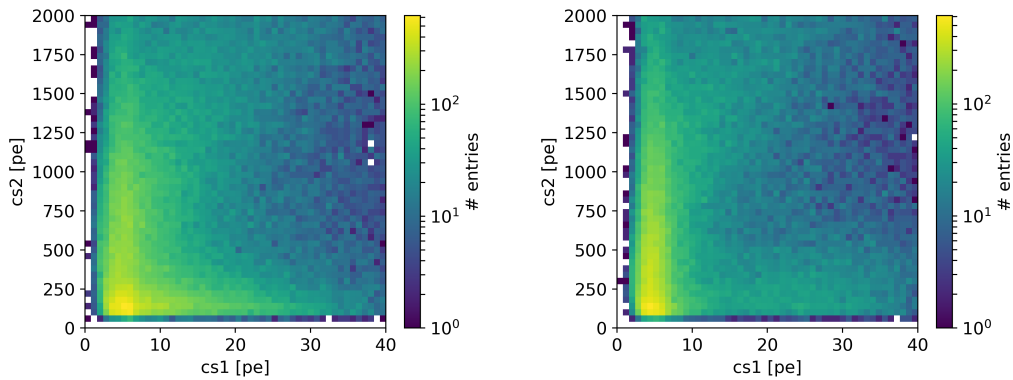
(a) Data from sciencerun0 ^{241}AmBe calibration

(b) Data from sciencerun1 ^{241}AmBe calibration

Figure 4.2.: Same data as in figure 4.1 but with logarithmic color scale to make the hidden nuclear recoil population more visible. Later applied quality cuts will carve out this part even better.

4.1.3. Data Selection and Quality Cuts

To clean the data from unwanted junk and to increase the data quality, 5 different cuts are applied:

- S1SingleScatter:
  Requires only a single valid interaction between the largest S2, and any S1 recorded before it [78].

- S1AreaFractionTop:
  Uses a modified version of the binomial from the scipy library to compute a p-value based on the observed number of s1 photons in the top array, given the expected probability (derived from ^{83m}Kr 32 keV line) that a photon at the event's position makes it to the top PMT array [67].

- S2Width:
  The S2 width cut compares the S2 width to what is expected based on diffusion according to its interaction depth in the detector. The inputs to this are the drift velocity and the diffusion constant, which both depend on the applied drift field. The allowed variation in S2 width is greater at low energies (since it is fluctuating statistically) [86, 102].

- PreS2Junk:
  Cuts events with a lot of peak area before the main S2. This cut was formerly known as "signal to noise cut" and is designed to reject events which definitely can't be analyzed due to misidentified peaks, shifted baselines or other conditions that can cause a very large amount of signal in the waveform in addition to the S1 and S2 [98, 99].

- S2AreaFractionTop:
  Cuts events with an unusual fraction of S2 on the top array. Primarily designed to cut gas events with a particularly large fraction of the S2 area on the top PMT array, also targets some strange or junk events with a low fraction of the S2 area on the top PMT array [26].

After the initial selection of the low energy region already during the minitree creation, table 4.1 shows what fraction of data is cut in addition by the quality cuts described above. From the applied cuts, S2Width and PreS2Junk have the biggest impact. This agrees with the hypothesis, that a lot of single electrons and after pulses (and their pileup) were involved in the chosen datasets at low energies since these cuts especially target those kind of unwanted events.

In figures 4.3a and 4.3b the remaining events after the cut are shown. The huge population and the horizontal and vertical "tails" are gone and a typical nuclear recoil event population of the neutrons scattering off the xenon nuclei remains. With this cleaned dataset, the actual trigger efficiencies will be calculated.

4.2. Results of the Data Driven Method

Now that the Data has been selected and properly cleaned, the actual data driven software trigger analysis can be performed. The focus will be set on the most important efficiency depending on the S2 signal, but we will also have a look at the S1 and z-position dependence for completeness. The results of the analysis will be compared to the results of a Monte-Carlo driven approach, which uses a waveform simulator to generate the data.

Table 4.1.: Summary of the applied cuts for the different science runs.

Cut	# before	# removed	% passed	Cumulative % left
Sciencerun 1				
S1SingleScatter	147104	1412	99.04	99.04
S1AreaFractionTop	145692	9238	93.66	92.76
S2Width	136454	65994	51.64	47.90
PreS2Junk	70460	22634	67.88	32.51
S2AreaFractionTop	47826	1147	97.60	31.73
Sciencerun 0				
S1SingleScatter	177644	5362	96.98	96.98
S1AreaFractionTop	172282	19867	88.47	85.80
S2Width	152415	62817	58.79	50.44
PreS2Junk	89598	36348	59.43	29.98
S2AreaFractionTop	53250	1360	97.45	29.21
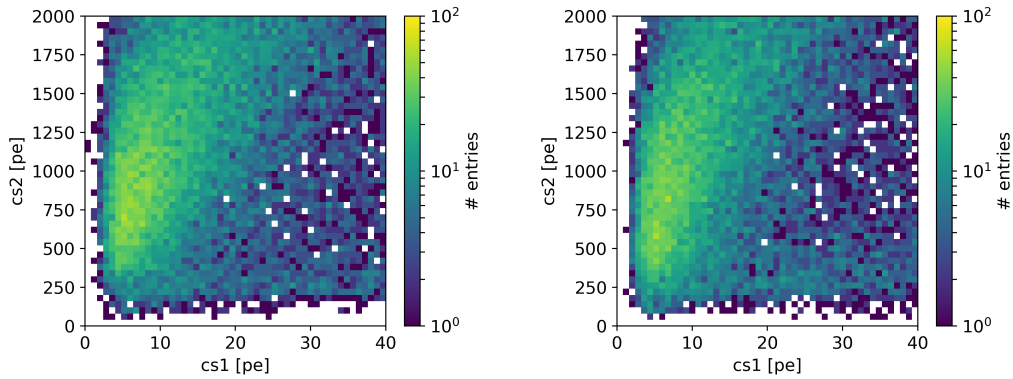
(a) Data from sciencerun0 ^{241}AmBe calibration after applying the data quality cuts from table 4.1.

(b) Data from sciencerun1 ^{241}AmBe calibration after applying the data quality cuts from table 4.1.

Figure 4.3.: Low energy region of the ^{241}Ambe calibration data with applied data quality cuts. The population of junk events and its horizontal/vertical tails is gone and the nuclear recoil band is now the prominent population.

4.2.1. S2 Dependence of the Efficiencies

To calculate the trigger efficiencies, the events are sorted into 4 different categories, as already described in section 4.1.1. In particular, the categories are:

1. S1 trigger only

2. *S2* trigger only

3. *S1 and* S2 trigger

4. *S1 or* S2 trigger (i. e. all the data)

   The above list is already ordered in terms of how many events are found for each condition, starting with the smallest population, i. e. S1 trigger only. After categorization, the events are sorted into histograms for further usage and visualization. Since the main interest lies in the estimation of the S2 trigger efficiency, the binning of the first histograms is chosen to be in S2 space accordingly, see figures 4.4 and 4.5.

   Even with over 300 h of AmBe calibration data for each individual sciencerun, we are left with a rather small statistic. It can already be said, that a dedicated measurement with a neutron source that produces a higher amount of low energy nuclear recoils would be beneficial for this analysis. Nevertheless, the S2 trigger efficiency can now be calculated by selecting events that have an S1 trigger but also have a valid S2 that has been found independently by the data processor. This is given by construction, since we only chose events whose interactions have a valid S1,S2 pair. In the next step it is checked if the event with an S1 trigger also contains a valid S2 trigger or, in other words, if the corresponding S2 found by the independent processor also would have caused a trigger in the DAQ.
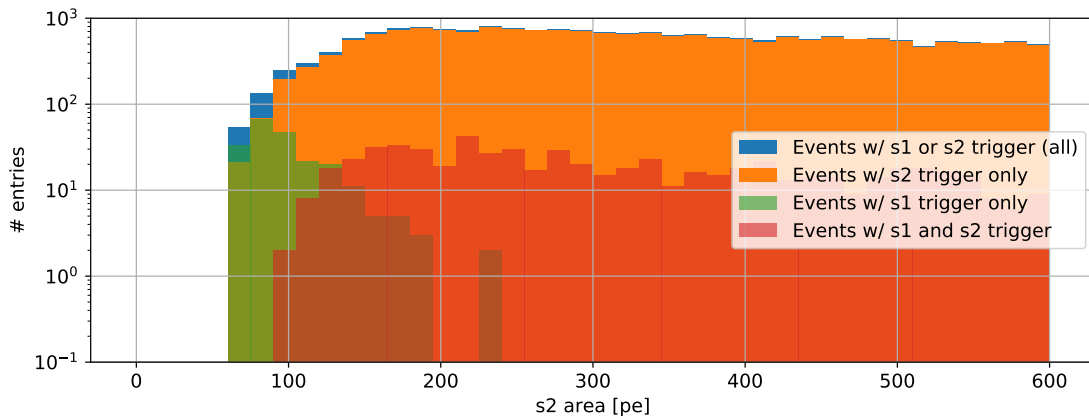
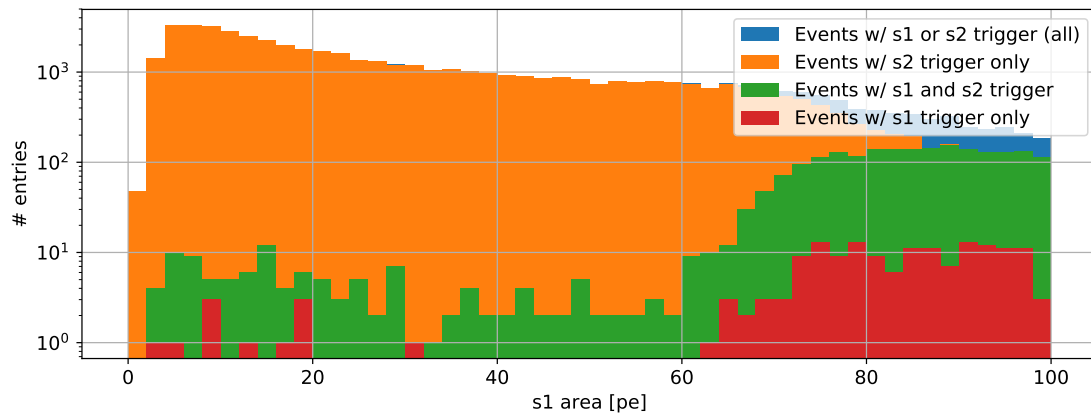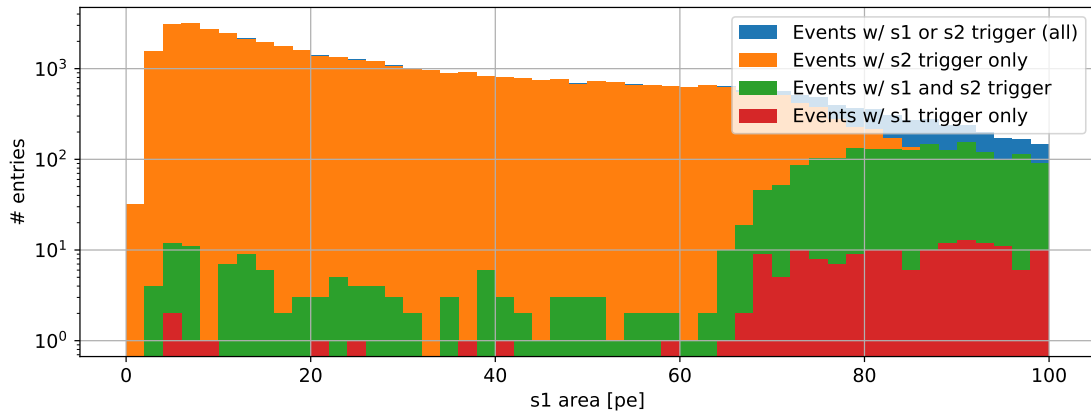**Figure 4.4.:** Histogram of the four different trigger categories in dependence of the uncorrected S2 area for sciencerun0.
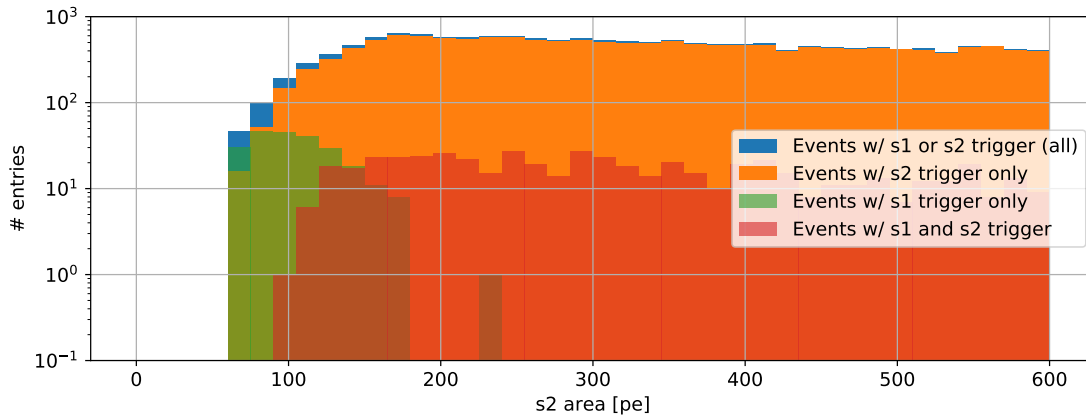
Figure 4.5.: Histogram of the four different trigger categories in dependence of the un-
corrected S2 area for sciencerun1.

For the S1 trigger efficiency, this is done analogously by looking at the S2 triggered events and checking for the S1 trigger afterwards. Finally, the efficiencies are calculated bin wise following

$$\epsilon_t^{S2}(S2) = 1 - \frac{t(S2)_{S1}}{t(S2)_{S1S2} + t(S2)_{S1}} = \frac{t(S2)_{S1S2}}{t(S2)_{S1S2} + t(S2)_{S1}} \tag{4.1}$$

for the S2 trigger efficiency and

$$\epsilon_t^{S1}(S2) = 1 - \frac{t(S2)_{S2}}{t(S2)_{S1S2} + t(S2)_{S2}} = \frac{t(S2)_{S1S2}}{t(S2)_{S1S2} + t(S2)_{S2}} \tag{4.2}$$

for the S1 trigger efficiency. Here $t(S2)_{S1}$ is the number of entries in the corresponding S2 bin for S1-only triggers, $t(S2)_{S2}$ is the number of entries in the corresponding S2 bin for S2-only triggers and finally $t(S2)_{S1S2}$ is the number of entries that have both, S1 and S2, triggers. The expression for the S1 case follows the same logic.

The results are shown in figures 4.6 and 4.7. The S2 trigger efficiency starts rising around 80 pe and reaches 100 % efficiency at around 180 pe for both science runs.

This result is a reliable cross-check to strengthen the conservative choice of the XENON1T analysis threshold of 200 pe in S2. The error-bars represent the binomial statistical error with a 95 % confidence level and also indicate the low statistics in some of the bins. For comparison, the efficiency using the simulated waveforms approach is shown, whose data is taken from [1]. Both approaches have their advantages: The simulation has no problem with low statistics but is heavily reliable on the model used in the waveform simulator and may be less conservative and yield higher overall efficiencies. On the other hand, the data driven method is model independent but is reliable on the data selection and other detector efficiencies and suffers heavily from low statistics. While there is a notable difference for both approaches, both agree on setting the analysis threshold to 200 pe is a meaningful choice.
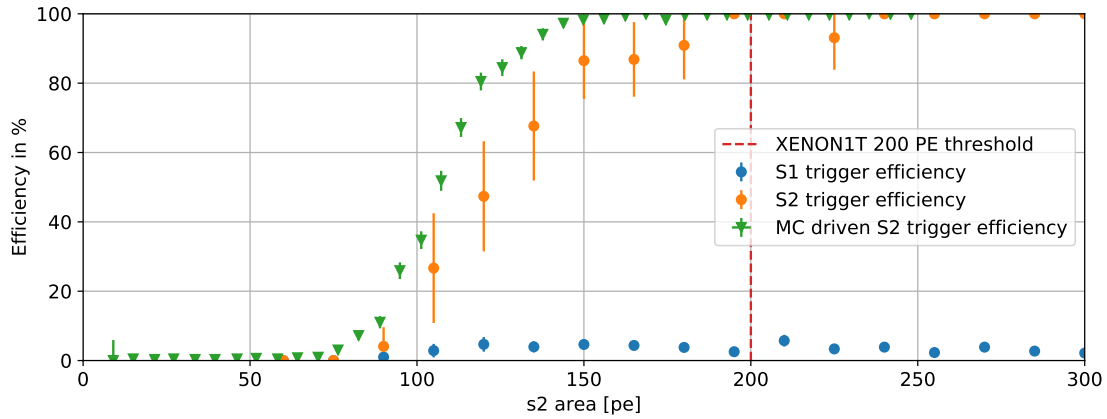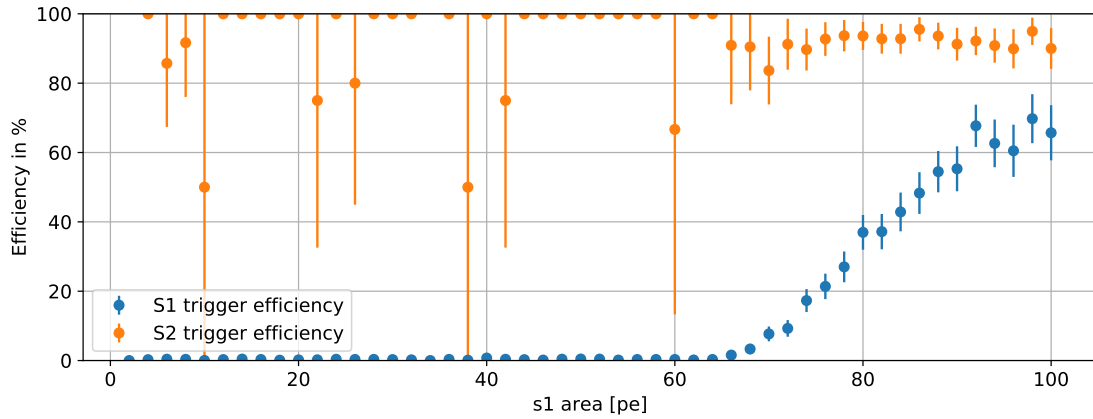
Figure 4.6.: Results for the S2 and S1 trigger efficiencies in dependence on the uncorrected S2 area for sciencerun0. The green data points are the results from the alternative approach using the waveform simulator.

Looking back at figures 4.4 and 4.5, we see that for the S1 trigger efficiency there are much more events left in the cleaned dataset. This is also reflected in the much smaller errors for this case. The efficiency of the S1 trigger remains small and seems more or less independent of the S2 size. This is no surprise, since even a very low energetic nuclear recoil, that produces an S1 of only a few photo electrons will already have a corresponding S2 that is in the order of hundreds or even up to a few thousand photo electrons. This explains why the S2 trigger efficiency is so important for the detection of low energy nuclear recoils: The S1 of low energy events would not be a reliable trigger, while the S2 is still big enough to be detected.

4.2.2. S1 Dependence of the Efficiencies

To get a different perspective, it is also possible to look at the S1 dependence of the two efficiencies. The calculations using equation (4.1) and (4.2) are therefore performed in dependence on the size of the S1, i. e. $\epsilon_t^{S2}(S1)$ and $\epsilon_t^{S1}(S1)$. Using this dependence results in the histograms shown in figures 4.8 and 4.9.

Using the same categorization as in the previous section, this leads to the efficiencies shown in figures 4.10 and 4.10 for sciencerun0 and sciencerun1 respectively. Looking at the S1 trigger efficiency it is clear, that nearly all low energy events below 60 pe (remember, the trigger condition is set to at least 50 pulses for an S1 flagged signal) would have been missed. From 60 pe onward, the efficiency rises continuously but never reaches or overtakes the S2 efficiency. This again emphasizes the importance of the S2 trigger efficiency, which stays well near to 100 % up to 60 pe. Apart from a few bins in between which suffer from low statistics, it is independent of S1 size until the S1 trigger efficiency itself starts rising at around 60 pe. Events that have an S1 signal already over 60 pe, typically have a huge associated S2 signal. Most certainly such an event would not be a Dark
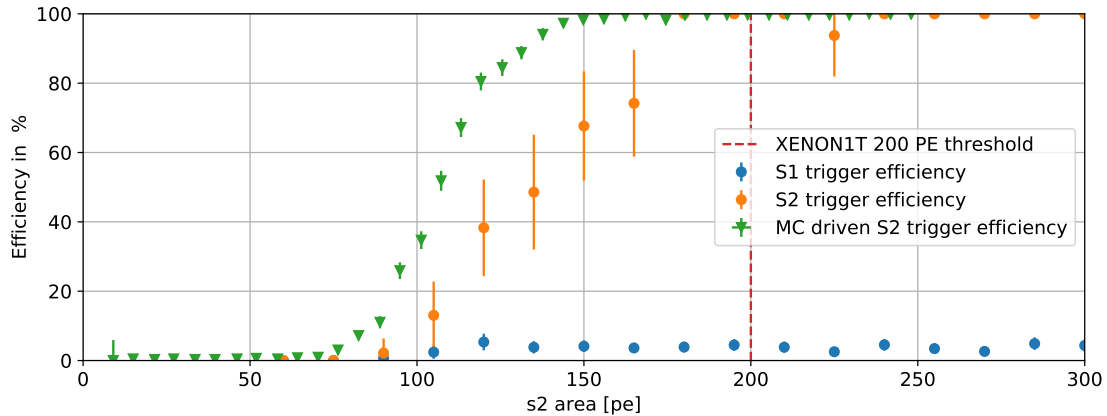
Figure 4.7.: Results for the S2 and S1 trigger efficiencies in dependence on the uncorrected S2 area for sciencerun1. The green data points are the result from the alternative approach using the waveform simulator.

Figure 4.8.: Histogram of the four different trigger categories in dependence of the uncorrected S1 area for sciencerun0.

Matter induced signal and is removed by e. g. the high energy veto. This is the effect visible in the region with a systematic lower S2 trigger efficiency above 60 pe.

4.2.3. Position (depth) Dependence of the Efficiencies

The last aspect of trigger efficiency that will be discussed in the scope of this thesis is the dependence on the interaction depth, i. e. on the z-position inside the TPC. Following the procedure of the two previous sections, the interactions are now filled into histograms depending on their position in z, i. e. $\epsilon_t^{S2}(z)$ and $\epsilon_t^{S1}(z)$, see figures 4.12 and 4.13. Despite the statistical uncertainties, there is no clear dependence visible regarding the interaction

Figure 4.9.: Histogram of the four different trigger categories in dependence of the un-corrected S1 area for sciencerun1.
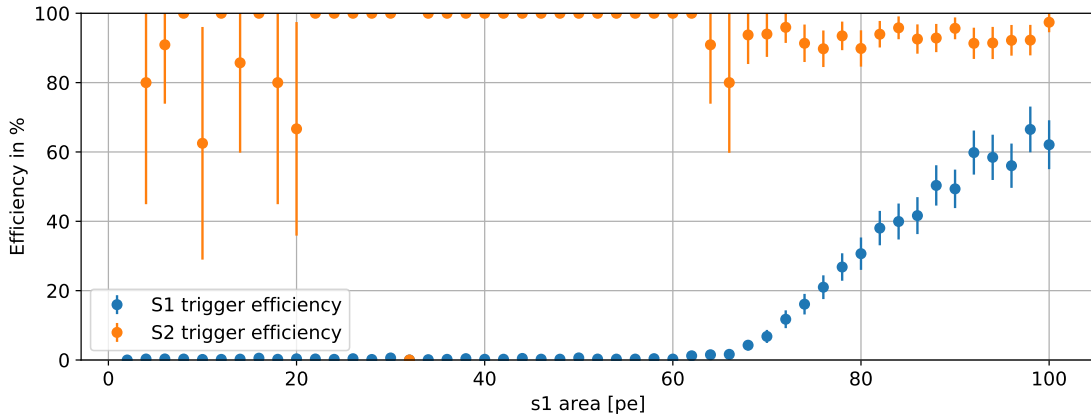
Figure 4.10.: Results for the S2 and S1 trigger efficiencies in dependence on the uncorrected S1 area for sciencerun0. The S2 efficiency seems to be independent of the size of the S1 signal, whereas the S1 efficiency clearly shows that only well above 60 pe triggers have been recorded.

depth for the S2 trigger efficiency. It stays rather constant over the whole z range. The errors become more prominent towards the top (0 cm) or bottom (-100 cm) of the TPC. Here, the quality and data selection cuts removed a lot of events and the statistics are reduced. Most of the events in these regions tend to be background from e.g. the radioactivity of the walls and PMTs themselves.

For the S1 trigger efficiency on the other hand, there is a trend visible. Most of the S1 light is collected by the bottom PMTs due to e.g. total reflection at the liquid/gas interface. This explains the slightly higher efficiency, the deeper the interactions take place. On

Figure 4.11.: Results for the S2 and S1 trigger efficiencies in dependence on the uncorrected S1 area for sciencerun1. Also in this sciencerun the S2 efficiency seems to be independent of the size of the S1 signal, whereas the S1 efficiency again shows that only well above 60 pe triggers have been recorded.
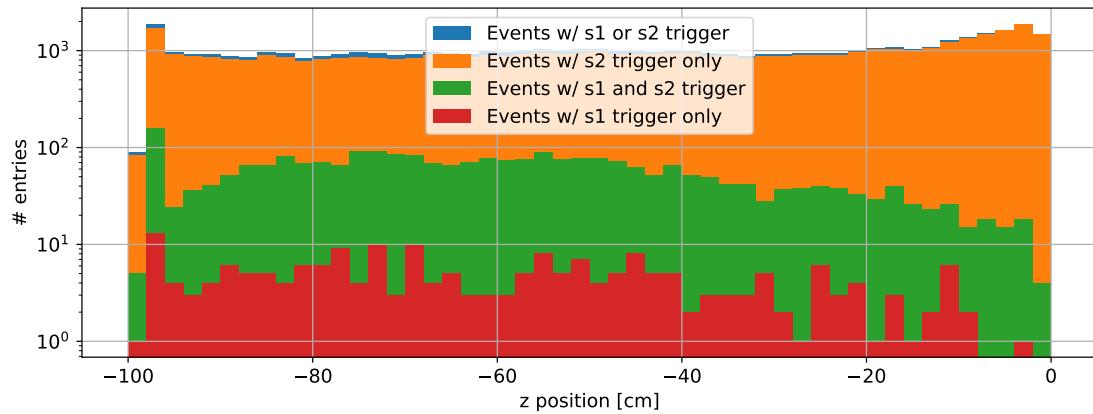
Figure 4.12.: Histogram of the four different trigger categories in dependence of the interaction depth z for sciencerun0.

the other hand, if the interactions get closer and closer to the bottom PMT array, the efficiency starts to drop again due to the event selection of the background cuts. This again reflects the fact that the cuts are tuned to get rid of (background) interactions close to the walls and PMT arrays. This is also the reason that for most of the standard analyses and especially for the DM search analysis a fiducial detector volume is chosen in addition to the background cuts.
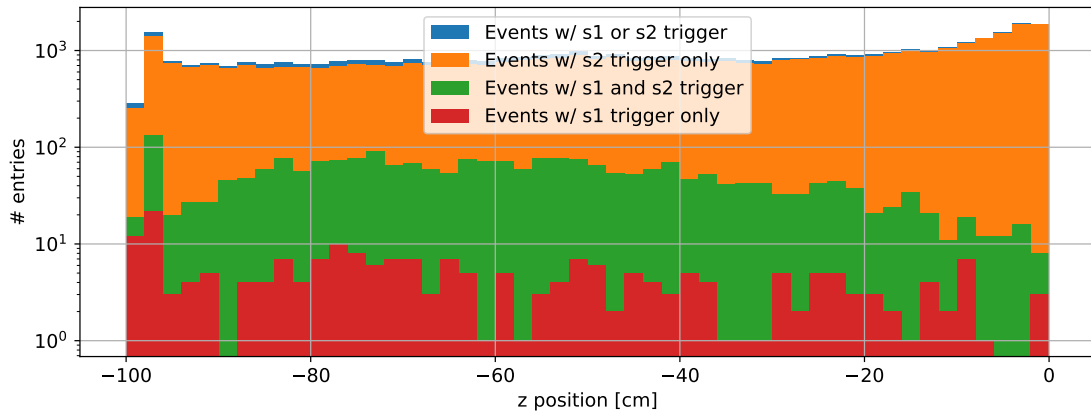
Figure 4.13.: Histogram of the four different trigger categories in dependence of the interaction depth z for sciencerun1.
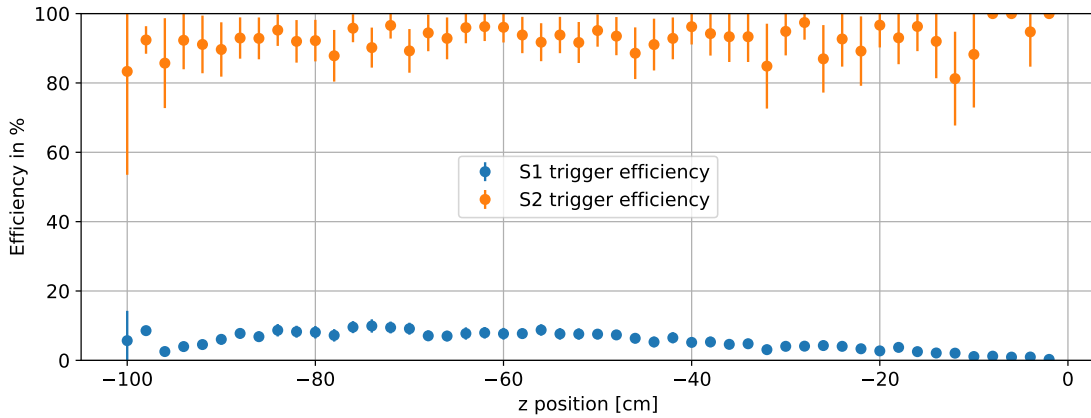
Figure 4.14.: Results for the S2 and S1 trigger efficiencies in dependence on the interaction depth z for sciencerun0. The S2 efficiency seems to be independent of the depth of interaction, whereas the S1 efficiency rises from the top of the TPC ($z=0$) until a certain point above the bottom PMT array. Since the majority of the S1 light is collected from the bottom PMTs, this growth in efficiency is as expected.

4.2.4. Summary of Results

The study in this chapter contributed an important cross-check on the chosen XENON1T S2 analysis threshold of 200 pe. After a thorough description on how the data for the analysis was obtained, selected and cleaned by writing custom minitree makers and applying different quality cuts, the trigger efficiencies are calculated. Overall, the results agree with the chosen XENON1T analysis S2 threshold for both data collection periods,
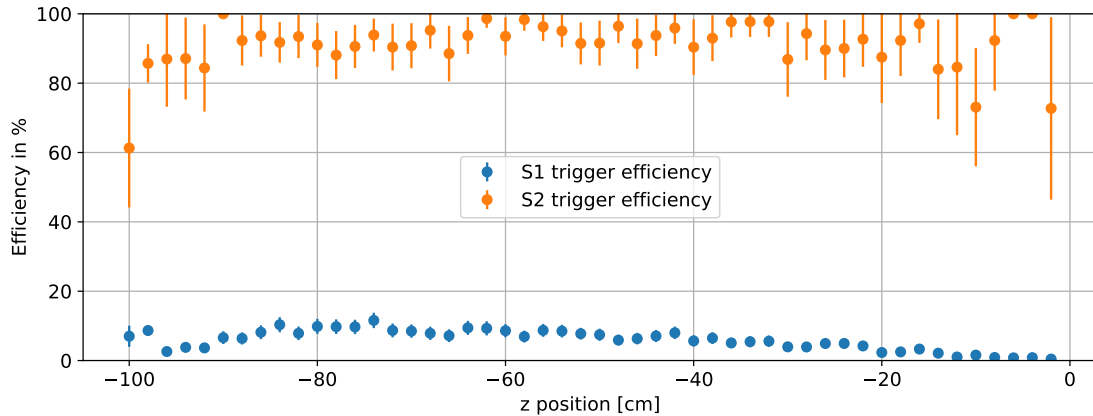
Figure 4.15.: Results for the S2 and S1 trigger efficiencies in dependence on the interaction depth z for sciencerun1. In this run the S2 efficiency seems also to be independent of the depth of interaction. The S1 efficiency also rises from the top of the TPC (z=0) until a certain point above the bottom PMT array. Since the majority of the S1 light is collected from the bottom PMTs, this growth in efficiency is as expected.

i.e. sciencerun0 and sciencerun1. The threshold could have been chosen to be as low as at ~180 pe but, to stay as conservative as possible, the choice of 200 pe has been favored by the XENON1T collaboration. These findings agree very well with the alternative study using a Monte Carlo simulation with a waveform simulator, that has been performed in an independent analysis [1].

Looking at the S1 dependence further strengthens the importance of the S2 trigger efficiency to detect low energy nuclear recoils. While the S2 efficiency seems to be mostly independent on the S1 signal, the S1 efficiency only starts to rise above 60 pe.

The interaction depth dependence can be seen as an intrinsic cross-check of the study, since it shows the expected behavior. While the S2 efficiency seems to be independent on the depth, the S1 efficiency is highest close (but not too close) to the bottom PMT array, where the prompt scintillation light has also the highest chance to reach a bottom PMT without getting lost on the way there.

Chapter 5

An Improved and Extended Signal-Model for the XENON Dual Phase TPC

This chapter describes a new generic signal model for xenon dual-phase Time Projection Chambers (TPCs) where the XENON100 detector parameters are implemented as a working example. In the Bayesian sense, the focus will be to use as much of already available information as possible. In contrast to earlier analyses of the XENON100 experiment, both signals (S1 and $S2_b$) are incorporated in their spatial dependent form into the likelihood functions and also later for Dark Matter parameter estimation. The spatial dependence is kept where possible instead of switching to the spatially averaged data space. Parameter estimation is formulated as a Bayesian hierarchical model and the detector and selection efficiencies will be included in a principled style. This work was done in close cooperation with Prof. Roberto Trotta from the Imperial College in London.

The model itself is developed in a modular way to be able to implement other detector configurations e.g. XENON1T in a straight forward manner. The first part deals with the necessary rework of the likelihood functions for both signals, i.e. $p(S1|E, \vec{r})$ in section 5.1 and $p(S2|E, \vec{r})$ in sections 5.2 and will be followed by invoking the detector signal efficiencies into the signal model in section 5.3. The chapter closes with the discussion of the posterior likelihood function for the Dark Matter parameter estimation, which is formulated in section 5.4.

5.1. Spatially Dependent Likelihood for the S1 Signal

In order to derive a spatially dependent likelihood for the $S1$ signal, consider an incoming particle that scatters off the target material creating a nuclear recoil (NR). This event k will have an interaction point $\mathbf{r} = (x, y, z)$ where $z = 0$ is defined at the liquid gas interface and $z < 0$ describes the position inside the liquid phase of the TPC. Let further be M the total amount of PMTs in the TPC, where $M = M_{top} + M_{bot}$ is the sum of the number of top and bottom PMTs. The S1 signal will be the measured (observed) amount of light produced by the prompt scintillation signal in units of photo electrons (pe). It is obtained by integrating the charge pulses of all contributing PMTs over the time domain. In the most common approach, the total signal (summed over all PMTs), $S1 = \sum_{i=1}^{M} S1_i$ is

spatially corrected

$$cS1 = S1 \frac{\langle \mu \rangle}{\mu(\mathbf{r})} \tag{5.1}$$

where

$$\langle \mu \rangle \equiv \frac{1}{V} \int \mu(\mathbf{r}) \, d\mathbf{r} \tag{5.2}$$

is the integral over the spatially dependent light collection efficiency (LCE) $\mu(\mathbf{r})$ inside the active volume V and

$$\mu(\mathbf{r}) \equiv \sum_{i=1}^{M_{\text{top}}+M_{\text{bot}}} \mu_i(\mathbf{r}). \tag{5.3}$$

The LCE $\mu_i(\mathbf{r})$ for PMT_i itself is the product of the probability $\gamma_i(\mathbf{r})$ that the photons created at position $\mathbf{r}$ will reach the photo cathode of PMT_i times the probability of creating one or two photo electrons and collecting them (where quantum and collection efficiencies of the various PMTs enter). For this work, the measured LCE map from the XENON100 detector [101] is used but could easily be replaced by a different one. The map is given in cylindrical coordinates and is normalized in the volume V of interest. This volume is called the fiducial volume and has the form of a super-ellipsoid inside the TPC. It is constructed by only considering the inner very silent part of the detector, where most of the radioactivity from the surrounding materials has already been screened by the surrounding xenon. The corrected signal is the value of S1 that would have been measured with an average detector light collection efficiency $\langle \mu \rangle$. In the case of a nuclear recoil event with energy deposit E, the probability for generating N_γ prompt scintillation photons at the interaction site can be written as

$$p(N_\gamma|E) = \text{Poi}_{N_\gamma}(\lambda = n_\gamma), \tag{5.4}$$

as shown in section 2.2.1. It is given by a Poisson distribution with expectation value $n_\gamma(\mathbf{r})$, which carries the spatial dependence. Following equation (2.10), $n_\gamma(\mathbf{r})$ can be expressed as

$$n_\gamma = \frac{E_{nr}}{W_\gamma(E_{nr})} \frac{W_\gamma(E_{ee})}{W_\gamma(E_{ee})} = E_{nr} \mathscr{L}_{\text{eff}} \frac{\mathscr{L}_y(\mathbf{r})}{\mu(\mathbf{r})} \frac{S_{nr}}{S_{ee}} \tag{5.5}$$

where the relations of (2.12) and (2.13) have been used. The quenching factors $S_{nr} = 0.95$ and $S_{ee} = 0.58$ are fixed according to [14]. After the NR the photons propagate through the detector where they are either detected by the PMTs in the top (after passing the liquid-gas interface) or the bottom PMTs. In case of reaching one of the PMT cathodes, the photons are absorbed and lead to the emission of photo electrons due to the photo-electrical effect. This conversion is modeled by a binomial distribution

$$p(N_{\text{pe}}|N_\gamma) = \text{Binom}_{N_{\text{pe}}}(p = \mu(\mathbf{r}), N = N_\gamma) \tag{5.6}$$

where the probability of success of converting N_γ photons into N_{pe} photo electrons is given by the light collection efficiency $\mu(\mathbf{r})$. See figure 5.1 for illustration of the light yield map.
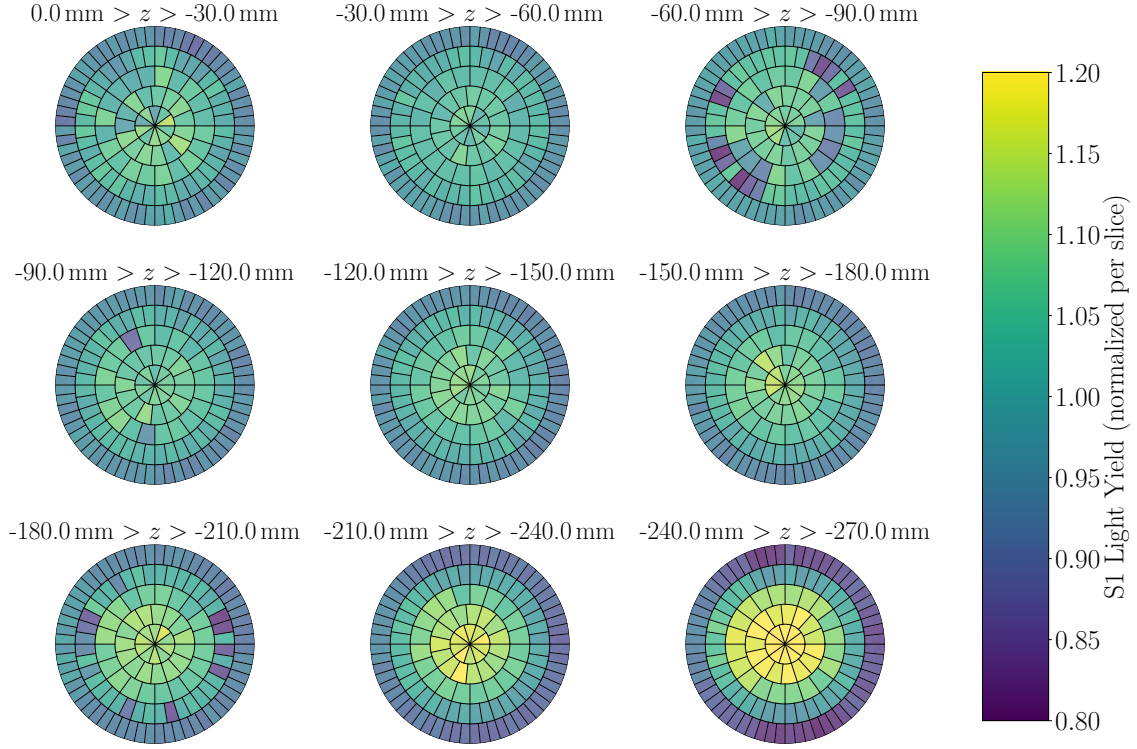
Figure 5.1.: S1 Light collection efficiency map (summed over all PMTs, top and bottom) for different slices in z, where $z = 0$ corresponds to the liquid-gas interface.

Therefore the likelihood function can be written as

$$\mathcal{L}_{S1}(E) \equiv p(S1|E) = \sum_{N_{\text{pe}}=1}^{\infty} \sum_{N_{\gamma}=0}^{\infty} p(S1, N_{\text{pe}}, N_{\gamma}|E)$$

$$= \sum_{N_{\text{pe}}=0}^{\infty} p(S1|N_{\text{pe}}) \sum_{N_{\gamma}=0}^{\infty} p(N_{\text{pe}}|N_{\gamma}) p(N_{\gamma}|E), \tag{5.7}$$

where $p(N_{\text{pe}}|N_{\gamma})$ is given by equation (5.6) and $p(N_{\gamma}|E)$ by equation (5.4). A component that still needs to be modeled is the average PMT response function $p(S1|N_{\text{pe}})$. This function is as already described in section 2.2.1 and is approximated by a normal distribution that can be written as

$$p(S1|N_{\text{pe}}) \approx \mathcal{N}_{S1}\left(\mu = N_{\text{pe}}, \sigma^2 = \sigma_{\text{PMT}}^2 N_{\text{pe}}\right), \tag{5.8}$$

where $\sigma_{\text{PMT}} = 0.5\,\text{pe}$ is the average PMT single photoelectron (SPE) response resolution (width). It is measured by fitting a Gaussian distribution for $p(S1|N_{\text{pe}} = 1)$, centered around $N_{pe} = 1\,\text{pe}$ and using standard error propagation for $N_{\text{pe}} > 1\,\text{pe}$. In the case of XENON100, this Gaussian is also truncated below $S1 < 0.35\,\text{pe}$ to account for PMT and

data acquisition threshold effects. Figure 5.2 shows an example SPE spectrum measured during an LED calibration of the XENON100.
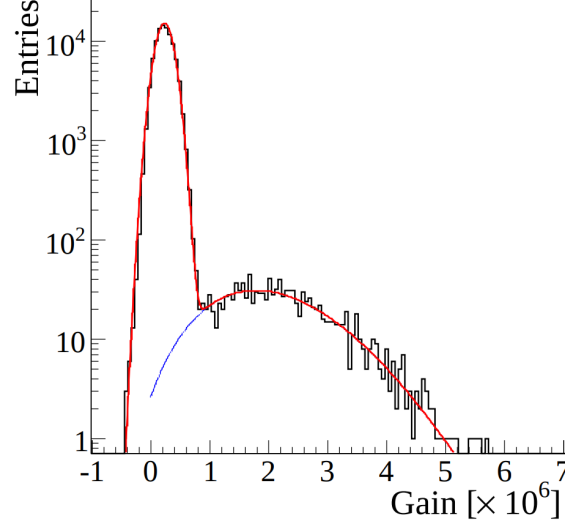
Figure 5.2.: Example of the XENON100 single photoelectron (SPE) LED calibration measurements for a single PMT. At a gain of 0 the noise peak is present followed by the SPE peak at a gain of around 2×10^6. From these fits e.g. the PMT response width σ_{PMT} or PMT gains are derived [101].

Using earlier mentioned relationships, see equation (2.13)ff., the second part of equation (5.7) can be rewritten to

$$\sum_{N_\gamma=0}^{\infty} p(N_{\text{pe}}|N_\gamma)p(N_\gamma|E) = \text{Poi}_{N_\gamma}(n_\gamma)\text{Binom}_{N_{\text{pe}}}(\mu(\mathbf{r}), N_\gamma) \tag{5.9}$$

$$= \text{Poi}_{N_{\text{pe}}}\left(\lambda = E\mathscr{L}_{\text{y}}(\mathbf{r})\mathscr{L}_{\text{eff}}\frac{S_{\text{nr}}}{S_{\text{ee}}}\right). \tag{5.10}$$

In this work the relative scintillation efficiency $\mathscr{L}_{\text{eff}}$ from [91] was chosen, see figure 5.4 for illustration. In this model, $\mathscr{L}_{\text{eff}}$ is set to 0 below 1 kev energy deposition to be conservative in the region with no data.

This leads to the already familiar form of the likelihood for the S1 signal:

$$\mathcal{L}_{S1}(E, \mathbf{r}) = \sum_{N_{\text{pe}}=1}^{\infty} p(S1|N_{\text{pe}})\text{Poi}_{N_{\text{pe}}}\left(\lambda = E\mathscr{L}_{\text{y}}(\mathbf{r})\mathscr{L}_{\text{eff}}\frac{S_{\text{nr}}}{S_{\text{ee}}}\right) \tag{5.11}$$

The spatial dependence of this function is encoded in $\mathscr{L}_{\text{y}}$ which is given by equation (2.12) and gets its dependency from the light collection efficiency $\mu(\mathbf{r})$ which depends on the interaction location in the detector. In the top left panel of figure 5.3, $\mathcal{L}_{S1}(E) = p(S1|E)$ is plotted as a sampling distribution, i.e. for fixed energies as a function of S1.
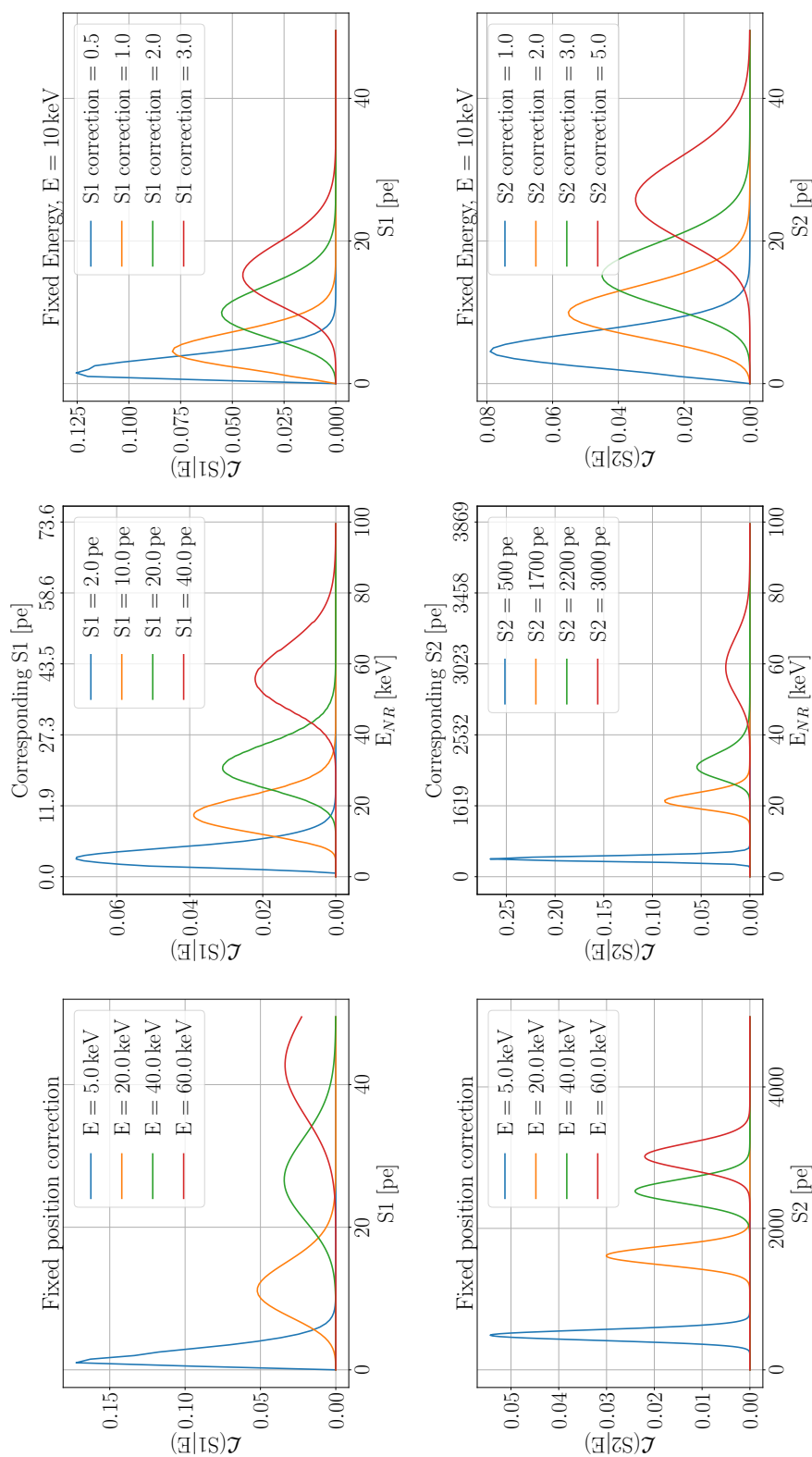
Figure 5.3.: Top: Illustration of $p(S1|E, \mathbf{r})$, plotted as a function of $S1$ for a fixed position (left panel) and different E; as a function of E for fixed a position and different $S1$ (middle panel) and as function of $S1$ for a fixed E and changing positions.
Bottom: The same plots but for $p(S2|E, \mathbf{r})$.
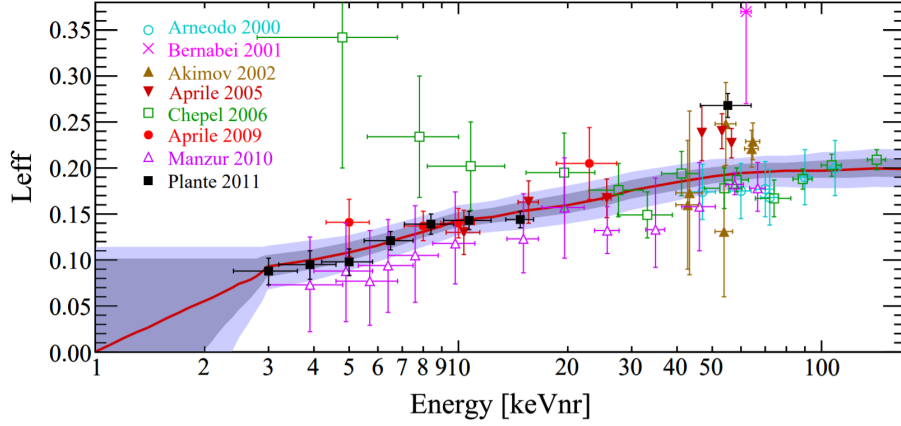
Figure 5.4.: Direct measurements of $\mathscr{L}_{\text{eff}}$ described by a Gaussian distribution to obtain the mean (solid line) and the uncertainty band ($1\,\sigma$ and $2\,\sigma$). Below $3\,\text{keV}_{nr}$ the trend is logarithmically extrapolated to $\mathscr{L}_{\text{eff}} = 0$ at $1\,\text{keV}_{nr}$ [91].

The same figure also shows the likelihood function itself, i.e. for fixed values of S1 as a function of the energy E (top right panel).

To put an emphasis on the spatial dependence, equation (5.11) is recast to

$$\mathcal{L}_{S1}(E, \mathbf{r}) = \sum_{N_{\text{pe}}=1}^{\infty} p(S1|N_{\text{pe}})\text{Poi}_{N_{\text{pe}}}\left(\lambda = E\tilde{\mu}(\mathbf{r})\langle\mathscr{L}_{\text{y}}\rangle\mathscr{L}_{\text{eff}}\frac{S_{\text{nr}}}{S_{\text{ee}}}\right), \qquad (5.12)$$

where the relative light collection efficiency (RLCE) $\tilde{\mu}(\mathbf{r})$ is introduced. It is defined as

$$\tilde{\mu}(\mathbf{r}) \equiv \frac{\mu(\mathbf{r})}{\langle\mu\rangle}. \qquad (5.13)$$

The average light yield $\langle\mathscr{L}_{\text{y}}\rangle = 2.28\,\text{pe/keV}$ at $122\,\text{keV}_{ee}$ has been interpolated from a dedicated measurement of several energy lines (e.g. $40\,\text{keV}$, $60\,\text{keV}$, $164\,\text{keV}$ and $662\,\text{keV}$, see [101] for reference).

For the later use in the modeled efficiency functions, which are (mostly) only available in the corrected space for the implemented example of the XENON100 detector, the information of the corrected $cS1$ values can always be obtained by using the position information of the event and converting the uncorrected signal back using the relation

$$S1 = \tilde{\mu}(\mathbf{r}) \cdot cS1. \qquad (5.14)$$

The standard analysis uses a detector averaged value of the light collection efficiency, leading to the spatial independent average light yield

$$\langle\mathscr{L}_{\text{y}}\rangle = \langle\mu\rangle\frac{S_{ee}}{W_{\gamma}}. \qquad (5.15)$$

Also, the likelihood of the standard analysis can easily be recovered by replacing $\mathscr{L}_y(\mathbf{r})$ with $\langle \mathscr{L}_y \rangle$ and $S1$ with $cS1$, which yields the familiar expression

$$\mathcal{L}_{cS1}(E) = \sum_{N_\gamma} p(N_{\mathrm{pe}}|N_\gamma)p(N_\gamma|E) = \mathrm{Poi}_{N_{\mathrm{pe}}}\left(\lambda = E\langle \mathscr{L}_y \rangle \mathscr{L}_{\mathrm{eff}}\frac{S_{\mathrm{nr}}}{S_{\mathrm{ee}}}\right). \tag{5.16}$$

This form of the likelihood can be identified with equation (2.19) after recasting some expressions.

5.2. Spatially Dependent Likelihood for the S2 Signal

While the description of the spatially dependent S1 likelihood is based on the description of section 2.2.1, the S2 likelihood will take a different more advanced approach. The nuclear recoil at position $\mathbf{r}$ also generates N_e electrons in addition to the prompt scintillation photons at the interaction site. This process, like the S1 photons, follows a Poisson distribution

$$P(N_e|E) = \mathrm{Poi}_{N_e}\left(\lambda = \frac{E}{W_e}T(\mathcal{E})\right), \tag{5.17}$$

where the symbols are already defined in equation (2.7). While the electrons are drifting upwards towards the gate, some of the electrons get lost by attaching to electronegative impurities. This process shows a characteristic exponential absorption behavior in time and is described by the electron lifetime τ_e. It is the time an electron can drift be fore it gets "absorbed" by an impurity. The electron life time usually grows during the run time of the detector, since the xenon inside the detector system is further purified. For an example of the time evolution in the XENON100 detector see [91]. The amount of electrons that make it to the liquid-gas interface is denoted as N_g which follows a binomial distribution of drawing N_e times with a success rate of $\exp(-t_d/\tau_e)$ times the spatial dependent detection probability $\delta(x,y)$, where t_d is the electron drift time. The detection probability itself is a product of the extraction yield, scintillation gain and a PMT and extraction location dependent efficiency, see section 2.2.2.

Since large $S2$ signals tend to saturate the top PMTs it is a common approach to only use the signal of the bottom PMT array to determine the amount of produced electrons. Though information of the S2 top signal is still used for e.g. position reconstruction by using the hit pattern and specialized algorithms.

To emphasize this fact, the S2 signal will be denoted as $S2_b$ whenever only the bottom information is used. The light yield map for the S2 signal will also only be given for the bottom PMT array in this work. the correction is denoted as $\delta(x,y)$ and is given by

$$\delta(x,y) = \sum_{i=1}^{M_b} \delta_i(x,y) \tag{5.18}$$

for for the XENON100 detector, which is shown in figure 5.5.
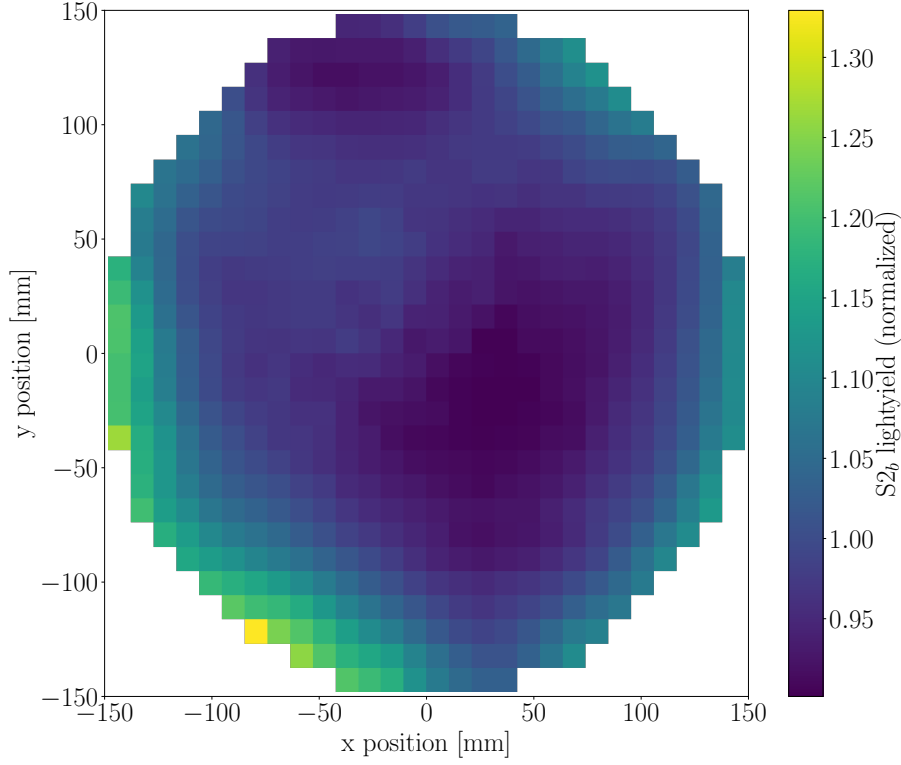
Figure 5.5.: Light collection efficiency map for the bottom PMT array of the XENON100 detector. This map has to be applied to the $S2_b$ signal as a correction factor.

In the next step the single electron response function, shown in figure 5.6, is used to convert the number of electrons N_g into the $S2_b$ signal in units of photo electrons (pe) using

$$p_{\text{se}}(S2_b|N_g) = \mathcal{N}_{S2_b}(\mu = \mu_b N_g, \sigma^2 = \sigma_b^2 N_g),\tag{5.19}$$

where $\mu_b = 6.98\,\text{pe}$ and $\sigma_b = 4.88\,\text{pe}$ are the amplification and width of the Gaussian PMT response for the bottom array of PMTs.

After invoking relation (2.16) and accounting for the marginalization over all intervening binomials where

$$\text{Binom}_k(n, p) \equiv \text{B}(K|n, p) = \binom{n}{k} p^k (1-p)^{n-k},\tag{5.20}$$

$p(N_g|E, \mathbf{r})$ is given as

$$p(N_g|E, \mathbf{r}) = \sum_{N_e} \text{Poi}_{N_e}(\lambda = E\mathcal{Q}_y)\text{Binom}_{N_g}(N_e, \exp(-t_d/\tau_e)\delta(x, y))\tag{5.21}$$

$$= \text{Poi}_{N_g}\left(\lambda = E\mathcal{Q}_y \cdot \exp(-t_d/\tau_e) \cdot \delta(x, y)\right)\tag{5.22}$$
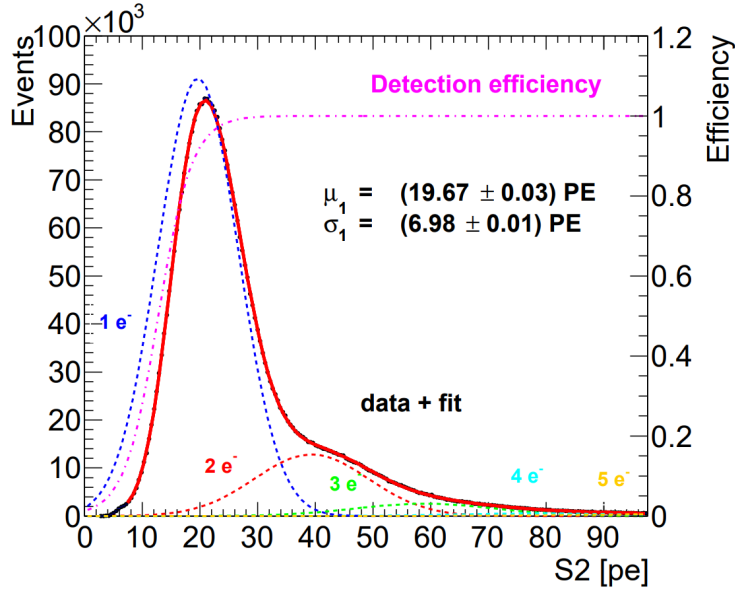
Figure 5.6.: Measurement of single electron response (blue dashed line). This measurement provides $p_{\text{se}}(S2|N_g)$ after normalization and $p_{\text{se}}(S2_b|N_g)$ after using the bottom only measurement [11].

where $\mathcal{Q}_y$ is the charge yield in $e^-/\text{keV}_{\text{nr}}$ which is measured separately, see e.g. [66] for reference. Given equations (5.19) and (5.21) the spatially dependent $S2_b$ likelihood follows as

$$\mathcal{L}_{S2_b}(E, \mathbf{r}) = p(S2_b|E, \mathbf{r}) = \sum_{N_g} p_{\text{se}}(S2_b|N_g) p(N_g|E). \tag{5.23}$$

The signal that would have been observed by a detector with spatially averaged detection efficiency $\langle \delta \rangle$, is therefore given by

$$cS2_b \equiv S2 \exp(t_d/\tau_e) \frac{\langle \delta \rangle}{\delta(x, y)}, \tag{5.24}$$

where

$$\langle \delta \rangle \equiv \frac{1}{A} \int \delta(x, y) \, \mathrm{d}x \, \mathrm{d}y \tag{5.25}$$

is the average detection efficiency inside the extraction area A.

5.3. Bayesian Implementation of the Signal Efficiency

Detectors are never 100 % efficient in any way. In a model, describing such a detector, these efficiencies have to be accounted for. In this work, for the data space of a xenon dual phase TPC, the two main factors that will be studied are the accumulated detection efficiencies of the S1 and S2 signals. Usually they are described by a function $\varepsilon(X)$,

where $X = \{S1, S2\}$. The signal efficiencies incorporate all data selection effects on the signals, whereas other efficiencies, e.g. absorption losses or quantum efficiencies are included in the instrumental response model. In the example case of XENON100, these efficiencies are given in the corrected data space $cS1$ and $cS2$. Later, a radial dependence was added to the S1 signal efficiency in the XENON1T analysis. Though, for the studies in this work, we want to implement a fully spatial dependence and it has been decided to use two dummy efficiencies of the XENON100 experiment that were still completely independent of spatial information: The unchanged $cS1$ efficiency $\varepsilon(cS1)$ of the 225-live days publication [101] and an artificial $cS2_b$ efficiency, which is motivated from the total $cS2$ efficiency. The hard threshold of 150 pe of $\varepsilon(cS2)$ has been translated to a lower, but still hard threshold of $\varepsilon(cS2_b)$. The cutoff was chosen to be 150 pe times the asymmetry factor (the fraction of light seen by the top or bottom PMT array is not symmetric), which results in $\varepsilon(cS2_b)_{\text{thres}} = 64.5$ pe. Otherwise the functional dependency was kept.

Figures 5.7 and 5.8 show the efficiencies as they were used in the analysis of this study. To be able to evaluate these functions, the uncorrected values of the signals have to be mapped back to the data space of the corrected signals using the individual position of each simulated event.

Before describing the actual incorporation into the signal model, the formalism and terminology will be introduced. The formalism will follow a general Bayesian way to describe the case of missing data due to a less than 100 % efficient data collection procedure, specifically considering data selection and event reconstruction efficiencies. We consider a case of missing data, where at the same time we have knowledge about the fact that not all data has been observed or that the data is knowingly somehow truncated.
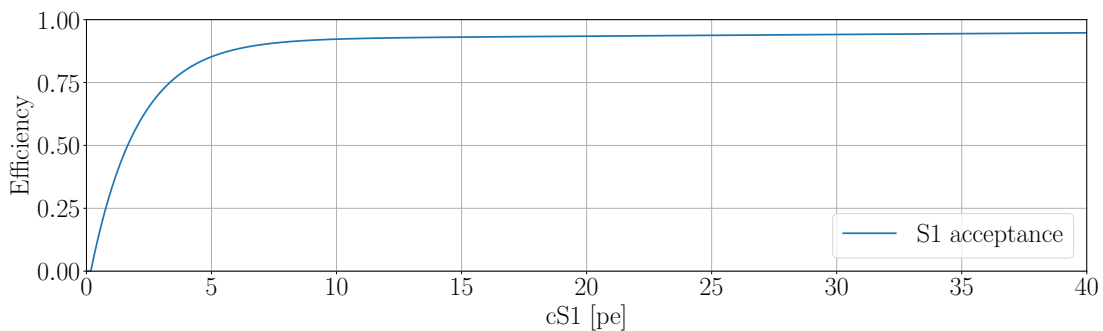
Figure 5.7.: Plot of the efficiency $\mathcal{E}_{S1}(cS1)$. The function has been adopted from earlier XENON100 analyses.

A collection of data $y = (y_1, y_2, \dots, y_N)$ includes all potential observations, the ones actually observed and also the ones that have been missed. Each y_i is a vector of all possible observables that an event produces (e.g. position, time, S1, S2b etc.). An indicator variable $I = (I_1, \dots, I_N)$ is introduced, which indicates if an event has been observed,
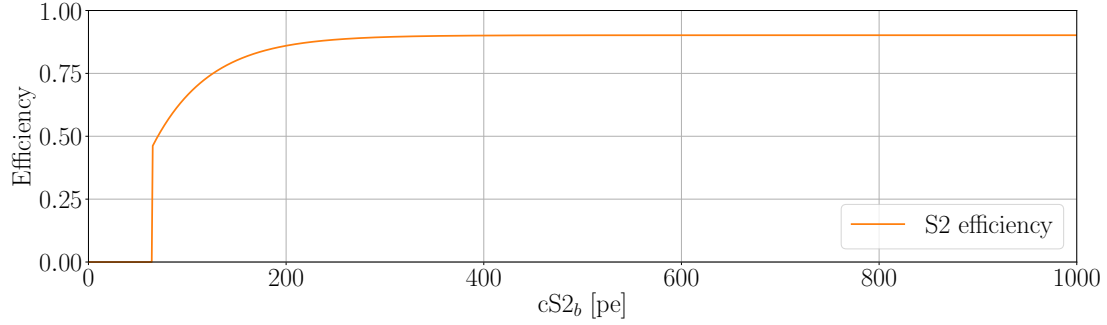
Figure 5.8.: Plot of the efficiency $\mathcal{E}_{S2_b}(cS2_b)$. Compared to its original used in XENON100, it has been modified to represent an $S2_b$ only efficiency (the functional correlation has been kept, but the hard threshold has been shifted to lower values following the asymmetry of light that is collected in the top and bottom PMT array).

$I_i = 1$, or has been missed, $I_i = 0$. This leads to the extended expression

$$y_{\text{obs}} = \{y_i | I_i = 1, i \in [1, \dots, N]\} \text{ and} \tag{5.26}$$

$$y_{\text{mis}} = \{y_i | I_i = 0, i \in [1, \dots, N]\}, \tag{5.27}$$

where the observed data is denoted by y_{obs} and the missed data by y_{mis}. The data likelihood therefore also has to be extended to

$$p(y, I | \Theta, \mathbf{r}, \phi) = p(y | \Theta, \mathbf{r}) \, p(I | y, \phi). \tag{5.28}$$

Here Θ are the parameters of the model that are not connected to the data collection procedure, like WIMP mass m_χ or cross-section σ_χ, whereas ϕ are the parameters that enter the data selection directly, i.e. they influence the shape of the efficiency function, e.g. detector related parameters like the light collection efficiency (LCE) $\mu(\mathbf{r})$. Therefore $p(y | \Theta)$ is the usual likelihood without selection effects and thus $y = y_{\text{obs}}$ in this case.

Merging the observed and unobserved events $y = \{y_{\text{obs}}, y_{\text{mis}}\}$, the likelihood for the observed data can be written as

$$p(y_{\text{obs}}, I | \Theta, \mathbf{r}, \phi) = \int dy_{\text{mis}} \, p(y, I | \Theta, \mathbf{r}, \phi), \tag{5.29}$$

where equality follows by the marginalization over the missing data in the complete likelihood. By marginalizing also over ϕ, the posterior distribution for the parameters of interest Θ, including selection effects follows as

$$p(\Theta | y_{\text{obs}}, \mathbf{r}, I) \propto \int d\phi \, p(\Theta, \phi) \int dy_{\text{mis}} \, p(y | \Theta, \mathbf{r}) p(I | y, \phi). \tag{5.30}$$

For comparison, assuming no (or ignoring) data collection efficiencies, the likelihood evaluated only for the observed data $p(y_{\text{obs}}|\Theta)$ yields the posterior distribution in the form

$$p(\Theta|y_{\text{obs}}) \propto p(\Theta)\, p(y_{\text{obs}}|\Theta). \tag{5.31}$$

The data collection effects can be neglected if $p(\Theta|y_{\text{obs}}, \mathbf{r}, I) = p(\Theta|y_{\text{obs}}, \mathbf{r})$. There are two conditions that would meet this situation:

1. Randomly missing data:
   i.e. $p(I|y, \phi) = p(I|y_{\text{obs}}, \mathbf{r}, \phi)$, which indicates that missing data only depends on the observed values y_{obs}.

2. Distinct parameters:
   i.e. $p(\phi|\Theta) = p(\phi)$, the data selection does not depend on the parameters of interest.

For the case of direct dark matter search, at least the second case is not satisfied. The WIMP spectrum changes the probability of missing data depending on the mass m_χ. Thus the data selection effects are not negligible.

Sticking to the above introduced formalism the following calculations apply for $S1$ and $S2_{\text{b}}$ equally and so a more general notation is chosen. As already mentioned, the data vector $y_{\text{obs}} = (y_1, y_2, \ldots, y_n)$, where n is the number of observed events and each y_i is a vector of the form $y_i = \{S1_i, S2_{\text{b}i}\}$. This already assumes that an event consists of both signals which also implies that the amount of $S1$s and $S2_{\text{b}}$s will be the same. The detector is triggered by the considerably larger $S2$ while its corresponding $S1$, which is much smaller and would cause a trigger only a fraction of the time (see e.g. the study in chapter 4), will be identified during the data processing pipeline. The actual unknown number of events, including the unobserved ones, is denoted by N_{Pois} and it is obvious that $N_{\text{Pois}} \geq n$. Further, the WIMP parameters of interest are denoted by $\Theta = \{m_\chi, \sigma_\chi^{\text{SI}}\}$.

Following equation (5.30), the joint posterior probability for the parameters of interest and N_{Pois} events is given by

$$p(\Theta, N_{\text{Pois}}|y_{\text{obs}}, \mathbf{r}, I) \propto p(y_{\text{obs}}, I|\Theta, \mathbf{r}, N_{\text{Pois}})p(\Theta, N_{\text{Pois}}), \tag{5.32}$$

where I is the above introduced indicator variable. Furthermore

$$p(\Theta, N_{\text{Pois}}) = p(N_{\text{Pois}}|\Theta, \mathbf{r})p(\Theta) = \text{Poisson}_{N_{\text{Pois}}}(\lambda(\Theta))p(\Theta) \tag{5.33}$$

where

$$\lambda(\Theta) = T_{\text{live}}M_{\text{fid}} \int_0^\infty dR/dE(\Theta)dE \tag{5.34}$$

is the expected amount of WIMP interactions in the detector for a given set of parameters Θ and detector parameters i.e. fiducial mass $M_{\text{fid}} = \rho_{\text{LXe}} \cdot V_{\text{fid}}$ and exposure time T_{live}. This is the number, the DM model predicts without any selection effects, noise or other detector specific influences. It is calculated by simply integrating the differential recoil energy spectrum, see e.g. figure 1.12 in the introduction section, over all possible energies. This clarifies the interpretation of N_{Pois}: It is the actual number of realized interactions

(observed and unobserved), subject to Poisson fluctuation around the expectation value $\lambda(\Theta)$, i.e. the number of events an ideal detector would have recorded.

In the next step the attention will be focused on the observed data likelihood:

$$p(y_{\text{obs}}, I|\Theta, \mathbf{r}, N_{\text{Pois}}) = \int dy_{\text{mis}} p(y, I|\Theta, \mathbf{r}, N_{\text{Pois}}) \tag{5.35}$$

$$= \int dy_{\text{mis}} p(y|\Theta, \mathbf{r}) p(I|y, N_{\text{Pois}}) \tag{5.36}$$

$$= \int dy_{\text{mis}} p(y_{\text{mis}}, y_{\text{obs}}|\Theta, \mathbf{r}) p(I|y, N_{\text{Pois}}) \tag{5.37}$$

$$= \int dy_{\text{mis}} p(y_{\text{mis}}|\Theta) p(y_{\text{obs}}|\Theta, \mathbf{r}) p(I|y, N_{\text{Pois}}). \tag{5.38}$$

Now $p(I|y, N_{\text{Pois}})$ is identified with the detector efficiencies, which is the part responsible for missing some of the events:

$$p(I|y, N_{\text{Pois}}) = \prod_{i=1}^{N_{\text{Pois}}} p(I_i|y_i, 1) = \prod_{i=1}^{n} \mathcal{E}(y_{\text{obs},i}) \cdot \prod_{i=1}^{N_{\text{Pois}}-n} (1 - \mathcal{E}(y_{\text{mis},i})), \tag{5.39}$$

where

$$p(I_i|y_i, 1) = \begin{cases} \mathcal{E}(y_{\text{obs},i}) & \text{for } I_i = 1 \\ 1 - \mathcal{E}(y_{\text{mis},i}) & \text{for } I_i = 0. \end{cases} \tag{5.40}$$

Here $I_i = 1$ indicates $y_i = y_{\text{obs},i}$ with a probability $\mathcal{E}(y_{\text{obs},i})$ and $I_i = 0$ the second case $y_i = y_{\text{mis},i}$ with a probability of $1 - \mathcal{E}(y_{\text{mis},i})$. For the efficiency the condition $1 = \mathcal{E}(y_i) = \mathcal{E}(y_{\text{obs},i}) + (1 - \mathcal{E}(y_{\text{mis},i}))$ was used. In words, this reads as follows: It is known, that there are N_{Pois} events but not all of them are observed by the detector, i.e. each of the N_{Pois} events is either observed or missed.

Inserting equation (5.39) into (5.38) and also considering all possible combinations of n events being observed out of N_{Pois} possible events (which is expressed by an additional factor $\binom{N_{\text{Pois}}}{k}$ to account for all possible permutations of the events being observed or missed) in addition to the fact that $\int d\, y_i p(y_i|\Theta) = 1$, the likelihood can be separated into two parts:

$$p(y_{\text{obs}}, I|\Theta, \mathbf{r}, N_{\text{Pois}}) = \left[\prod_{i=1}^{n} p(y_{\text{obs},i}|\Theta, \mathbf{r}) \mathcal{E}(y_{\text{obs},i}) \right]$$

$$\times \binom{N_{\text{Pois}}}{n} \left[\prod_{i=1}^{N_{\text{Pois}}-n} \int dy_{\text{mis},i}\, p(y_{\text{mis},i}|\Theta)(1 - \mathcal{E}(y_{\text{mis},i})) \right] \tag{5.41}$$

$$= \binom{N_{\text{Pois}}}{n} \prod_{i=1}^{n} \mathcal{L}_{y_{\text{obs},i}, \mathbf{r}}(\Theta) \mathcal{E}(y_{\text{obs},i}) \left[1 - f(\Theta)\right]^{N_{\text{Pois}}-n}, \tag{5.42}$$

where the average of the efficiency over the likelihood has been defined as

$$f(\Theta) = \int dx \mathcal{L}_x(\Theta) \mathcal{E}(x). \tag{5.43}$$

Depending on the case, $y_{\text{obs,i}}$ can either be dependent on $S1$, $S2_b$ or both $\{S1, S2_b\}$ and thus

$$\mathcal{L}_{y_{\text{obs,i}}}(\Theta, \mathbf{r}) = \begin{cases} \mathcal{L}_{S1_i}(\Theta, \mathbf{r}) & \text{for } y_{\text{obs,i}} = S1_i \\ \mathcal{L}_{S2_{b,i}}(\Theta, \mathbf{r}) & \text{for } y_{\text{obs,i}} = S2_{b,i} \\ \mathcal{L}_{S_{\text{tot},i}}(\Theta, \mathbf{r}) & \text{for } y_{\text{obs,i}} = \{S1_i, S2_{b,i}\} \,. \end{cases} \tag{5.44}$$

The likelihood and efficiency can be separated into the product

$$\mathcal{L}_{y_{\text{obs,i}}}(\Theta, \mathbf{r})\mathcal{E}(y_{\text{obs,i}}) = \mathcal{E}(S_{\text{tot},i})p(S_{\text{tot},i}|\Theta, \mathbf{r}) \,, \tag{5.45}$$

whose terms can be factorized into

$$\mathcal{E}(S_{\text{tot},i})p(S_{\text{tot},i}|\Theta, \mathbf{r}) = \mathcal{E}_{S1}(cS1_i)\mathcal{E}_{S2_b}(cS2_{b,i})\int_0^\infty p(S_{\text{tot},i}|E, \mathbf{r})p(E|\Theta)\,\mathrm{d}E \tag{5.46}$$

$$= \mathcal{E}_{S1}(cS1_i)\mathcal{E}_{S2_b}(cS2_{b,i})\int_0^\infty p(S1_i|E, \mathbf{r})p(S2_{b,i}|E, \mathbf{r})p(E|\Theta)\,\mathrm{d}E \,. \tag{5.47}$$

For the missed events $y_{\text{mis,i}}$, there is no information on the spatial location and so the averaged, corrected form of the likelihood has to be calculated instead

$$f(\Theta) = f(m_\chi) = \int \mathrm{d}cS_{\text{tot}}\, \mathcal{E}(cS_{\text{tot}})p(cS_{\text{tot}}|\Theta) \,, \tag{5.48}$$

where $\mathcal{E}(cS_{\text{tot}})$ is calculated following the same recipe as before and

$$p(cS_{\text{tot}}|\Theta) = \int_0^\infty p(cS1|E)p(cS2|E)p(E|\Theta)\mathrm{d}E \,. \tag{5.49}$$

$f(m_\chi)$ is always calculated using both, $S1$ and $S2_b$ signals, since only events that survive both selection processes will contribute to the finally observed data. Single $S1$s or $S2_b$s will be discarded, an effect already incorporated in the efficiencies. For the case of observed data, one can decide to only use one of both signals for later inference, but the other part of the signal would still be available. Figure 5.9 illustrates an example how $f(m_\chi)$ is constructed for $m_\chi = 50\,\text{GeV}$.

For the likelihood of the observed data, see equation (5.42), the first part can be identified with the likelihood for a negligible data collection effect, i.e. $\prod_{i=1}^n \mathcal{L}_{y_{\text{obs,i}}}\mathcal{E}(y_{\text{obs,i}})$ times a WIMP-mass dependent correction factor that is given by

$$C(m_\chi) = \binom{N_{\text{Pois}}}{n}[1 - f(m_\chi)]^{N_{\text{Pois}}-n} \,. \tag{5.50}$$

To obtain the marginal posterior for the parameters of interest, equation (5.32) has to be marginalized over N_{Pois}:

$$p(\Theta|y_{\text{obs}}, \mathbf{r}, I) = \sum_{N_{\text{Pois}}=n}^\infty p(\Theta, N_{\text{Pois}}|y_{\text{obs}}, \mathbf{r}, I) \tag{5.51}$$
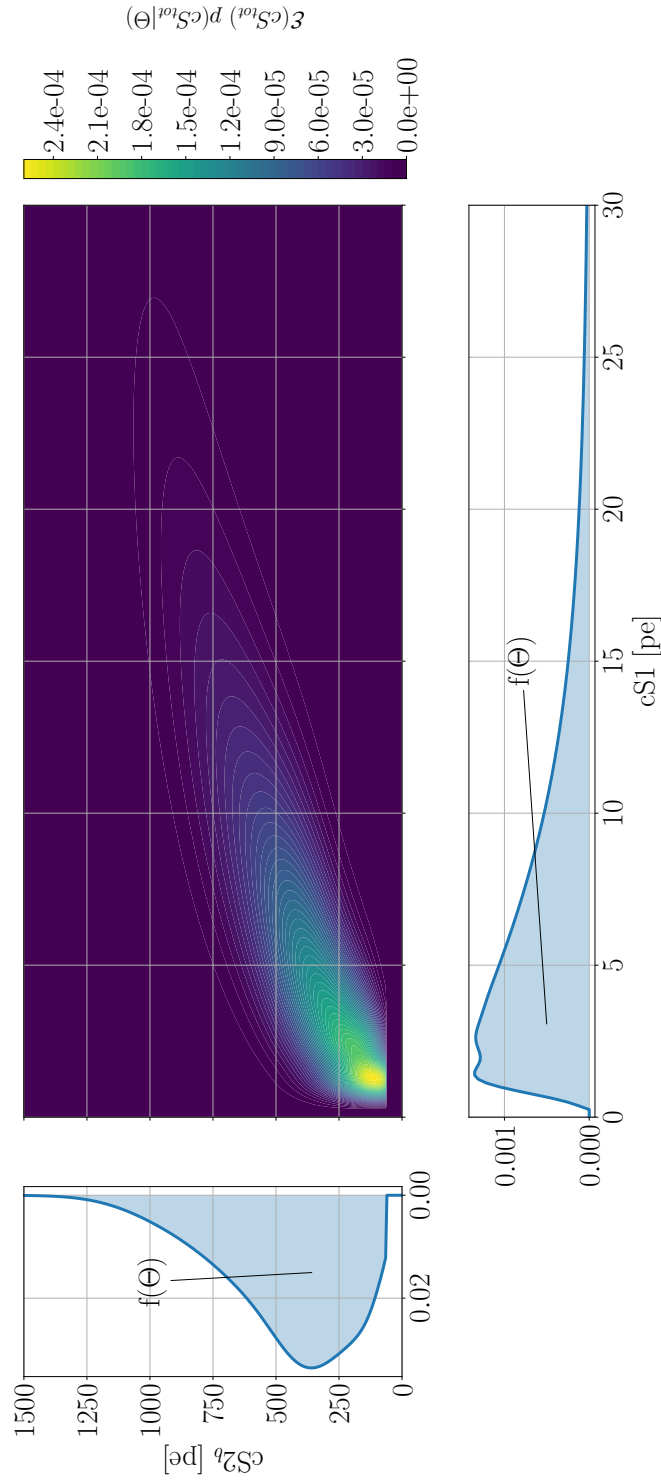
Figure 5.9.: Example of the calculation and construction of $f(m_\chi)$, see equation (5.48). The center plot shows the results of equation (5.46), using the corrected signals only. The left (bottom) graph, show the marginalized distribution over cS1 (cS2$_b$). For both distributions, the integrals (light blue areas) yield the correction factor of interest $f(m_\chi)$, for a given WIMP mass of $m_\chi = 50\,$GeV.

$$= \sum_{N_{\text{Pois}}=n}^{\infty} p(N_{\text{Pois}}|\Theta, \mathbf{r}) C(m_\chi) \prod_{i=1}^{n} \mathcal{L}_{y_{\text{obs,i}}}(\Theta, \mathbf{r}) \mathcal{E}(y_{\text{obs,i}}) p(\Theta) \tag{5.52}$$

$$= \prod_{i=1}^{n} \mathcal{L}_{y_{\text{obs,i}}}(\Theta, \mathbf{r}) \mathcal{E}(y_{\text{obs,i}}) p(\Theta)$$

$$\times \sum_{N_{\text{Pois}}=n}^{\infty} \frac{\lambda^{N_{\text{Pois}}} e^{-\lambda}}{N_{\text{Pois}}!} \frac{N_{\text{Pois}}!}{(N_{\text{Pois}} - n)!n!} (1 - f(m_\chi))^{N_{\text{Pois}}-n} . \tag{5.53}$$

This expression can be further reduced by rewriting the second part of the equation:

$$\sum_{N_{\text{Pois}}=n}^{\infty} \frac{\lambda(\Theta)^{N_{\text{Pois}}} e^{-\lambda(\Theta)}}{N_{\text{Pois}}!} \frac{N_{\text{Pois}}!}{(N_{\text{Pois}} - n)!n!} (1 - f(\Theta))^{N_{\text{Pois}}-n} \tag{5.54}$$

$$= \sum_{N_{\text{Pois}}=n-n}^{\infty-n} \frac{\lambda(\Theta)^{N_{\text{Pois}}+n} e^{-\lambda(\Theta)}}{(N_{\text{Pois}} - n + n)!n!} (1 - f(\Theta))^{N_{\text{Pois}}-n+n} \tag{5.55}$$

$$= \sum_{N_{\text{Pois}}=0}^{\infty} \frac{\lambda(\Theta)^{N_{\text{Pois}}} \lambda(\Theta)^n e^{-\lambda(\Theta)}}{(N_{\text{Pois}})!n!} (1 - f(\Theta)^{N_{\text{Pois}}} \tag{5.56}$$

$$= \frac{\lambda(\Theta)^n e^{-\lambda(\Theta)}}{n!} \underbrace{\sum_{N_{\text{Pois}}=0}^{\infty} \frac{(\lambda(\Theta)(1 - f(\Theta)))^{N_{\text{Pois}}}}{N_{\text{Pois}}!}}_{=\exp(\lambda(\Theta)-\lambda(\Theta)f(\Theta))} \tag{5.57}$$

$$= \frac{\lambda(\Theta)^n e^{-\lambda(\Theta)}}{n!} e^{\lambda(\Theta)-\lambda(\Theta)f(\Theta)} \tag{5.58}$$

$$= \frac{\lambda(\Theta)^n}{n!} e^{-\lambda(\Theta)f(\Theta)} , \tag{5.59}$$

which leads to the simplified expression

$$p(\Theta|y_{\text{obs}}, \mathbf{r}, I) = \frac{\lambda(\Theta)^n}{n!} e^{-\lambda(\Theta)f(\Theta)} \prod_{i=1}^{n} \mathcal{L}_{y_{\text{obs,i}}}(\Theta, \mathbf{r}) \mathcal{E}(y_{\text{obs,i}}) p(\Theta) . \tag{5.60}$$

This is almost the same result as (incorrectly) assuming no selection effects and introducing a simple Poisson term for the number of observed events. The integration over the missing data instead leads to a different exponent in the Poisson distribution like part, i.e. $-\lambda(\Theta)f(\Theta)$ instead of $-\lambda(\Theta)$ only.

This is rather unexpected and a new finding from this approach of including the efficiencies. It also triggers some questions:

1. *How does the result behave for the case of no selections effects?*
   For $\mathcal{E} \to 1$ also $\lim_{\mathcal{E} \to 1} f(\Theta) = 1$ and therefore $n \to N_{\text{Pois}}$. The result is an unmodified Poisson distribution.

2. *What happens for small WIMP-masses m_χ?*
   In this case $f(\Theta)$ becomes smaller than 1. The likelihood will peak at smaller $S1$s and $S2_b$s, where also the efficiency is worse and the integral of $\mathcal{L}_{y_{\text{obs,i}}}(\Theta)$ gets also

smaller than 1. The fact that small masses lead to signals that are more difficult to observe is compensated by the modified Poisson term which gets up-weighted for $f(\Theta) < 1$ in the exponent.

3. *Is it compatible with the expectations for the extreme cases like $n = 0$ but $N_{Pois} > 0$ and in addition to the case where $N_{Pois} = 0$ and $n = 0$?*
   In the first case, some events are predicted but none are observed in the end, which yields $y_{\text{obs}} = \varnothing$ and $p(\Theta|y_{\text{obs}}, I) = \exp(-\lambda(\Theta)f(\Theta))p(\Theta)$. Here the posterior is suppressed with respect to the prior for regions of the parameter space where $\lambda(\Theta) \times f(\Theta)$ is large and therefore the exponential is small.
   In the second case, where no events have been expected and none have been observed the posterior is reduced to the prior $p(\Theta|\varnothing, I)p(\Theta) = p(\Theta)$ since $\lambda \to 0$. There has been no gain in information and the prior knowledge is returned, due to the lack of sensitivity in this part of the parameter space.

These results agree with the theoretical and intuitive expectations. In the next chapter, after explaining the event simulation, a further cross-check of this approach will be performed.

5.4. Hierarchical Model for the WIMP Parameters

Sticking with the previously introduced notation, denoting the signal as $S_{\text{tot}} = S1, S2_{\text{b}}$ and using n for the number of observed events, with $y_{\text{obs}} = S_{\text{tot}}$ the posterior for the parameters of interest $\Theta = m_\chi, \sigma_{\text{SI}}$ can be written as

$$p(\Theta|S_{\text{tot}}, \mathbf{r}, I) = \frac{\lambda^n}{n!} \exp(-\lambda f) \prod_{i=1}^{n} p(S_{\text{tot},i}|\Theta, \mathbf{r})\mathcal{E}(S_{\text{tot},i})p(\Theta). \tag{5.61}$$

Connecting this likelihood with the previously derived expressions for the $S1$ and $S2_{\text{b}}$ likelihoods yields

$$p(S_{\text{tot},i}|\Theta, \mathbf{r}) = \int_0^\infty p(S_{\text{tot},i}|E, \mathbf{r})p(E|\Theta)dE \tag{5.62}$$

$$= \int_0^\infty p(S1_i|E, \mathbf{r})p(S2_{\text{b}i}|E, \mathbf{r})p(E|\Theta)dE, \tag{5.63}$$

where $p(S1_i|E) = \mathcal{L}_{S1,i}(E)$ and $p(S2_{\text{b}i}|E) = \mathcal{L}_{S2_{\text{b}},i}(E)$. Here the factorization of the likelihoods is done by assuming that they are independent, see section 2.2 and figure 2.4. The model will be hierarchical in the sense that it marginalizes out the latent (unknown) energy information for each event while retaining the probabilistic dependency on the WIMP energy spectrum for fixed astrophysical parameters:

$$p(E|\Theta) = p(E|m_\chi) = \frac{dR(E)/dE}{\int_0^\infty (dR(E)/dE)dE}, \tag{5.64}$$

which is the normalized pdf for the latent and unobserved event energy E for a WIMP interaction (energy deposition) with parameters $\Theta = m_\chi, \sigma_{SI}$. The dependence on the cross-section σ_{SI} disappears due to the normalization while being only a multiplicative factor in the nominator as well as in the denominator. The spectrum itself can be written, in accordance with section 1.5.2, as

$$\frac{dR}{dE}(x) = \frac{\rho_0 \sigma_{SI} A^2 F^2(x)}{2\mu_p^2 m_\chi} \int_{v > v_{\min}(m_\chi)} d^3 v \frac{f(v + v_E)}{v}, \tag{5.65}$$

where ρ_D is the local Dark Matter density , A is the atomic number of the target material, $F(E)$ is the nuclear form-factor, μ_p is the reduced proton-target mass while $f(v, v_e)$ is the velocity distribution within the DM halo (which is also dependent on earth's velocity) and finally $v_{\min}$ is the minimum speed a DM particle of mass m_χ must have to produce an energy deposit of energy E.

As described in chapter 4, the main trigger is on $S2$ which is the larger of the two signals. When this trigger happens with an efficiency given by $\mathcal{E}_{S_2}(S2)$, a corresponding $S1$ signal is searched for in the data window right before the trigger with efficiency $\mathcal{E}_{S_1|S_2}(S1)$. Notice that this efficiency assumes that a corresponding $S2$ signal has already been triggered. Assuming this chain of causality, it can be understood as a missing data problem with a truncation i.e. it is known that for each $S1$ signal there is already a corresponding $S2$ signal whose value however is not recorded in $\mathcal{E}_{S_1|S_2}(S1)$. The total efficiency for passing both sets of data selection effects (cuts) on S2 and S1, given that S2 has been observed, is denoted by $\mathcal{E}(S_{tot})$, which can be be factorized in a product of the two efficiencies, as

$$\mathcal{E}(S_{tot}) = \mathcal{E}_{S_1|S_2}(cS1)\mathcal{E}_{S_2}(cS2). \tag{5.66}$$

Finally, the posterior for the WIMP parameters is given by the expression

$$p(\Theta|S_{tot}, \mathbf{r}) \propto \frac{\lambda^n}{n!} p(\Theta) \exp(-\lambda f) \prod_{i=1}^{n} \mathcal{E}(S_{tot,i}) \int \mathcal{L}_{S1_i}(E, \mathbf{r}) \mathcal{L}_{S2_i}(E, \mathbf{r}) p(E|\Theta) \, dE, \tag{5.67}$$

with suitably defined prior $p(\Theta)$ on m_χ and σ_{SI}. The terms $\mathcal{E}(S_{tot,i})$ depend only on the observed values of $S1$ and $S2$ and hence this part of the selection effect is negligible (i.e. it is only a multiplicative constant that does not depend on the parameters of interest).

Chapter 6

Simulation Study: Quantification of the generic Signal-Model

This chapter deals with the previously introduced approach from chapter 5. After an introduction on how events are simulated in section 6.1, the implementation of the efficiency is verified with a Monte Carlo study in section 6.2. In the main section 6.3, the Bayesian study of reconstructing the Dark Matter parameters: WIMP mass m_χ and cross-section σ_χ is performed. This study is repeated for different sets of input parameters and whole event sets. To conclude, an upper limit for a background free experiment is calculated in section 6.4.

6.1. Generating Events

At the time the presented approach was developed, the XENON100 detector was still up and running whereas the XENON1T detector was still at the stage of commissioning. So all detector parameters were adopted from the XENON100 experiment for the purpose of using well understood and established sets of parameters.

The detector specific and astrophysical parameters that are needed to simulate a single event can be found in table 6.1. The production of a single event, always consisting of the primary scintillation light signal ($S1$) and the secondary proportional scintillation signal ($S2_b$) follows this procedure:

1. Given a choice of parameters Θ, the expected number of Dark Matter events λ is calculated using equation (5.34), integrating over the whole energy range. No threshold or selection effects are applied yet. Figure 6.1 shows the number of expected events for the considered WIMP mass range at a fixed cross-section of arbitrary choice.

2. The amount of actually observed events N_{Pois} is determined by drawing from a Poisson distribution with expectation value λ.

3. For every observed event $j = 1, \ldots, N_{\text{Pois}}$:

a) From the (normalized) WIMP spectrum an energy E_j is drawn using a simple rejection sampling method.

b) A position (x_j, y_j, z_j) inside the fiducial volume is randomly initialized considering a uniform distribution of WIMP events in the volume.

c) For the given energy from step a) and the position from b), the signals $S1_j$, $S2_{bj}$ are sampled from their respective likelihoods independently, see equation 5.12 and 5.23, still without applying any thresholds or selection effects.

d) In the next step, it is checked if the event passes the selection (detector efficiency):

    i. Generate two independent random numbers from a uniform distribution between 0 and 1

    ii. Check if the $S1_j$ signal passes the selection by comparing the efficiency $\mathcal{E}_{S1}(cS1_j)$ and the first random number. The needed value of $cS1_j$ is calculated using the attached position (x_j, y_j, z_j) and equation 5.14, since the detection efficiency is only available in the corrected signal space.

    iii. Analogous check if the $S2_{bj}$ signal passes the selection by comparing the efficiency $\mathcal{E}_{S2_b}(cS2_{bj})$ and the second random number. The needed value of $cS2_{bj}$ is calculated using the attached position (x_j, y_j, z_j) and equation 5.24.

    iv. The event is only kept if ii. **and** iii. are passed. If one of these conditions is not met, the event is discarded since it would not have been processed as a full event in the first place during data processing.

4. After the selection procedure n observed events are left, where obviously $n \leq N_{\text{Pois}}$.

Table 6.1.: Selection of the most relevant Xenon100 model parameters

Parameter	Description	Value	Unit
FM	fiducial mass	34	kg
L_y	(S1) light yield	2.28	pe/keV$_{ee}$
T	detector live-time	224.56	d
S_{nr}	NR quenching factor	0.95	-
S_{ee}	ER quenching factor	0.58	-
v_d	e^- drift velocity	1.7	mm/μs
τ_e	e^- lifetime	514	μs

Figure 6.2 shows events for three monochromatic input energies as a test setup. Monochromatic energies have been chosen for better illustration, since for a given WIMP energy spectrum the different energies would not be distinguishable. For each energy, 200 events have been produced (transparent circles) and a selection by applying the detector efficiencies has been performed afterwards. The surviving events are marked as a dot within the
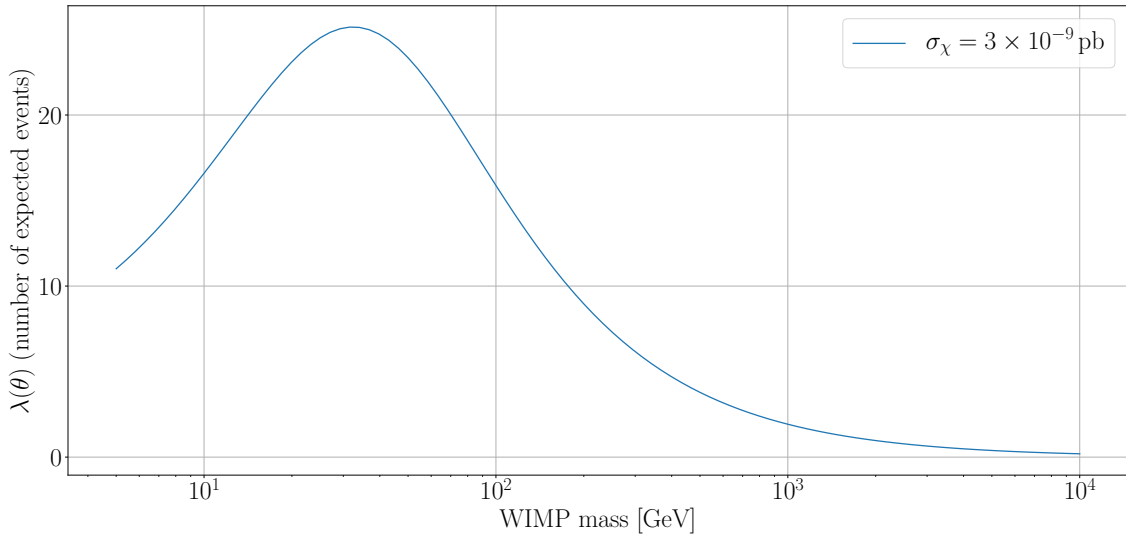
Figure 6.1.: The number of expected events for a fixed cross-section of $\sigma_\chi = 10^{-8}$ pb plotted against the WIMP mass (blue line) using the detector parameters from table 6.1.

circles. Each event has all relevant information stored as meta data, e.g. position, energy and correction factors will be stored and are ready for further analysis.
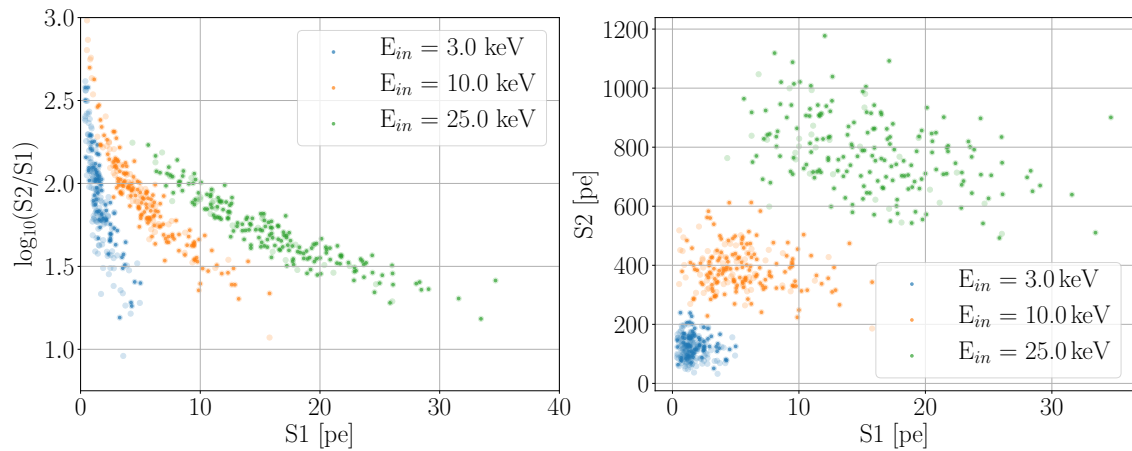
Figure 6.2.: Events for three monochromatic input energies: 3.0, 10.0 and 25.0 keV. For each energy 200 events have been generated (transparent circles) and a selection by applying the detector efficiencies has been performed afterwards. The surviving events are marked as a dot within the transparent circles. Each event contains all relevant information stored as meta data, e.g. position, energy and correction factors.

6.2. Verifying the Efficiency implementation

Since it is one of the major changes to the standard approach, a special emphasis will be put on the verification of the implementation of the detector efficiencies. The pipeline for this verification consist of 5 steps:

1. For a given WIMP mass of 50 GeV and an assumed WIMP-nucleon cross-section of 10^{-8} pb, events according to section 6.1 are produced assuming the exposure parameters from table 6.1.

2. For this test setup 1000 individual experiments are produced, i.e. 1000 datasets each with a fluctuating amount of events which is drawn from a Poisson distribution with an expectation value of $\lambda = 77.83$, see figure 6.1 and equation (5.34).

3. The corresponding correction factor for a WIMP mass of 50 GeV is obtained using equation 5.48, whose overall mass dependence is illustrated in figure 6.3.
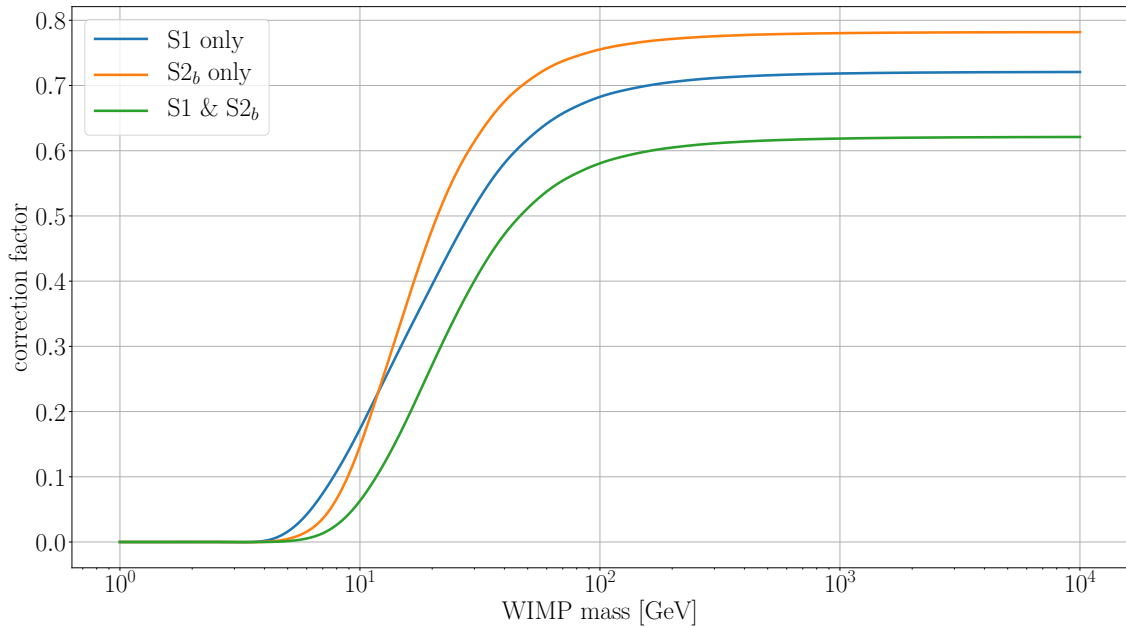
Figure 6.3.: The efficiency correction factor f(m_χ) only depends on the WIMP mass, see equation 5.48 for reference. Only when both signals are present in an event it is considered complete. This is expressed in the combined correction factor labeled $S1$ & $S2_b$ (green line). The individual correction factors for S1 only (blue) and $S2_b$ only (orange) are plotted in addition for completeness.

4. Assuming the simple scenario of a constant selection effect with $\mathcal{E} < 1$, equation (5.48) yields $f(m_\chi) = \mathcal{E}$, which leads to an average of

$$\langle N_{\text{Pois}} \rangle = \lambda \text{ and } \langle n \rangle = \mathcal{E}_{\text{const.}} \cdot \langle N_{\text{Pois}} \rangle = f(m_\chi = 50 \, \text{GeV}) \cdot \lambda. \tag{6.1}$$

events (i. e. neglecting Poisson fluctuations).

5. Using the correction factor and the previously generated events, this simplified scenario is tested for the more general case of signal dependent selection effects: Each of the 1000 experiments is corrected following the relation

$$\lambda_{\langle n \rangle_i} = \frac{n_i}{f(m_\chi = 50\,\text{GeV})},$$

(6.2)

which on average should yield an estimate for the true amount of expected events $\lambda \approx \langle \lambda_{\langle n \rangle_i} \rangle$ if the correction works as expected in up-weighting the amount of events that have been missed due to selection effects.

Figure 6.4 shows the histogram, filled with all $\lambda_{\langle n \rangle_i}$ calculated following equation (6.2). The mean value $\langle \lambda_{\langle n \rangle_i} \rangle = 79.9$ is very close to the real value and only differs 2.4 % from the true value of $\lambda = 77.8$, which is much smaller than the typical standard deviation
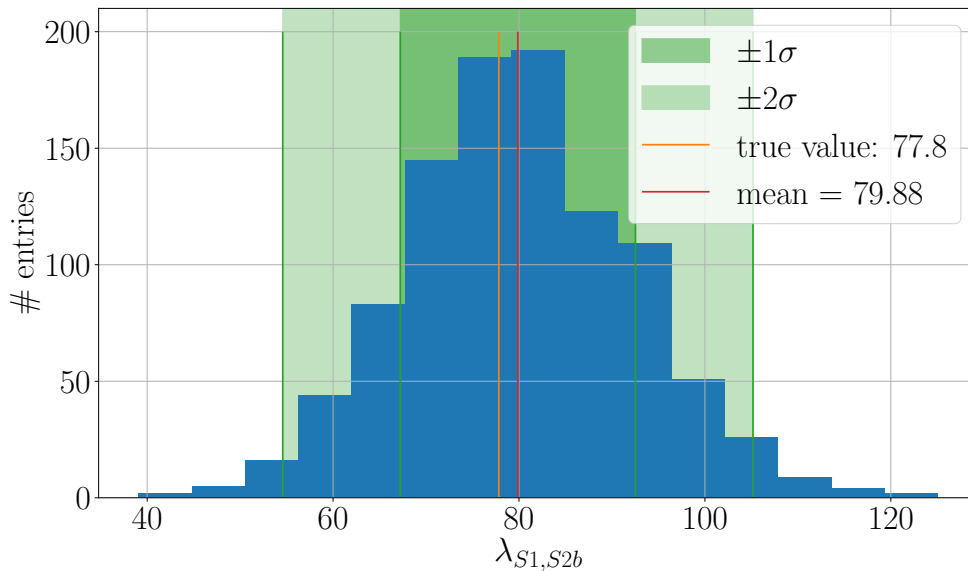
Figure 6.4.: Using the correction factor, the average number of observed events n can be corrected to match the initial number of expected events $\lambda = \langle n \rangle / f(m_\chi) = 77.8$. The blue histogram shows all corrected values $\lambda_{\langle n \rangle_i}$ of the initial n_i events of 1000 individual experiments. The true value (orange) is the expected number of events λ, which is equal to the average number of observed events $\langle N_{\text{Pois}} \rangle$, i.e. ignoring the Poisson fluctuations. As mean (red line) the average value of all corrected observed events $\langle \lambda_{\langle n \rangle_i} \rangle = 79.9$ is shown. This shows that using the correction factor, the true amount of events can be reconstructed with high accuracy.

of 8.82 events for a Poisson distributed value. As discussed in 5.3 for equation (5.48) the correction factor is calculated for the missed events, so no spatial information is available. This, by construction, introduces a systematic error but cannot be avoided.

Looking at these results, the implementation of the signal efficiencies has succeeded. The model introduced in section 5.3 is able to reproduce the initial amount of observed events N_{Pois} with high accuracy.

6.3. Dark Matter Parameter Reconstruction

This section shows the improved signal model in action. The performance of the ability to reconstruct the Dark Matter parameters of interest, i.e. WIMP mass m_χ and cross-section σ_χ, given the observed events after selection effects is evaluated.

For this purpose a new framework written in python has been developed. Using the numerous compiled libraries that the python community provides, even while being a high level language it can deliver a reasonable speed. Especially when using vector and matrix algebra which is provided by one of the widely used python library *numpy* (numerical python) [74]. Using these compiled libraries python can operate at a remarkable speed, not as fast as compiled languages as C++ but almost as fast.

The posterior probability density function of the dark matter parameters is obtained using MCMC sampling, which is a common tool used in Bayesian inference. See section 3.3.3 for information on the particular MCMC algorithm implemented in the EMCEE library [47], which is used in the framework presented here.

Since the likelihood functions, i.e. $\mathcal{L}_{S1}(E, \mathbf{r})$ and $\mathcal{L}_{S2}(E, \mathbf{r})$ are also written in python and not compiled they were calculated and stored beforehand. This was done by binning and normalizing the likelihoods in three dimensions: deposited Energy, detector signal S1(2) and a correction factor that incorporates the position dependence. The dependencies of the likelihood functions change to

$$\mathcal{L}_{S1}(E, \mathbf{r}) \rightarrow \mathcal{L}_{S1}(E, \mu(\mathbf{r})) \tag{6.3}$$

and

$$\mathcal{L}_{S2}(E, \mathbf{r}) \rightarrow \mathcal{L}_{S2}(E, \delta(\mathbf{r})). \tag{6.4}$$

Using a correction factor reduces the dimensionality needed by 2, which on the one hand saves a lot of computing time and on the other also a lot of disk-space. The granularity of the binning was chosen to still be able to calculate the integrals of the pdfs, even for small energies down to 1 keV which obviously gets harder the coarser the binning is chosen. The step-sizes and ranges chosen for the binning can be found in table 6.2.

Table 6.2.: Ranges and binning of the likelihoods $\mathcal{L}_{S1}(E, \mu(\mathbf{r}))$ and $\mathcal{L}_{S2}(E, \delta(\mathbf{r}))$.

	Energy	S1	$S2_{\text{b}}$	$\mu(\mathbf{r})$	$\delta(\mathbf{r})$
range	0-100 keV	0-100 pe	0-4000 pe	0.8-2.0	0.5-3.0
binning	0.125 keV	0.125 pe	5 pe	0.05	0.05

6.3.1. cS1-only Analysis as a Benchmark

Now that everything has been prepared, a reconstruction of the Dark Matter parameters can be performed. To begin with, all spatial information of the signals and in addition the whole $S2_b$ information is neglected. This is not only done to proof the concept of the implementation on an easier example, but also to have a counterpart to benchmark the influence of the additional information added to the problem in the next step.

Using only the $cS1$ information reduces the full posterior for the WIMP parameters, see equation (5.67), to

$$p(\Theta|cS1) \propto \frac{\lambda^n}{n!} p(\Theta) \exp(-\lambda f) \prod_{i=1}^{n} \mathcal{E}(cS1_{,i}) \int dE \mathcal{L}_{cS1_i}(E) p(E|\Theta). \qquad (6.5)$$

The posterior is sampled using the MCMC approach described in section 3.3.3, using 6 walkers each with 6000 samples plus 600 burn-in steps. Using ~10 % samples as burn-in has proven to be sufficient enough to let the walkers find their equilibrium, even when starting at a position further away from the truth. In this work the starting position of each walker is randomly initialized within ±30 % of the true parameter values.

Figure 6.5 shows the resulting reconstruction. In this example the true values have been hit almost spot on. Both the WIMP mass m_χ posterior and the cross-section σ_χ posterior peak around the truth, which was set to $\sigma_\chi = 3 \times 10^{-9}$ pb ($log(\sigma_\chi) = -8.52$) and $m_\chi = 50$ GeV ($log(m_\chi)$=1.70). Out of a total amount of $N_{Pois} = 21$ events only $n = 11$ events survived the efficiency selection. These surviving events contribute as an input for the calculations in the MCMC sampling of the posterior.

Table 6.3.: Dark Matter model parameters and prior choices for the implemented XENON100 signal model.

	mass	cross-section
prior	log-uniform	log-uniform
prior range	5-10000 GeV	10^{-12} - 10^{-6} pb

While the number of expected events directly scales with the underlying cross-section, the influence of different masses is more complicated, see again figure 6.1 for comparison. The influence of the mass is dependent on the kinematics of the interaction and other model parameters as described during the introduction in section 1.5.2. The interplay between the cross-section in the nominator and the WIMP mass in the denominator leads to a sort of the degeneration for the region of higher masses: For a given amount of events and a rising WIMP mass, the cross section has to compensate the dropping amount of expected events by growing itself. A rising WIMP mass leads to less sensitivity due to the dropping energy transfer for an interaction produced while considering the mass of the target xenon nuclei of ~131 GeV as a constant which in addition contributes to the tail towards higher WIMP masses. These tails in the posterior distributions are not always present. In cases where many events have been produced, e. g. due to upwards fluctuations during the event generation process, additional information can contribute
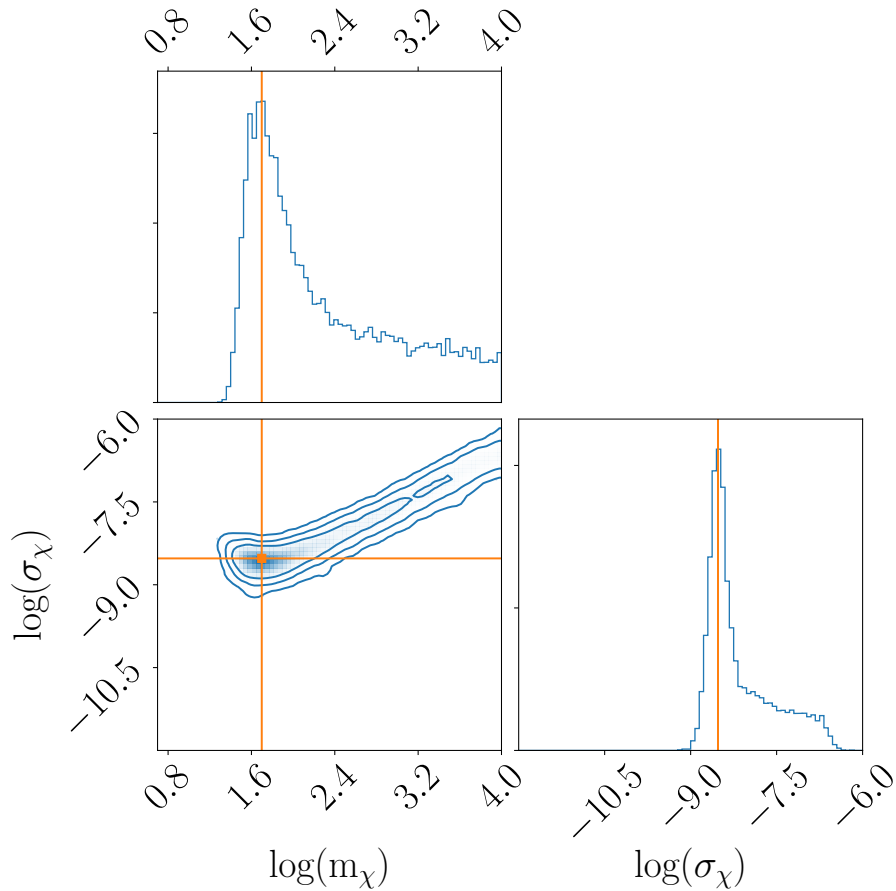
Figure 6.5.: Reconstruction of the WIMP mass m_χ and WIMP-nucleon cross-section σ_χ using only the $cS1$ signal. Since the prior pdfs on the parameters of interest were chosen to be flat in log-space, see table 6.3 for reference, the plot is also shown in log-space. The true underlying parameters are marked with an orange line at $m_\chi = 50\,\text{GeV}$ ($\log(m_\chi)$=1.70) and $\sigma_\chi = 3 \times 10^{-9}\,\text{pb}$ ($log(\sigma_\chi) = -8.52$) in all three parts of the plot. The two histograms show the marginalized posterior distribution of the mass m_χ (top) and cross-section σ_χ (bottom right). The central plot shows the 2D posterior of the reconstruction, which in this case is nicely concentrated around the real values. The contours within the central plot mark the different sigma levels, 1, 2 and 3 σ (standard deviation), that are used during the coverage study. In this particular reconstruction a total of 11 events survived the selection effects and contributed in the MCMC calculations.

to the reconstruction and less tails are visible. See some of the example reconstruction plots in appendix A for reference.

The overall performance is tested using a total of 100 parameter reconstructions. For each reconstruction the posterior mean and the highest posterior density point (HPD) is calculated and added to a histogram, see figure 6.6 for the mass on the left and for the cross-section on the right.
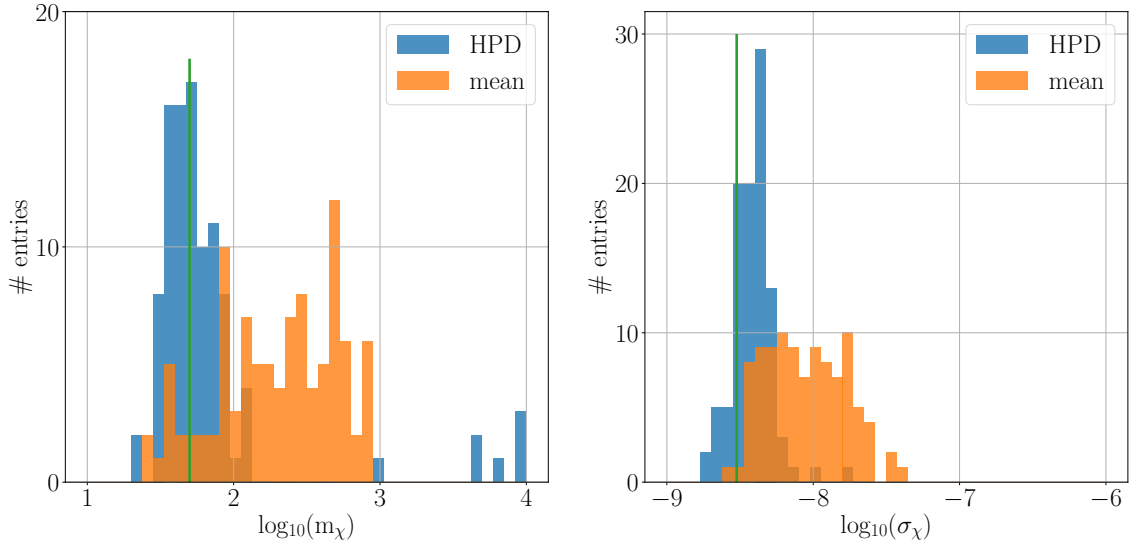
Figure 6.6.: Distribution of the posterior mean (orange) and HPD (blue) for 100 dark matter parameter reconstructions of mass (left) and cross-section (right). The true parameters are marked with a green line at $m_\chi = 50\,\mathrm{GeV}$ and $\sigma_\chi = 3 \times 10^{-9}\,\mathrm{pb}$. While the mean is strongly dependent on possible tails in the posterior distributions and thus is shifted to higher values away from the truth, the HPD just reflects the most probable value and is by construction not sensitive to the shape of a distribution. This makes the HPD a better measure for the performance of the reconstructions with a reduced amount of events (due to a smaller chosen true underlying cross-section).

The first thing to notice is the bad matching between the posterior mean and the truth. This is easy to explain though: Both posterior distributions, the one for the reconstructed mass as well as the one for the reconstructed cross-section, see again figure 6.5, have tails towards higher values which also leads to a shift of the mean to higher values. Tails in the distributions appear more often for reconstructions with fewer events since they are determined with less certainty due to the lack of information. As a result, the posterior mean values for these heavy tailed distributions with a smaller underlying cross-section seem to be worse. The HPD values on the other hand are not as much influenced by this effect. Here, the influence of the tails is less prominent although the lack of events and the corresponding lack of information still leads to a broader distribution of the HPD values compared to parameter configurations with larger event numbers. In general the true

values of the underlying dark matter parameters can be found in both cases if the amount of surviving events is large enough, see figure 6.7 for 100 experiments that have been produced with an underlying cross-section of $\sigma_\chi = 1 \times 10^{-8}$ pb resulting in an expected amount of 77.83 events, which corresponds to 40.5 events after applying the detector selection effects (the mean efficiency for the XENON100 detector is at 52 %).
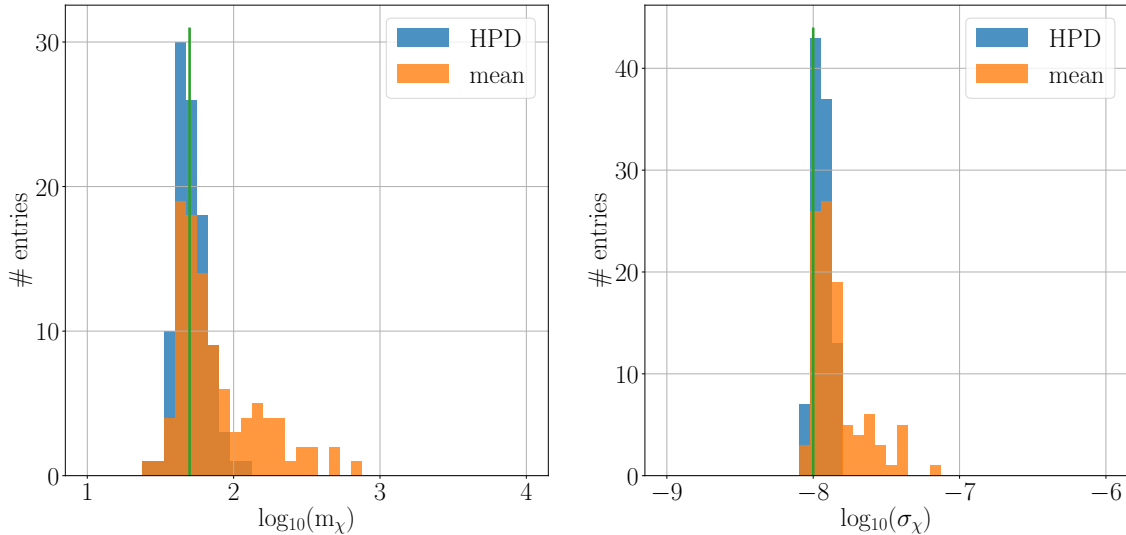
Figure 6.7.: Distribution of the posterior mean (orange) and HPD (blue) for 100 dark matter parameter reconstructions of mass (left) and cross-section (right). The true parameters are marked with a green line at $m_\chi = 50$ GeV and $\sigma_\chi = 1 \times 10^{-8}$ pb. Compared to figure 6.6 much more events contribute to the reconstructions and so the washed out tails of the posterior distributions are reduced. This leads to an improvement of the posterior mean towards the true values of the parameters. In addition the HPD also more concentrated around the true values due to the better performance of the reconstructions.

Here both, the posterior distribution HPDs and especially the mean values have a much smaller spread around the truth, which is marked as a green vertical line. This confirms the assumption that more events and therefore using additional prior knowledge, the posterior distributions of the reconstructions tend to be more symmetric and do not tend to generate heavy tailed posterior distributions. The HPD values have proven to be the preferred measure for cases of only a few events since it is by construction not dependent on the shape of the underlying posterior distributions but a good indicator for the most probable posterior value.

Having tested the whole pipeline of generating events to reconstructing the underlying WIMP parameters, the next section will focus on the more sophisticated model which is also taking into account the contribution of the S2 signal and the explicit spatial dependence of both signals. The new model is evaluated by comparing its reconstruction performance to the simple model presented earlier in this section.

6.3.2. Extended Analysis: Using Both, $S1$&$S2_b$ Information

To be able to use the previous study for comparison, the following analysis uses the same event information of the $S1$ signal but, in addition, includes the $S2_b$ signal and the spatial information. Since the events have already been produced with the full set of information in the first place, i. e. $S1$, $S2_b$ and 3D-position, they can be used out of the box and no new events have to be simulated. The events were generated to be uniformly distributed within the fiducial volume inside the XENON100 TPC. See figure 6.8 for the illustration of the simulated event positions for 100 different experiments, with a total of 1248 events.
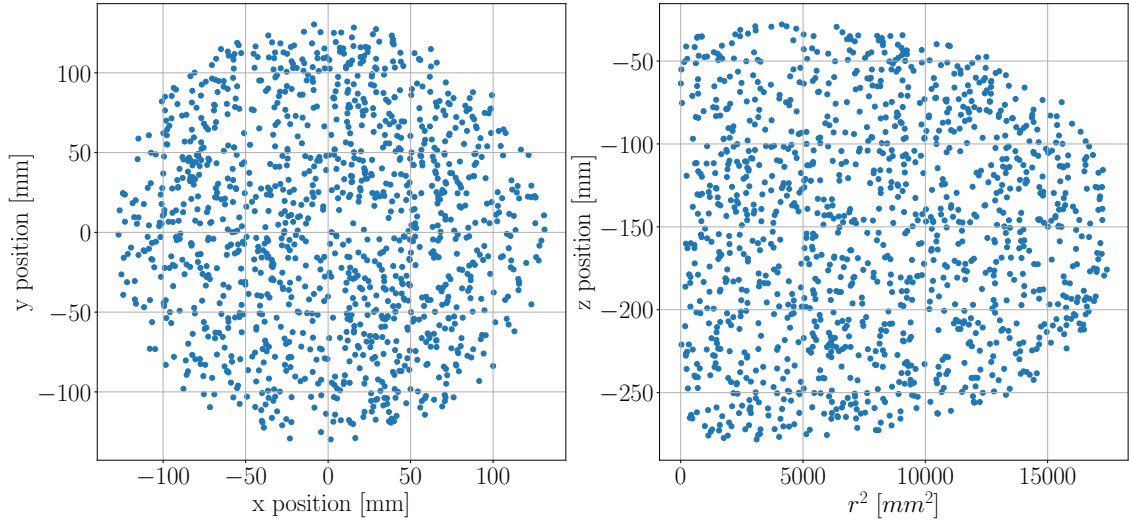
Figure 6.8.: Spatial distribution of 100 generated experiments in the x-y-plane (left) and depth (z position) vs. r^2 (right). The events are created uniformly distributed within the fiducial volume of the TPC, which is a ellipsoid positioned on the center of the TPC. This explains the rounded edges of the event distribution in the right plot. The underlying dark matter parameters were chosen to be a cross-section of $\sigma_\chi = 3 \times 10^{-9}$ pb and mass of $m_\chi = 50$ GeV. With these settings a total of 23.35 events per experiment are expected (before selection effects such as detection efficiency).

The volume is fiducialized to e.g. get rid of possible regions with a bad signal to background ratio. It tends to be a super-ellipsoid which is centered inside the TPC volume. This explains the smaller area in the x-y plane of the TPC compared to its dimensions (the radius of the whole XENON100 TPC is $r = 150$ mm) and also explains the "rounded" edges when looking at the event distribution in the z vs. r^2 plane, see again figure 6.8. The uniform distribution of the events was chosen to resemble the uniformly distributed dark matter particles for an earth bound experiment with a uniform local dark matter distribution of constant density. The underlying dark matter parameters were chosen with a mass of $m_\chi = 50$ GeV and a cross-section of $\sigma_\chi = 1 \times 10^{-8}$ pb. In addition to the spatial distribution, figure 6.9 shows the distribution of the signal in data space: The

first row of the figure shows the plain $S1$ vs. $S2_b$ data space and compares the spatially averaged data on the left with the uncorrected data on the right. One can clearly see the difference, e. g. the decreasing slope of the overall distribution. This difference is not as prominent in the second row of the plots. It shows the same data but in a different portrayal, namely $S1$ vs. $\log(S2_b/S1)$ which was one of the standard data spaces in the past since the $S2_b$ can be orders of magnitude larger than the $S1$ and the data appears less spread, see e.g. [7]. In the meantime most of the analyses are done using a complete 2D approach, i.e. inference is done using $S1$ and $S2_b$ together, and the native data space has become the preferred one, see e. g. [9].
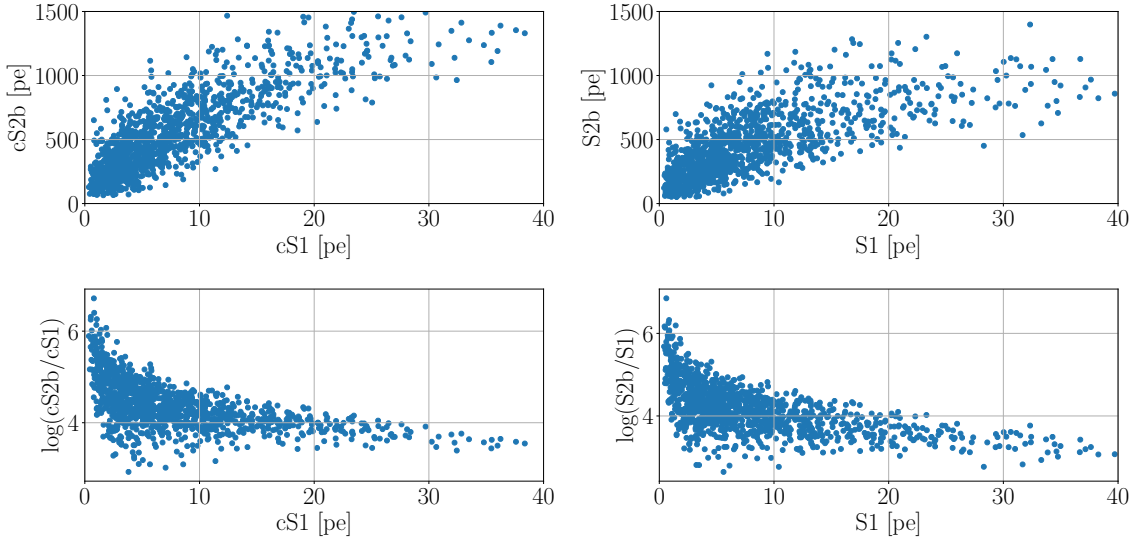
Figure 6.9.: Event distribution of 100 generated experiments. The underlying dark matter parameters were chosen to be a cross-section of $\sigma_\chi = 3 \times 10^{-9}$ pb and mass of $m_\chi = 50$ GeV. In the first row the data is shown in the native data-space of $cS1$ vs. $cS2_b$ (left) and $S1$ vs. $S2_b$ (right) respectively. The second row shows the same data in the more established data space $cS1$ vs. $\log(cS2_b/cS1)$ (left) and $S1$ vs. $\log(S2_b/S1)$ (right) respectively.

To analyse the reconstruction capabilities of the improved model, the full posterior pdf, as derived in equations (5.67), is used:

$$p(\Theta|S_{\text{tot}}) \propto \frac{\lambda^n}{n!} p(\Theta) \exp(-\lambda f) \prod_{i=1}^{n} \mathcal{E}(S_{\text{tot},i}) \int dE \mathcal{L}_{S1_i}(E) \mathcal{L}_{S2_i}(E) p(E|\Theta). \quad (6.6)$$

Figure 6.10 shows the reconstruction result that uses the same input parameters as the reconstruction done in the previous section but this time all the additional input parameters are used.

Comparing the old reconstruction from 6.5 with the new one, already by eye there are a few key differences visible: The standard deviation contours seem to be more narrow around the truth, which is again marked by the orange lines. Also the tails of the
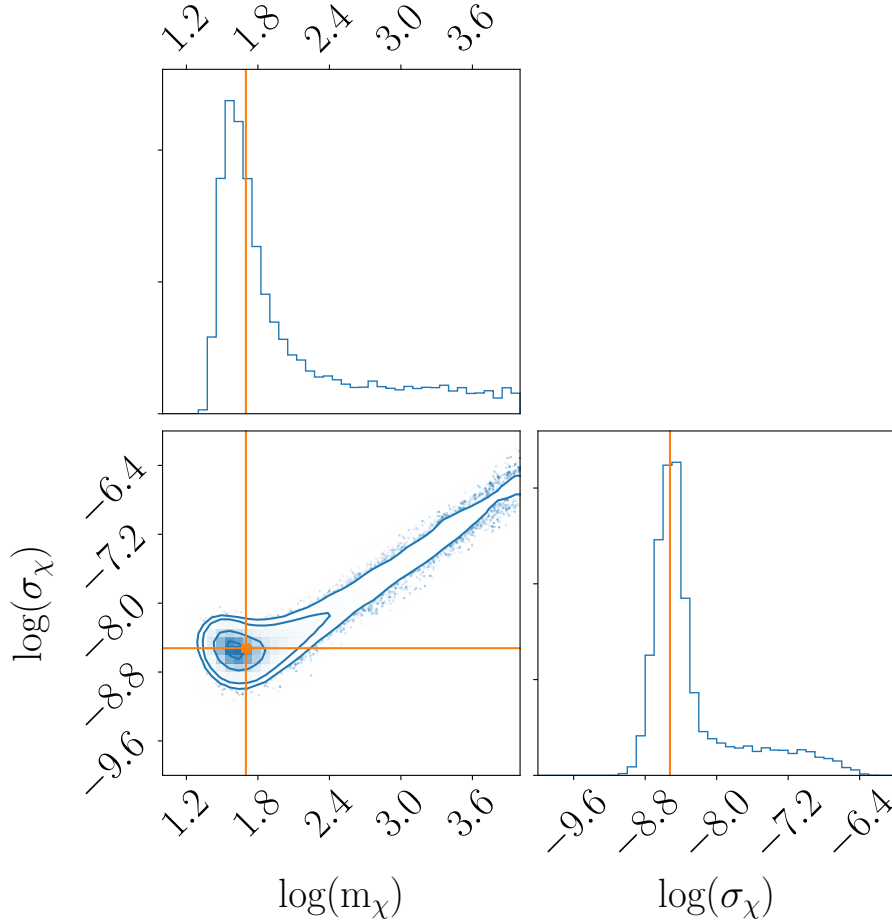
Figure 6.10.: Reconstruction of the WIMP mass m_χ and WIMP-nucleon cross-section σ_χ using both spatially dependent signals $S1$ and $S2_b$. Since the prior pdfs on the parameters of interest were chosen to be flat in log-space, see table 6.3 for reference, the plot is also shown in log-space. The true underlying parameters are marked with an orange line at $m_\chi = 50\,\text{GeV}$ ($\log(m_\chi)$=1.70) and $\sigma_\chi = 3 \times 10^{-9}\,\text{pb}$ ($log(\sigma_\chi) = -8.52$) in all three parts of the plot. The two histograms show the marginalized posterior distribution of the mass m_χ (top) and cross-section σ_χ (bottom right). The central plot shows the 2D posterior of the reconstruction, which in this case is nicely concentrated around the real values. The contours within the central plot mark the different sigma levels, 1, 2 and 3 σ (standard deviation), that are used during the coverage study. In this particular reconstruction a total of 11 events survived the selection effects and contributed in the MCMC calculations.

marginalized distributions for both mass and cross-section are less prominent. Of course, a comparison by eye is only a very subjective first step. This section will focus on presenting more sophisticated approaches to test if the new model will improve the dark matter parameter reconstruction capabilities.

As a measure to quantify the differences, the mean squared error (MSE) is used as the central value:

$$\text{MSE} = b_{m,\sigma}^2 + V_{m,\sigma}, \tag{6.7}$$

where V is the variance of the distribution and b the so called bias. The MSE measures the goodness of an estimator, i.e. how much the reconstructed parameter estimation differs from the truth. It is a strictly positive value and the closer to zero, the closer to the truth the chosen estimator will be, see e.g. [38]. The bias b is defined as the difference of the estimator from the truth:

$$b_{m,\sigma}^{HPD} = \text{HPD}_{m,\sigma} - \text{truth}_{m,\sigma}. \tag{6.8}$$

The estimator in the case of the parameter reconstructions are the mean and in addition the highest posterior density (HPD) of the mass m and cross-section σ posterior distributions. As shown in the section before, the HPD value proved to be the more accurate estimator compared to the posterior mean, so all the following calculations focus on the HPD. It has already been shown, that the HPD is less sensitive to the skewness and tails of distributions. Therefore the HPD should give a different insight in the comparison of the two models: While the MSE of the posterior mean will say more about the relative importance of tails or skewness of the posterior distributions, the posterior HPD has more significance towards how close the distribution peaks at the true value. For completeness the posterior mean calculations were still performed for the here chosen example parameter set and can be found in appendix B. Each of the 100 different $S1$-only reconstruction experiments is separately compared to the corresponding experiment of the improved model. To decide which reconstruction shows the superior performance, the MSEs of the $S1$-only models are subtracted from the MSEs of the improved model. If this measure results in a positive value, the new model outperformed the old one, i.e. the reconstructions deliver a prediction that is closer to the true values. See figures 6.11 and 6.12 for the histograms for the MSE differences for mass (blue) and cross-section (orange) using the posterior HPD as an estimator for the case of $\sigma_\chi = 3 \times 10^{-9}$ pb or expected number of events after selection of 48.2.

The x-axes of the histograms show the difference of the two MSEs, where zero (green line) would imply an equal performance of the reconstructions. In addition, for visualization purposes the MSE pairs are shown as a scatter-plot on the right hand side of the particular figures. Here the green dashed line again marks the position of equal errors, i.e. events falling in the region above the dashed line indicate reconstructions where the old $S1$-only model outperformed the improved model and the region below the green dashed contains the events with a better performance of the improved model.

In both cases, for the mass and the cross-section using the MSE as a measure of comparison, the improved model performs better. Using the posterior HPD as the estimator for the MSE, it has been shown that the reconstructions got more accurate. The HPD was 59 % (55 %) of the time closer to the true underlying mass (cross-section).
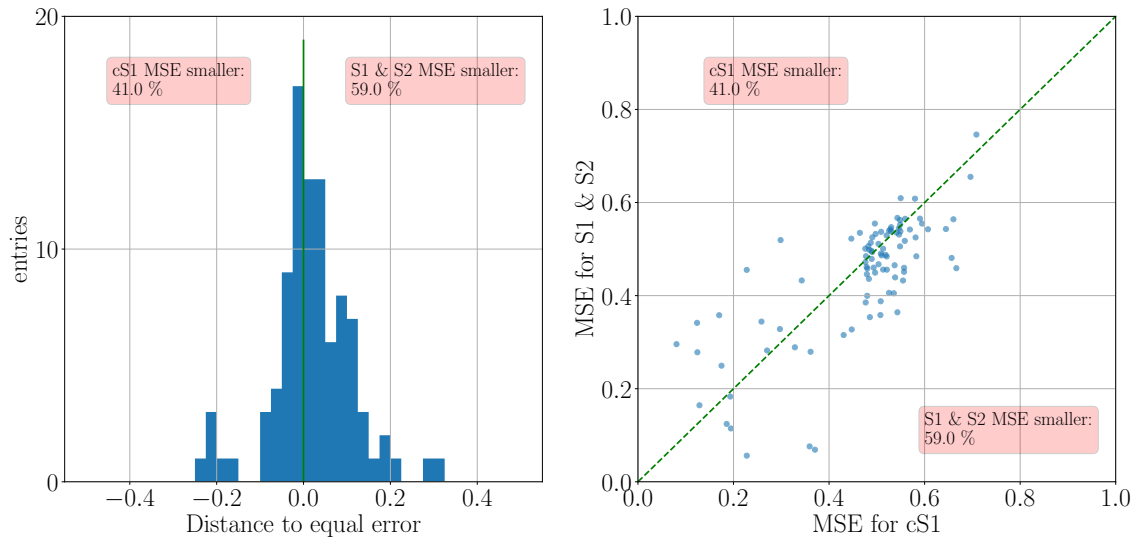
Figure 6.11.: Left: Histogram of the differences of the MSE for the two models using the HPD of the mass as an estimator. The green line indicates the point of equal error. Right: Scatter plot of the 100 MSE pairs. The green dashed line marks again the point of equal error.
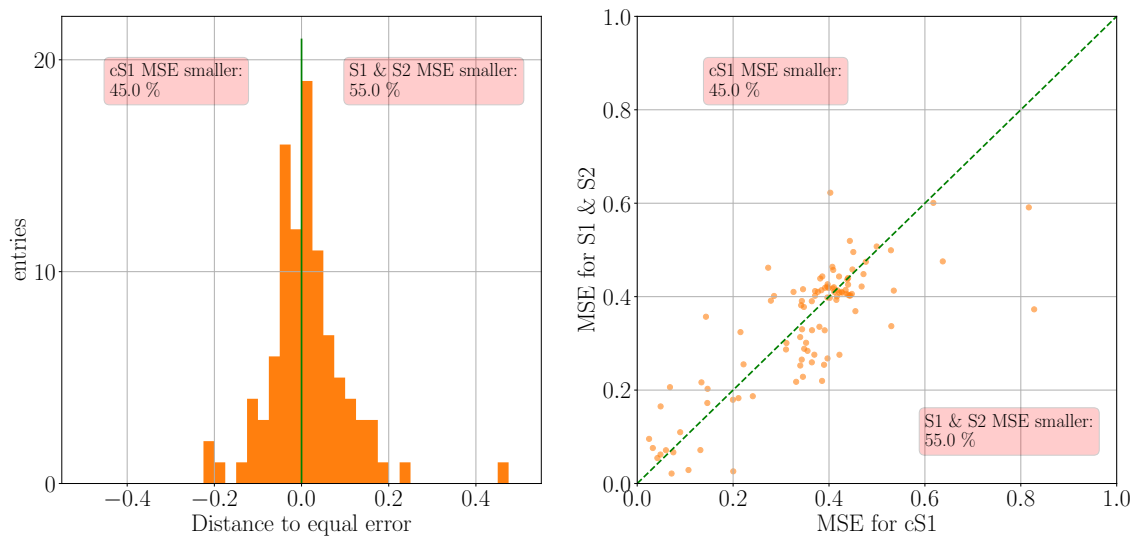
Figure 6.12.: Left: Histogram of the differences of the MSE for the two models using the HPD of the cross-section as an estimator. The green line indicates the point of equal error. Right: Scatter plot of the 100 MSE pairs. The green dashed line marks again the point of equal error.

In addition, using the posterior mean as an estimator showed that the reconstructions also got more robust against possible tails in the distributions (less skewed). The reconstruction of the mass (cross-section) performed better 52 % (53 %) of the time. This is especially helpful in the case of fewer measured events i. e. a smaller true underlying cross-section.

Both improvements are especially beneficial for rare event experiments, where the amount of expected signal events is close to zero most of the time.

To round off this analysis, the coverage of the different reconstructions is calculated. Two different Bayesian approaches of credibility intervals will be used to check the coverage. First, inspired by the classical frequentist confidence interval (CI), the equal-tailed interval with 68 % and 95 % confidence is used to check whether the true value of mass or cross-section falls within that region. This method uses the quantile values of the distribution to define the left and right intervals: The $1 - 0.68 = 0.32$ ($1 - 0.95 = 0.05$) quantile for the left and the 0.68 (0.95) quantile for the right border for the case of the 68 % (95 %) credible interval, see figure 6.13 for an illustration of the calculated intervals for an arbitrary choice of a set of posterior distributions from the reconstructions.
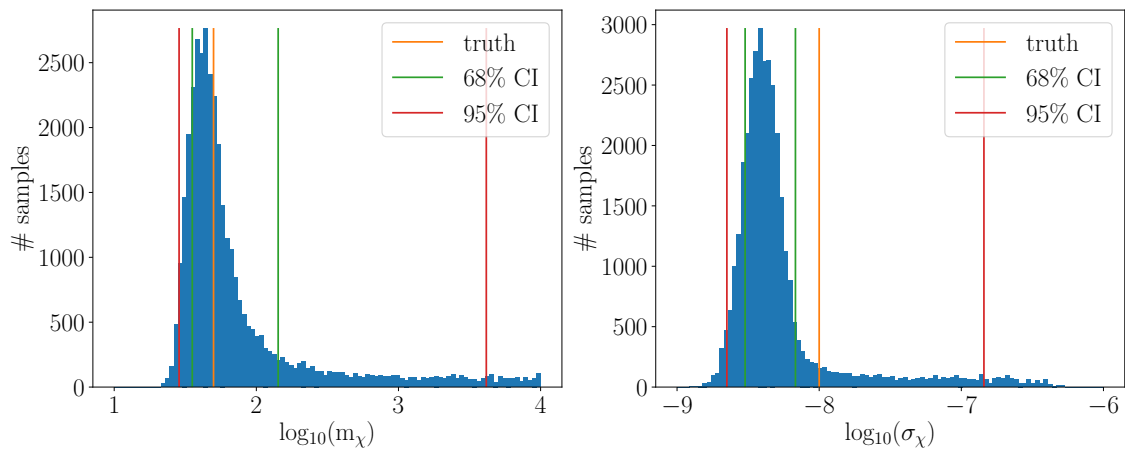
Figure 6.13.: Arbitrary selection of posterior distributions for WIMP mass m_χ (left) and cross-section σ_χ (right) to illustrate the equally tailed credible interval. The green (red) vertical line indicate the 68 % (95 %) interval. The orange line marks true values at m_χ=50 GeV and $\sigma_\chi = 3 \times 10^{-9}$ pb.

As there are posterior distributions whose tails extend well above the prior parameter range, this obviously may not be the best approach since the upper boundary will be dependent on the chosen prior range. Therefore the credible interval in addition is also calculated by using the highest posterior density interval (HPDI). This Method is especially useful when the distribution of interest is uni-modal, which is given for the case studied in this work. By definition the HPDI yields the smallest interval to include 68 % (95 %) of the distributions most probable values. See figure 6.14 for illustration of the HPDI. The same distribution as in the previous study for the equally-tailed interval has

been used to have a direct comparison of the two different methods.
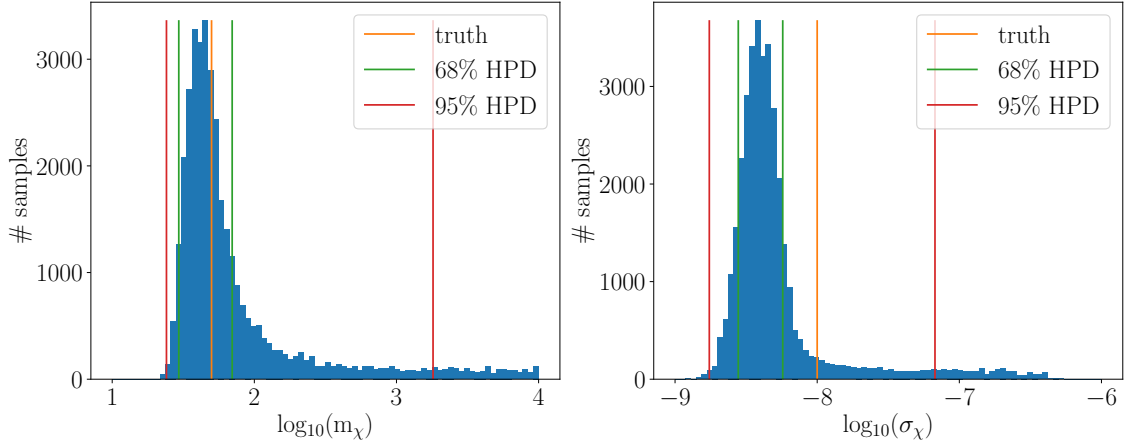
Figure 6.14.: Same selection of posterior distributions for WIMP mass m_χ (left) and cross-section σ_χ (right) as in the previous figure. Here the highest posterior density interval is shown. The green (red) vertical line indicate the 68 % (95 %) interval. The orange line marks true values at m_χ=50 GeV and $\sigma_\chi = 3 \times 10^{-9}$ pb.

Figure 6.15 shows the result of the coverage study. In seven out of eight cases while comparing the green (old) with the red (new) bars for the 68 % coverage intervals and the yellow (old) with the blue (new) bars for the 95 % coverage intervals, the new model shows a higher coverage, i.e. more values fall within the interval including the truth. This confirms the earlier findings that the new model did improve the reconstruction capability and also its accuracy. In addition there is a clear deviation concerning the different credible interval methods. While the equally tailed interval (ETI) method shows a clear under-coverage for the 68 % interval, the highest posterior density interval (HPDI) performs much better and even hints towards a slight over-coverage. Even while being the smallest possible interval by construction, the HPDI contains the truth much more often. This again is caused by the heavily tailed posterior distributions that form for reconstructions with too few events as input information. It is clear, that constructing the intervals by using quantiles of the distributions like it is done for the ETI, there is a big influence of the range of the prior distribution and also on how distinct the individual tails are. This again qualifies the method including the HPD value as the key point in the executed analysis since it is mostly independent of the skewness and tails of the studied distributions. As the amount of events grows, the huge gap in coverage between the two methods starts to disappear, since there also will be less tails present in the posterior distributions.

All analyses have also been performed for different sets of underlying dark matter parameters, see appendix D for a selection of figures. Overall, it can be concluded that there is an obvious systematic improvement for reconstructions using the new and improved
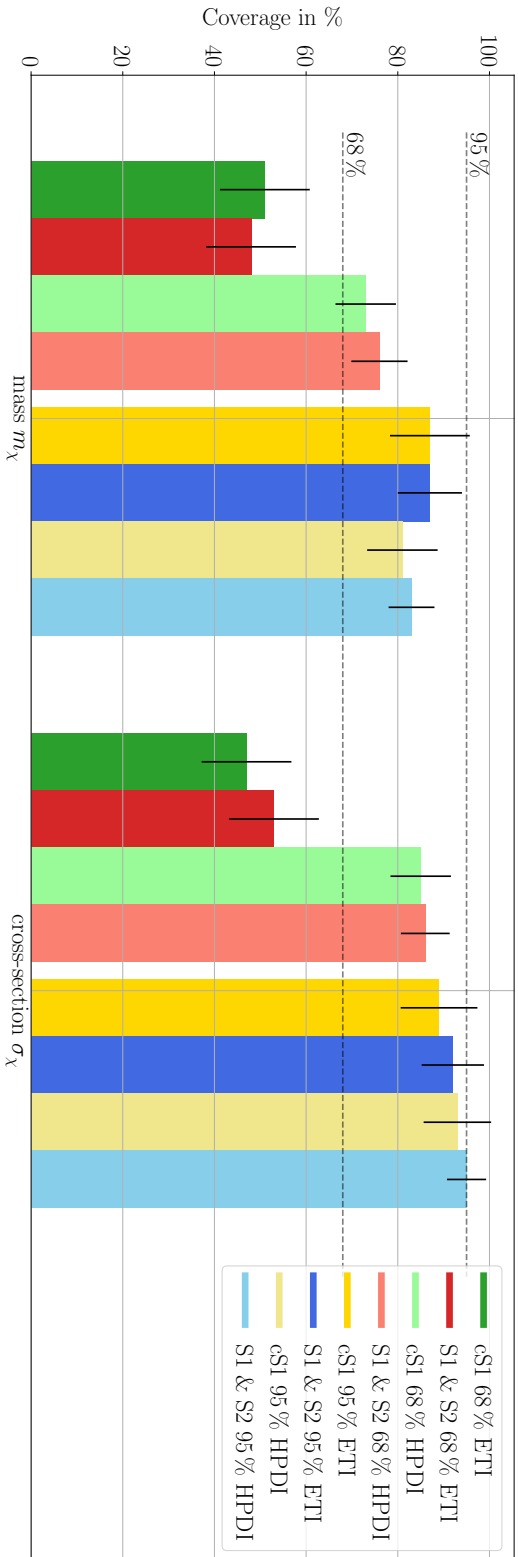
Figure 6.15.: Coverage of the WIMP mass m_χ=50 GeV (left) and the WIMP-nucleus cross-section $\sigma_\chi = 3 \times 10^{-9}$ pb (right) for different analysed configurations. The green and red bars compare the performance of the old (green) and new (red) models for the 68 % coverage, while the colour saturation differentiates the methods used to calculate the coverage, i. e. the pale colours mark the highest posterior density interval (HPDI) and the full saturated colours mark the equally tailed interval (ETI). The same has also been done for the 95 % coverage, see the yellow and blue bars which again compares the old and new model coverage performance. The saturation in colours, like before, marks the different methods of coverage. Overall the new model outperforms the old model also in coverage.

model introduced in this work. Especially when there are less events expected and the additional information used in the improved model helps to compensate this lack of information. On the other hand, when there are enough events measured, the difference gets less prominent.

6.4. Setting an Upper Limit for a Background-free Experiment

One of the remaining questions is the performance of the new model for the task of setting an upper limit. Since in this work, there is no background model introduced to the analysis framework, an upper limit can only be calculated for the case of zero measured events. Even with just one measured event, without a background model involved this would already imply a discovery. Although the reconstruction of a possible set of DM parameters would turn out to be very inaccurate because of the lack of input information. By invoking zero events into the framework, the maximal possible sensitivity of the background-free detector can be calculated. See figure 6.16 for a reconstruction result, where there was no other input than the detector parameters.

Clearly the reconstruction looks very different from the ones invoking signal information. The posterior distributions are not clustering around a certain value, the marginalized cross-section posterior (lower right hand side histogram) forms a plateau towards lower values and keeps dropping rapidly after passing a certain threshold cross-section. This threshold marks the region where the cross-section would still yield a compatible amount of events, which would be zero in this case. The marginalized posterior distribution for the mass (upper left histogram) on the other hand, shows a rather different behaviour. Instead of a peaking distribution around the true underlying WIMP mass, it shows a minimum around the most sensitive mass range of the detector, following figure 6.1 that shows the mass dependent number of expected events. This behaviour is mirrored in the posterior mass distribution of figure 6.16.

To calculate a mass dependent limit for the zero event case, the 2D posterior distribution is sliced in 60 mass bins. For the sake of getting enough statistics in the individual mass bins, the reconstruction is done 100 times each with 36000 samples, which in the end yields a total of 3.6 million samples. All reconstructions are pooled to form one huge data-set to gain more events per bin needed in the next step of the analysis. Looking at one individual mass slice results in the histogram shown in figure 6.17. This very much looks like the marginalized cross-section posterior distribution, but only represents one slice in mass. To finally be able to calculate an upper limit, these histograms are fitted with a suiting step-like function. Two fitting representations were tested: First, the Fermi-Dirac function with an additional amplitude parameter

$$f_{\text{FD}}(x) = \frac{A}{e^{(x-B)/C} + 1} \, , \tag{6.9}$$

where A is the amplitude or the height of the plateau, B is the point of half height or turning point and C defines how fast the function falls to zero and is a measure for the width of the function.
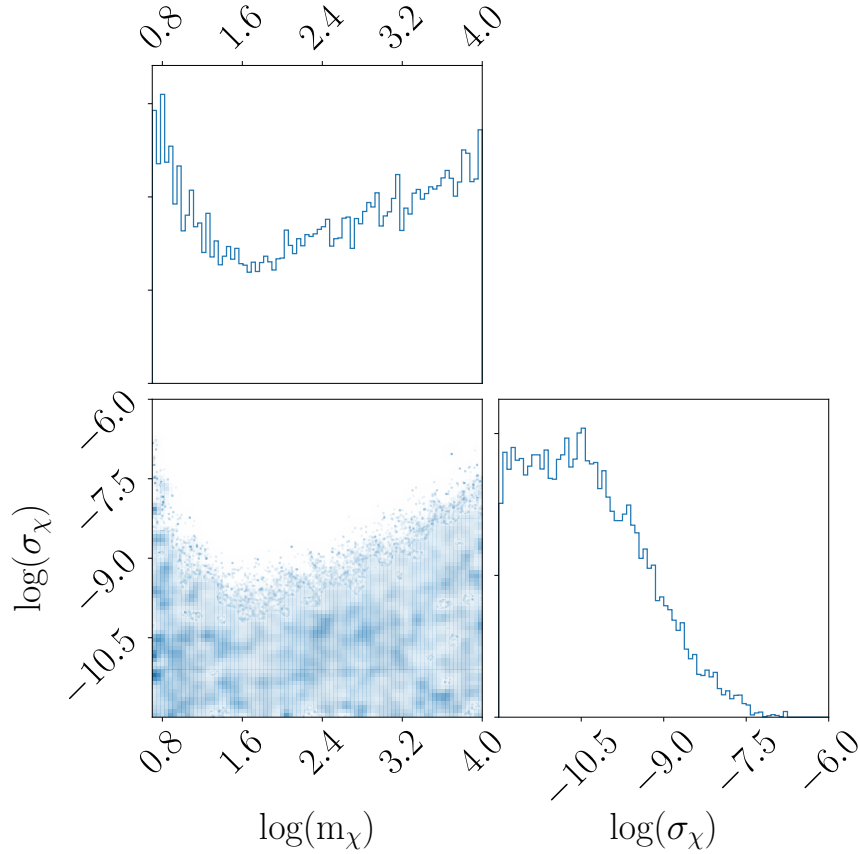
Figure 6.16.: Reconstruction of the WIMP mass m_χ and WIMP-nucleon cross-section σ_χ using the improved model as described in section 6.3.2. Since the prior pdfs on the parameters of interest were chosen to be flat in log-space, see table 6.3 for reference, the plot is also shown in log-space. The true underlying parameters were chosen to be $m_\chi = 50\,\text{GeV}$ ($\log(m_\chi)$=1.70) and $\sigma_\chi = 0$ to produce no events for all three parts of the plot. The two histograms show the marginalized posterior distribution of the mass m_χ (top) and cross-section σ_χ (bottom right). The central plot shows the 2D posterior of the reconstruction, which does not show any peaks in the given parameter range. Following figure 6.1, the most events are expected in the region of 30-50 GeV which is reflected in the 2D posterior distribution (center). In this mass region the corresponding cross-section does not extend to very large values.

Second, a threshold function including the error function

$$f_{\text{thres}}(x) = \frac{A}{2} \left[1 - \text{erf}\left(\frac{x - B}{C} \right) \right] , \tag{6.10}$$

whose parameters can be interpreted like in the previous case. Since the threshold function resulted in a slightly smaller goodness of fit value χ^2, its parameters were chosen as an input for the limit calculations.

The upper limit will be chosen to be the parameter B (the turning point of the distribution), see again figure 6.17 for a generic example of the fit, see appendix C for additional plots.
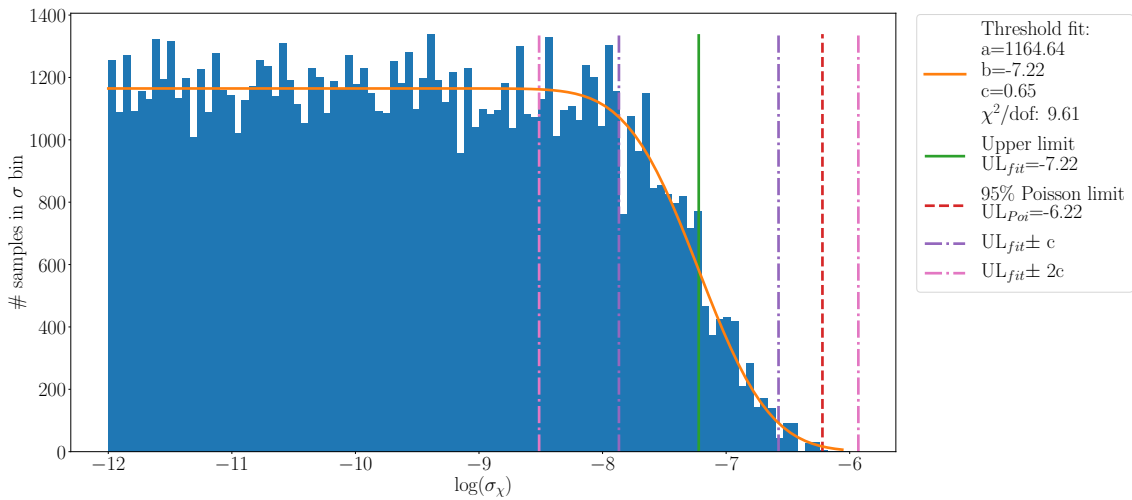
Figure 6.17.: Cross-section distribution for an arbitrarily chosen mass slice at a WIMP mass between 5 GeV and 5.7 GeV. Also shown are the threshold fit defined in equation (6.10) (orange line) and the chosen upper limit for the particular mass bin (green line) in form of the fit parameter b. In addition the 95 % Poisson limit (red line) as well as the width parameter with respect to the limit (purple line) are shown. This fit is performed for each individual mass bin.

After fitting the cross-section distribution for each mass slice and extracting the the parameters B (turning point), the resulting limit is shown in figure 6.18 (blue point/line). The shape resembles a typical upper limit, see e.g. the XENON1T upper limit in figure 2.14 for comparison. Since the new model is based on the XENON100 configuration and response, the upper limit can be interpreted as the best possible performance the XENON100 detector could have delivered in the absence of background events. As a measure for the spread or uncertainty of the calculated upper limit, the width parameter C of the threshold fit, see equation (6.10), was used (orange and green points/lines).

To further guide the eye and also to justify the method of the limit calculation, an additional Poisson limit has been calculated and added to the plot, see the red points/line

in figure 6.17. A 95 % upper Poisson limit is set if 2.3 events have been detected while expecting none. For this calculation equation (6.2) was used by fixing the masses to m_i in the correction factor $f(\Theta)$ and optimizing the cross-section in $\lambda(\Theta)$ so the number of observed events yields n_i=2.3 events:

$$n_i(\sigma_\chi) = 2.3 = f(m_i) \cdot \lambda(m_i, \sigma_\chi). \tag{6.11}$$

The Poisson limit nicely follows the shape of the zero-events limit and confirms the validity of the chosen limit calculation method of using the threshold function for fitting the cross-section distributions for the different mass slices. To again emphasize the importance of the formerly introduced correction factor $f(\Theta)$, figure 6.17 also shows the Poisson limit without using the correction factor, see the purple points/line. It is clearly visible, that below ~80 GeV the correction factor plays a major role: It inherits the efficiency of the detector for small energy transfers that occur for low WIMP mass interactions.

6.5. Summary of Results

In this chapter the new model has been tested thoroughly. After having checked the general event generation, see figure 6.2, the implementation of the selection effects and efficiencies by introducing a correction factor was confirmed by a monte carlo simulation, see figure 6.4. Using the cS1-only analysis as a benchmark, it has been shown that using the full signal and full spatial information within the signal model does improve the capability of reconstructing the dark matter parameters of interest, i.e. WIMP mass m_χ and spin independent WIMP-nucleus cross-section σ_χ, see figures 6.11 and 6.12. In the last part of the analysis a background free upper limit calculation was performed by using the results of zero event parameter reconstructions, see figure 6.18.
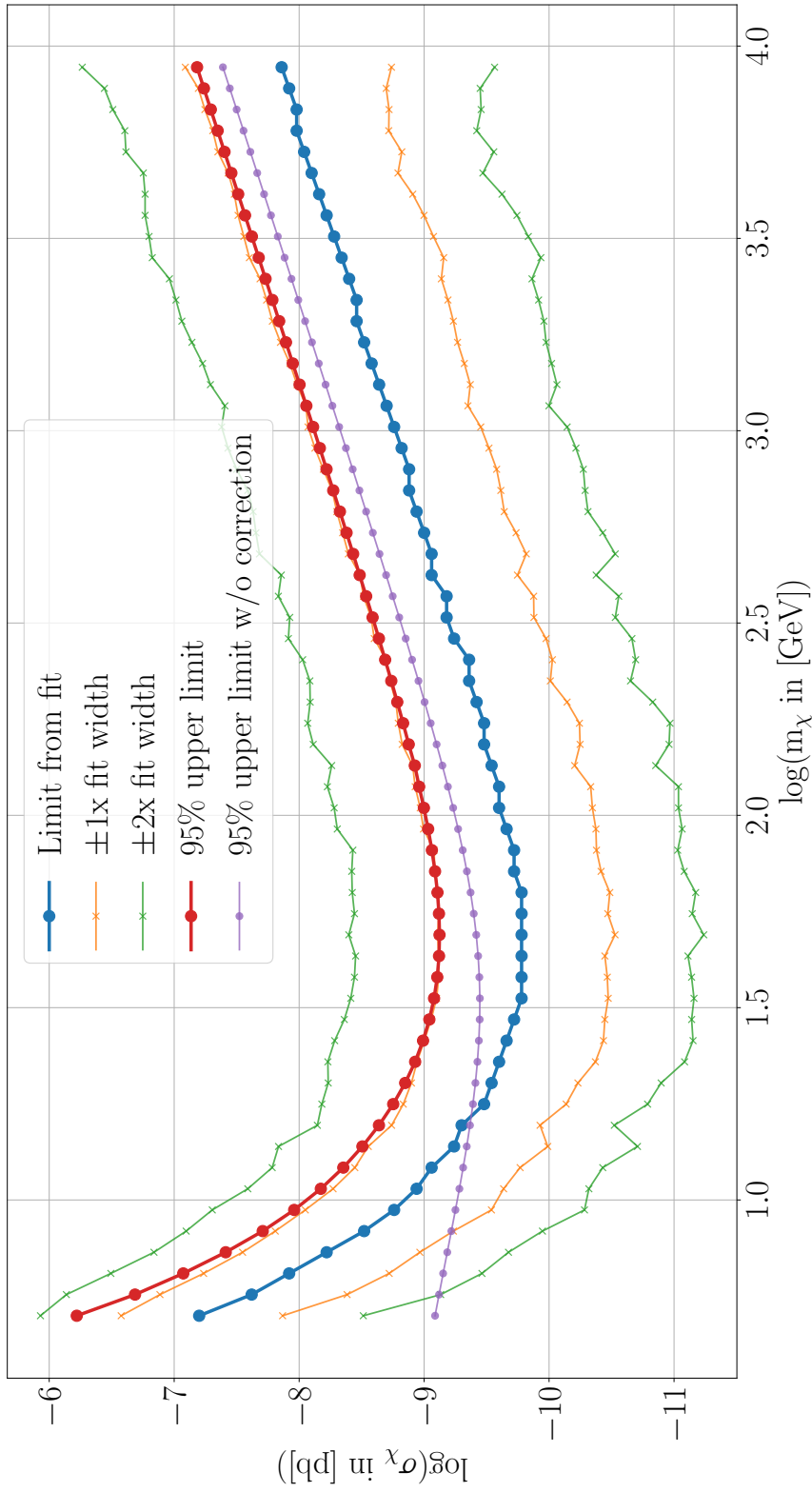
Figure 6.18.: Upper limit for the background free signal model using the XENON100 configuration and response (blue line/points). As a measure for the spread of the limit, also the width of the fit is treated like a standard deviation: The orange (green) line/points are the normal (double) fit width. For comparison and confirmation, the 95 % Poisson limit is also shown (red line/points). The purple line/points show the Poisson limit without applied correction factor.

Chapter 7

Summary and Outlook

The first analysis performed in this thesis deals with the data driven determination of the software trigger efficiency of the XENON1T data acquisition system in chapter 4. It is an important cross check on the chosen S2 analysis threshold, which is set to 200 pe and complements the simulation driven analysis which can be found in [1]. To be able to perform the data driven analysis, a lot of effort is put into selecting and cleaning the data by writing custom data extractors (minitree makers). After the extraction has been successful, different quality cuts are applied to further clean the data from different kinds of unwanted events. Finally, the cleaned data is used to calculate different efficiencies. For the S2 trigger efficiency, the results agree with the chosen XENON1T analysis S2 threshold for both data collection periods, i. e. sciencerun0 and sciencerun1. The choice of 200 pe as a conservative analysis threshold could be confirmed. One could have argued to choose an even lower threshold at ~180 pe but, to stay as conservative as possible, the higher threshold has been been favored by the XENON1T collaboration. While the results are overall in agreement with the alternative simulation study, both approaches suffer from different weaknesses that may explain the visible differences: While the simulation has no problem with low statistics it is heavily reliable on the model used in the waveform simulator and may be less conservative and so tends to yield higher overall efficiencies. The data driven method on the other hand is independent of the model, but at the same time it is heavily reliable on data selection cuts and other intrinsic detector efficiencies.

The second analysis and main topic of this thesis emphasises a completely different topic. It consists of two parts:

The first part of the analysis in chapter 5 introduces a new approach to integrate efficiencies into the TPC signal model. While XENON100 has been used as a template detector, the model has been developed to be as flexible as possible to be easily adaptive to future generations like the XENON1T detector. The necessary rework of the likelihood functions for both fundamental detector signals, i.e. $p(S1|E,\vec{r})$ in section 5.1 and $p(S2|E,\vec{r})$ in section 5.2 is followed by the description hot wo invoke the detector signal efficiencies into the signal model in section 5.3. Parameter estimation is formulated as a Bayesian hierarchical model and the detector as well as the selection efficiencies will be included in a fundamental way. The posterior likelihood function for the Dark Matter parameter estimation is prepared in section 5.4 for later use, where the improved model is tested

thoroughly.

The second part of the analysis in chapter 6 contains detailed tests and simulations to check the validity and performance of the new model. After having checked the general event generation in section 6.1, the implementation of the selection effects and their resulting efficiencies by introducing a correction factor to the model is shown in section 5.3. The validity of the implementation is checked by a Monte Carlo simulation, see figure 6.4, which shows the expected behavior. As a representative for the old approach, the cS1-only analysis is used as a benchmark. As a result it is shown that the usage of the full signal information, i.e. S1 and S2 while also keeping the full spatial information, the signal model does improve the capability of reconstructing dark matter parameters of interest, i.e. WIMP mass m_χ and spin independent WIMP-nucleus cross-section σ_χ, see sections 6.3.2. As a second cross check and first application of the improved model, a background free upper limit calculation for the cross section is performed in section 6.4. By comparing the Poisson limit to the mass slice fitting approach, again we see that the model performs as expected and nicely follows the the Poisson limit shape while resulting in a lower limit at the same time.

The construction of the XENON1T successor experiment, XENONnT is already in its final stages. Here, a decision on the S2 analysis threshold still has to be made. With two well established methods, the one presented in this work and the alternative simulation approach, it should be again possible to choose the lowest possible, but still conservative S2 threshold.

The improved signal model developed in this work can be used to handle the signal efficiencies in a straight forward and fundamental way. The flexibility of the developed framework should make it easy to adapt the configuration to a new detector configuration.

Appendices

A. Additional reconstruction plots
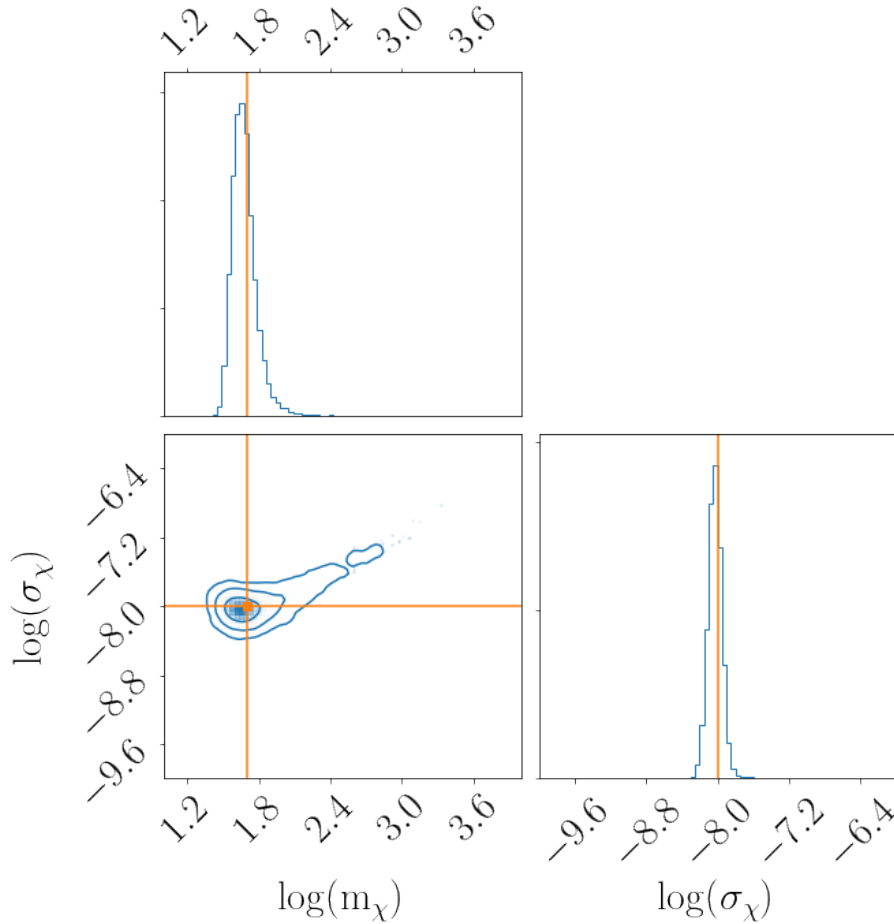
Figure A.1.: Reconstruction of the WIMP mass m_χ and WIMP-nucleon cross-section σ_χ using both spatially dependent signals $S1$ and $S2_b$. Since the prior pdfs on the parameters of interest were chosen to be flat in log-space, see table 6.3 for reference, the plot is also shown in log-space. The true underlying parameters are marked with an orange line at $m_\chi = 50\,\text{GeV}$ ($\log(m_\chi)$=1.70) and $\sigma_\chi = 1 \times 10^{-8}\,\text{pb}$ ($log(\sigma_\chi) = -8.00$) in all three parts of the plot. The two histograms show the marginalized posterior distribution of the mass m_χ (top) and cross-section σ_χ (bottom right). The central plot shows the 2D posterior of the reconstruction, which in this case is nicely concentrated around the real values. The contours within the central plot mark the different sigma levels, 1, 2 and 3 σ (standard deviation), that are used during the coverage study. In this particular reconstruction a total of 36 events survived the selection effects and contributed in the MCMC calculations.
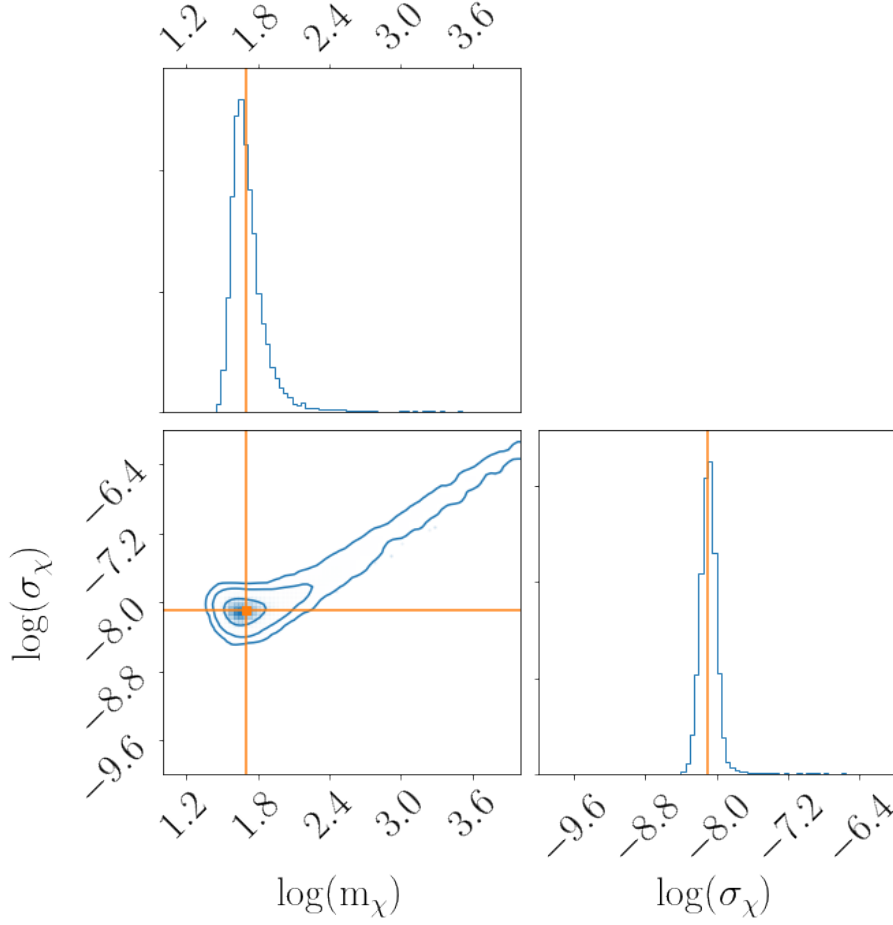
Figure A.2.: Reconstruction of the WIMP mass m_χ and WIMP-nucleon cross-section σ_χ using both spatially dependent signals $S1$ and $S2_b$. Since the prior pdfs on the parameters of interest were chosen to be flat in log-space, see table 6.3 for reference, the plot is also shown in log-space. The true underlying parameters are marked with an orange line at $m_\chi = 50\,\text{GeV}$ ($\log(m_\chi)$=1.70) and $\sigma_\chi = 8 \times 10^{-9}\,\text{pb}$ ($log(\sigma_\chi) = -8.10$) in all three parts of the plot. The two histograms show the marginalized posterior distribution of the mass m_χ (top) and cross-section σ_χ (bottom right). The central plot shows the 2D posterior of the reconstruction, which in this case is nicely concentrated around the real values. The contours within the central plot mark the different sigma levels, 1, 2 and 3 σ (standard deviation), that are used during the coverage study. In this particular reconstruction a total of 35 events survived the selection effects and contributed in the MCMC calculations.
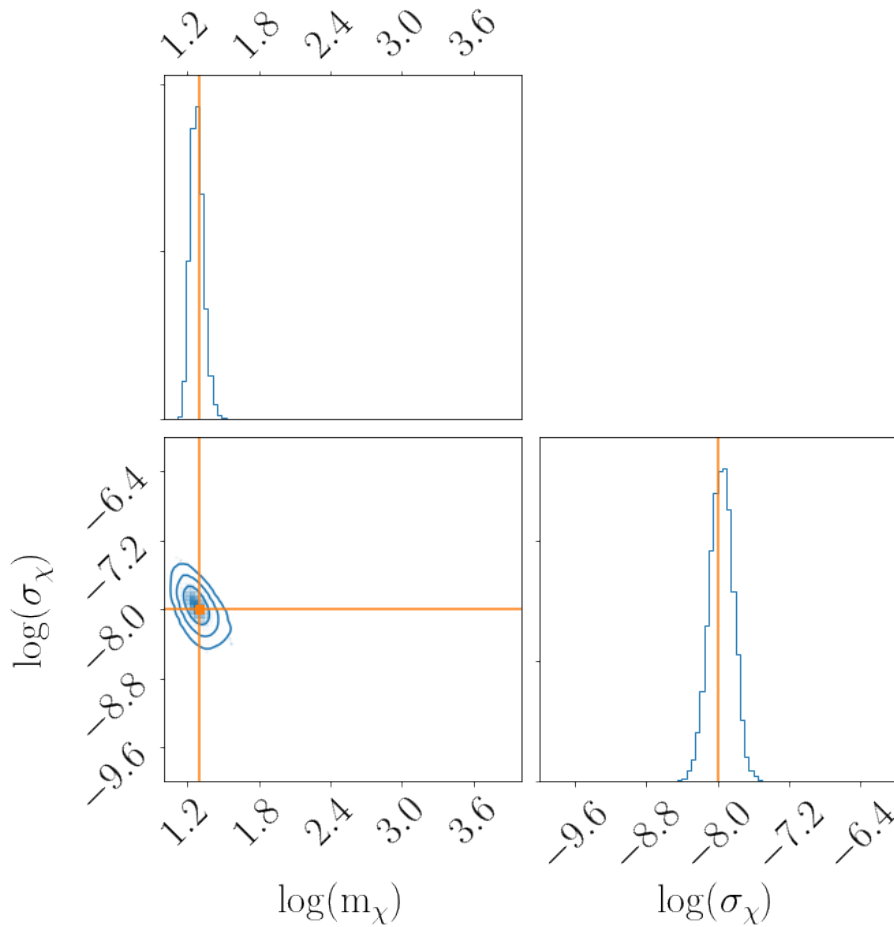
Figure A.3.: Reconstruction of the WIMP mass m_χ and WIMP-nucleon cross-section σ_χ using both spatially dependent signals $S1$ and $S2_b$. Since the prior pdfs on the parameters of interest were chosen to be flat in log-space, see table 6.3 for reference, the plot is also shown in log-space. The true underlying parameters are marked with an orange line at $m_\chi = 20\,\mathrm{GeV}$ ($\log(m_\chi)$=1.30) and $\sigma_\chi = 1 \times 10^{-8}\,\mathrm{pb}$ ($log(\sigma_\chi) = -8.00$) in all three parts of the plot. The two histograms show the marginalized posterior distribution of the mass m_χ (top) and cross-section σ_χ (bottom right). The central plot shows the 2D posterior of the reconstruction, which in this case is nicely concentrated around the real values. The contours within the central plot mark the different sigma levels, 1, 2 and 3 σ (standard deviation), that are used during the coverage study. In this particular reconstruction a total of 32 events survived the selection effects and contributed in the MCMC calculations.

B. Model comparison using the posterior mean as an estimator
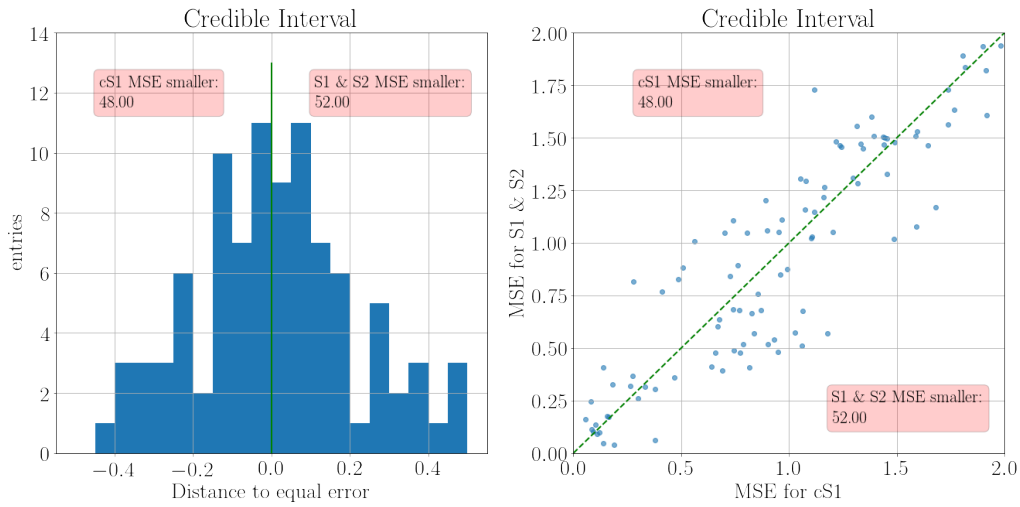
Figure B.4.: Left: Histogram of the differences of the MSE for the two models using the posterior mean of the mass as an estimator. The green line indicates the point of equal error. Right: Scatterplot of the 100 MSE pairs. The green dashed line marks again the point of equal error.
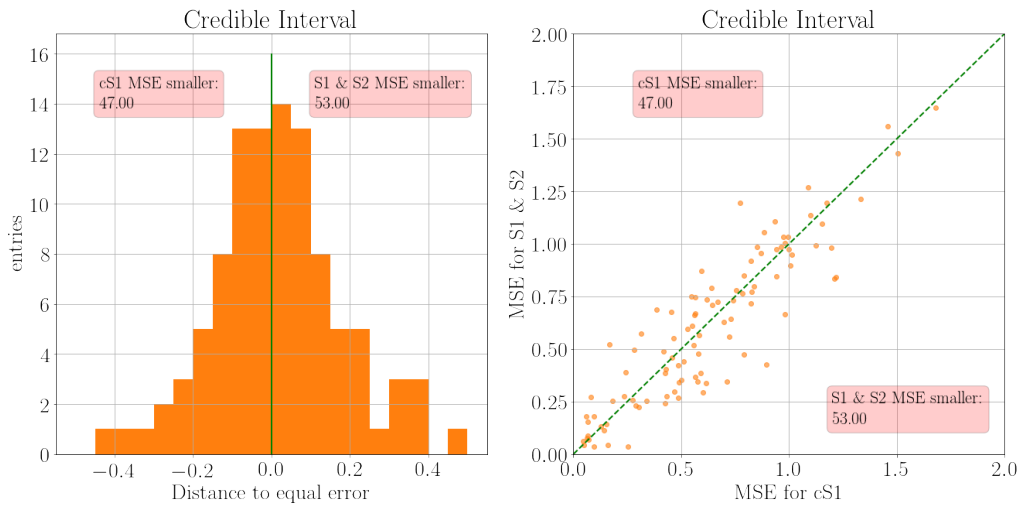
Figure B.5.: Left: Histogram of the differences of the MSE for the two models using the posterior mean of the cross-section as an estimator. The green line indicates the point of equal error. Right: Scatterplot of the 100 MSE pairs. The green dashed line marks again the point of equal error.

C. Selection of limit fits

C.1. Using the Threshold function
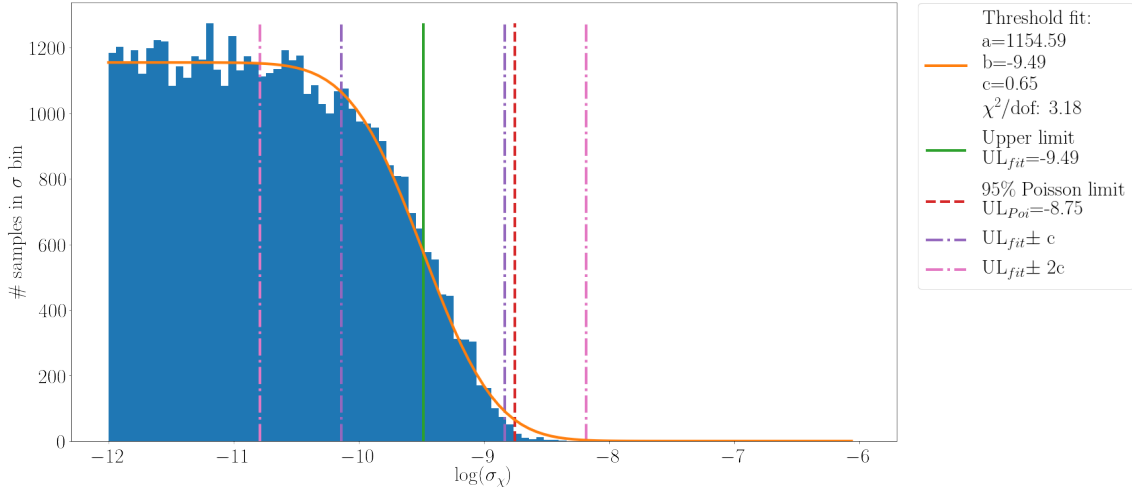
Figure C.6.: Cross-section distribution and threshold fit for the WIMP mass slice between 18-20 GeV.
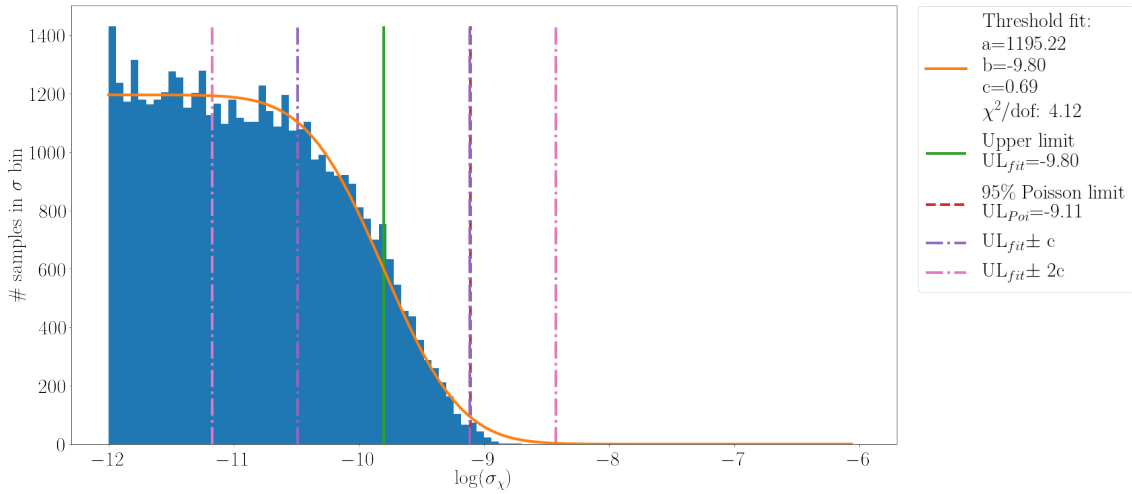
Figure C.7.: Cross-section distribution and threshold fit for the WIMP mass slice between 63-72 GeV.
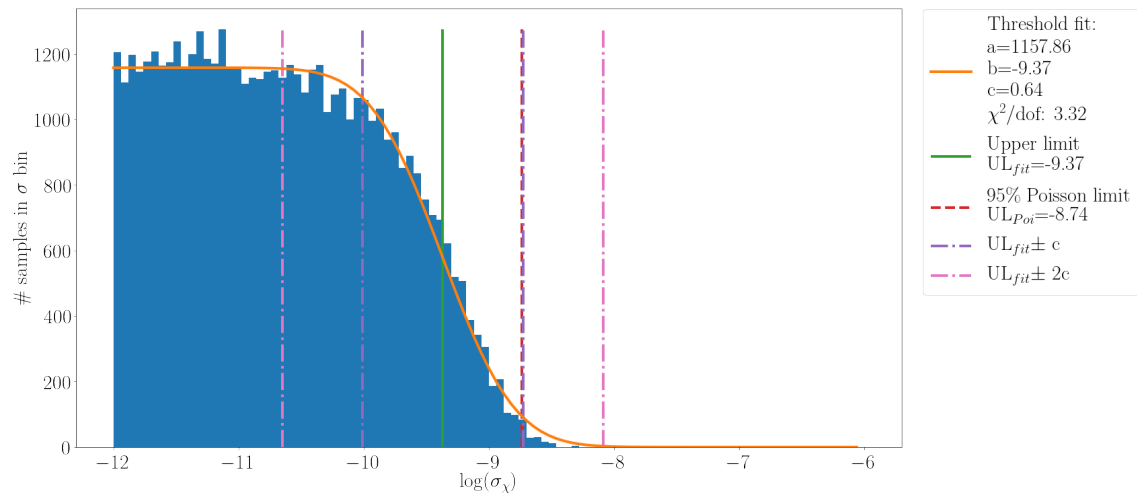
Figure C.8.: Cross-section distribution and threshold fit for the WIMP mass slice between 224-254 GeV.
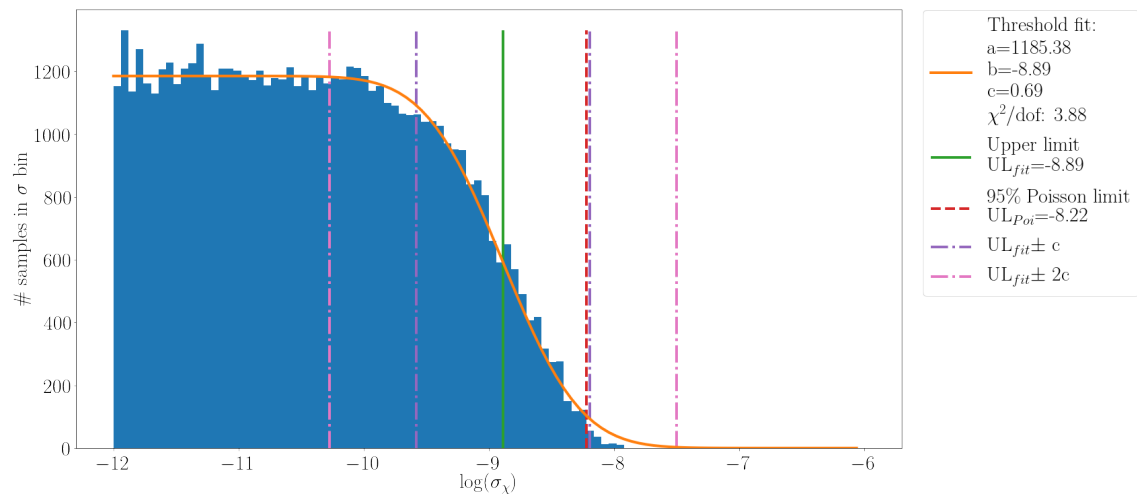
Figure C.9.: Cross-section distribution and threshold fit for the WIMP mass slice between 794-901 GeV.
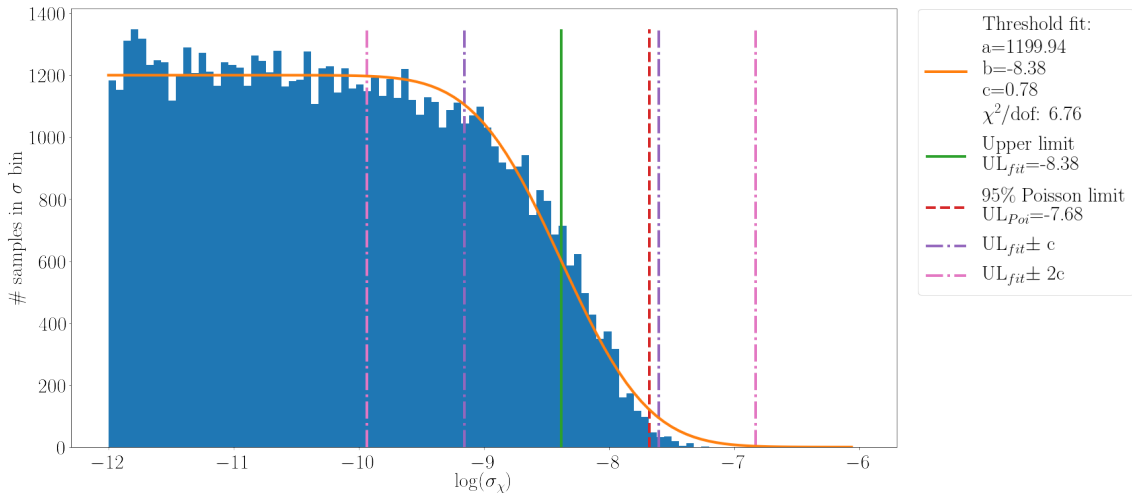
Figure C.10.: Cross-section distribution and threshold fit for the WIMP mass slice between 2817-3198 GeV.
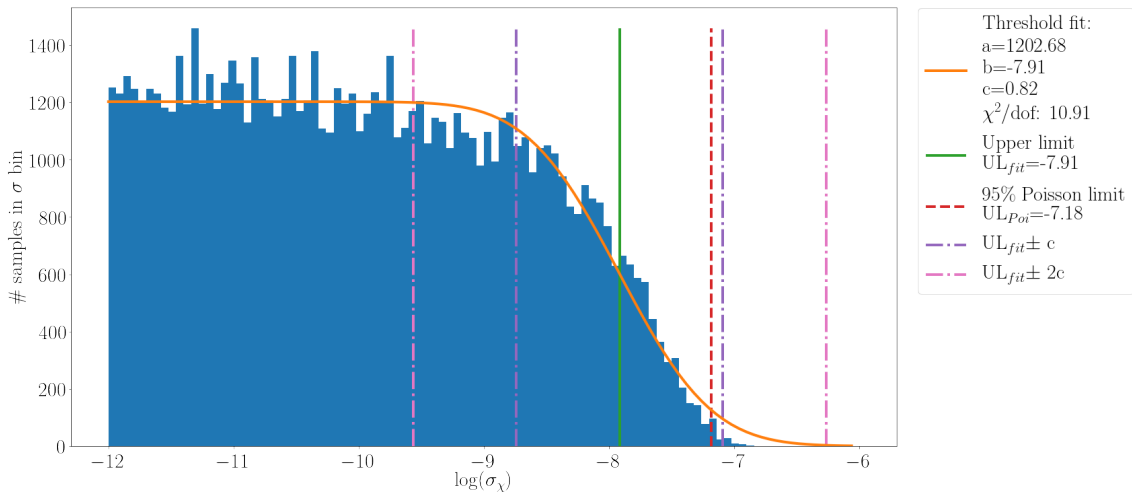
Figure C.11.: Cross-section distribution and threshold fit for the WIMP mass slice between 8810-10000 GeV.

C.2. Using the Fermi-Dirac function
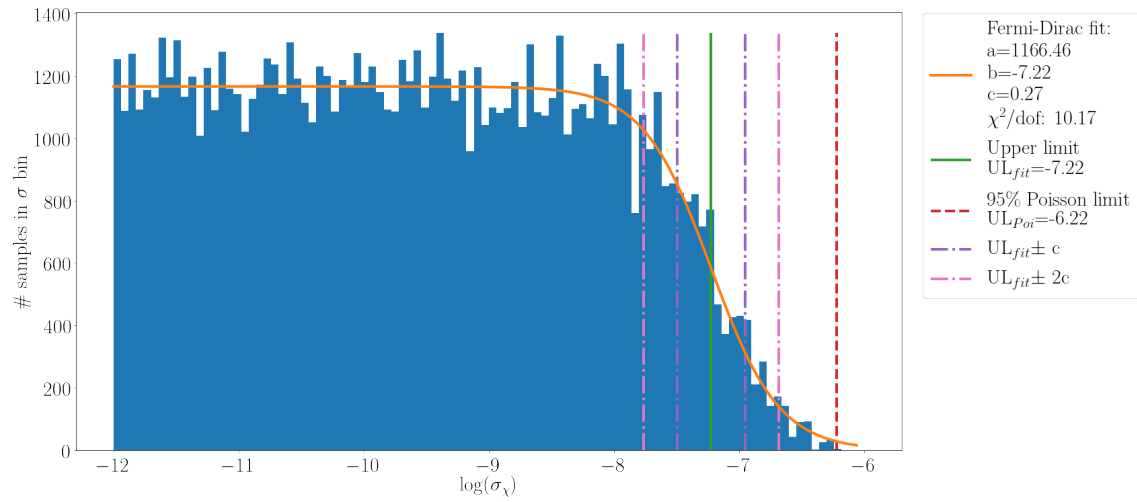
Figure C.12.: Cross-section distribution and threshold fit for the WIMP mass slice between 5-5.7 GeV.
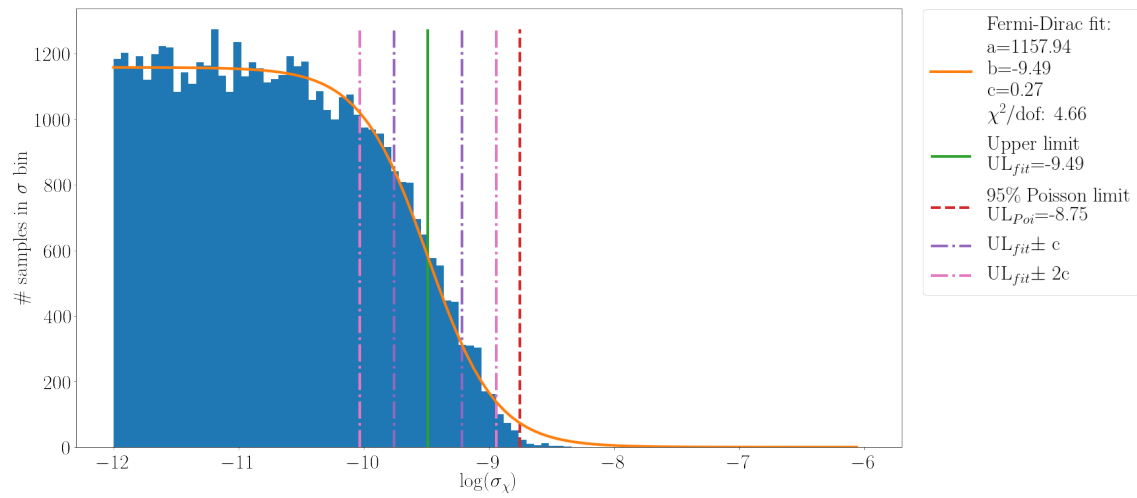
Figure C.13.: Cross-section distribution and threshold fit for the WIMP mass slice between 18-20 GeV.
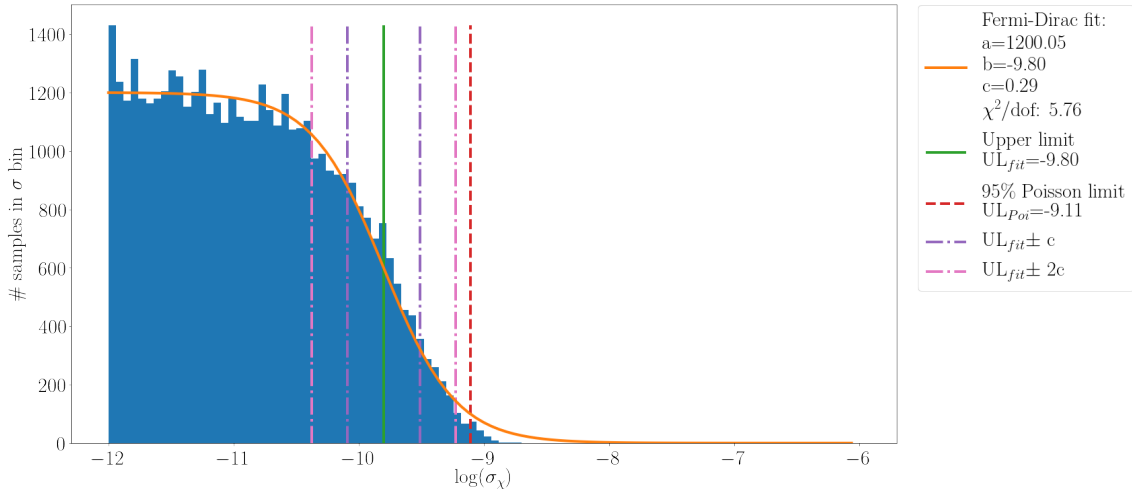
Figure C.14.: Cross-section distribution and threshold fit for the WIMP mass slice between 63-72 GeV.
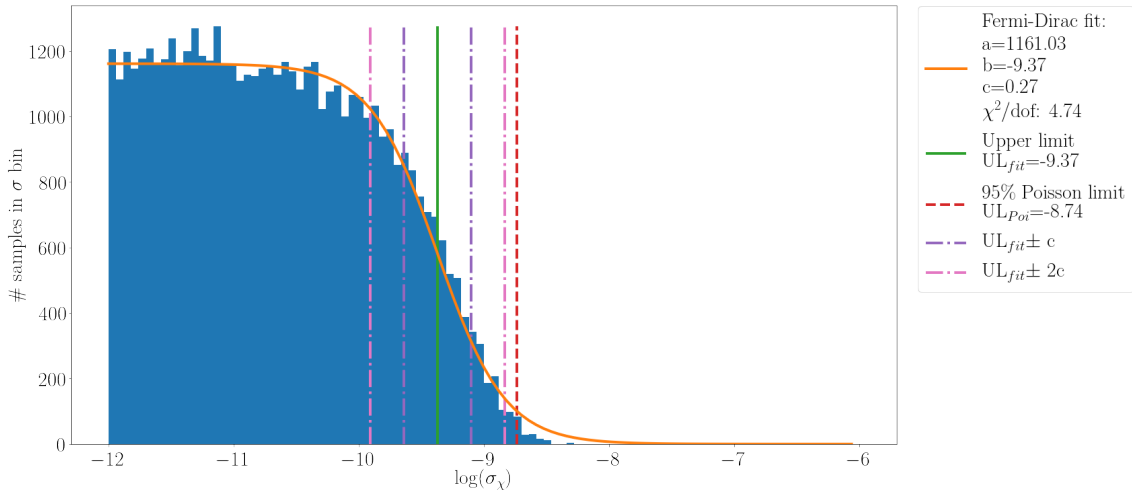
Figure C.15.: Cross-section distribution and threshold fit for the WIMP mass slice between 224-254 GeV.
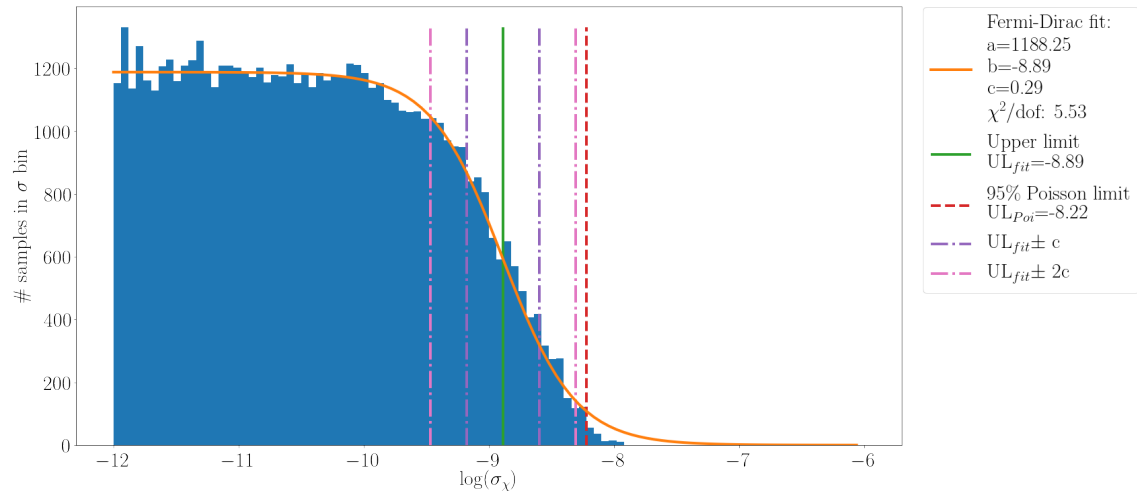
Figure C.16.: Cross-section distribution and threshold fit for the WIMP mass slice between 794-901 GeV.
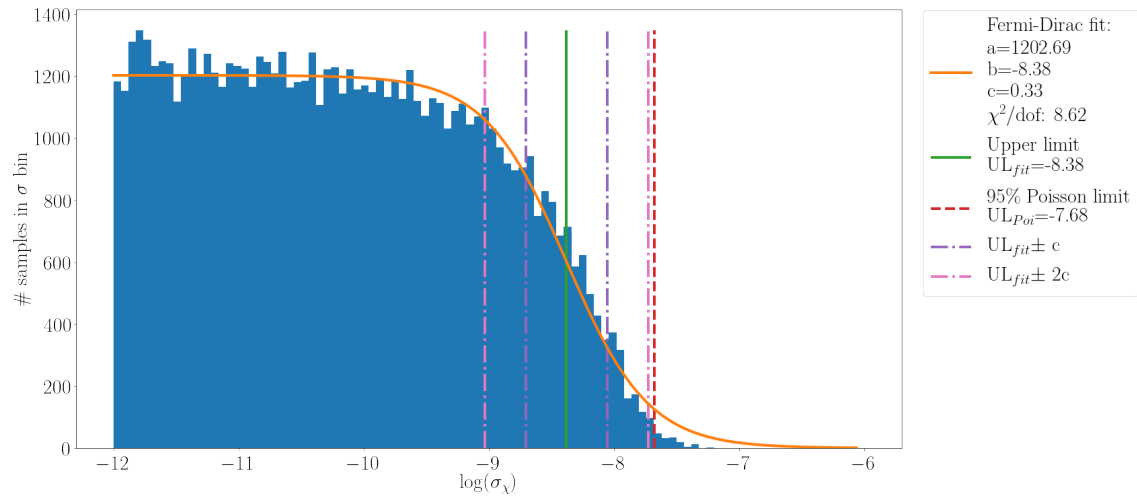
Figure C.17.: Cross-section distribution and threshold fit for the WIMP mass slice between 2817-3198 GeV.
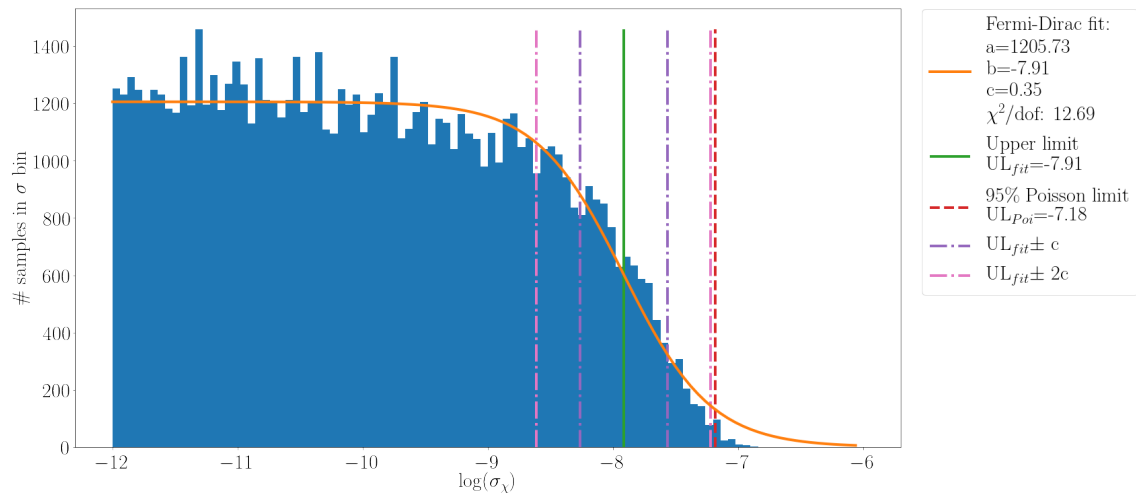
Figure C.18.: Cross-section distribution and threshold fit for the WIMP mass slice between 8810-10000 GeV.

D. Additional coverage plots
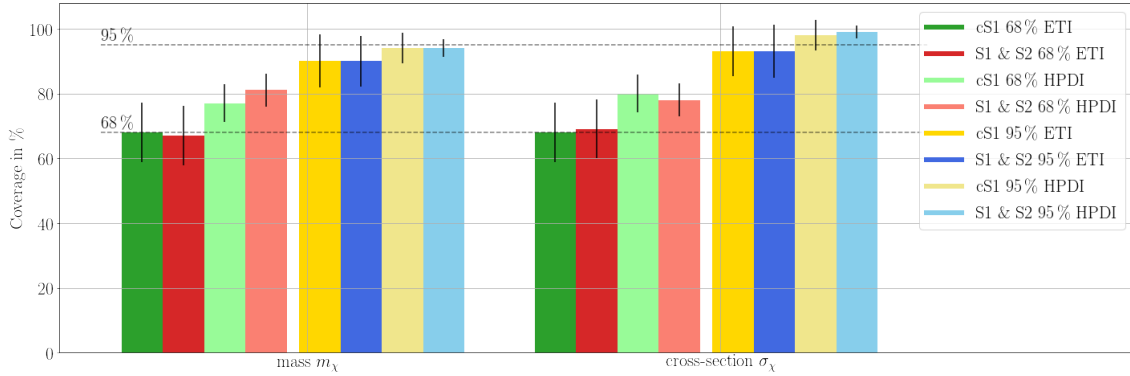
Figure D.19.: Coverage of the WIMP mass m_χ=50 GeV (left) and the WIMP-nucleus cross-section $\sigma_\chi = 1 \times 10^{-8}$ pb (right) for different analysed configurations. The green and red bars compare the performance of the old (green) and new (red) models for the 68 % coverage, while the colour saturation differentiates the methods used to calculate the coverage ,i. e. the pale colours mark the highest posterior density interval (HPDI) and the full saturated colours mark the equally tailed interval (ETI). The same has also been done for the 95 % coverage, see the yellow and blue bars which again compares the old and new model coverage performance. The saturation in colours, like before, marks the different methods of coverage. Overall the new model outperforms the old model also in coverage.

Figure D.20.: Coverage of the WIMP mass m_χ=50 GeV (left) and the WIMP-nucleus cross-section $\sigma_\chi = 8 \times 10^{-9}$ pb (right) for different analysed configurations. The green and red bars compare the performance of the old (green) and new (red) models for the 68 % coverage, while the colour saturation differentiates the methods used to calculate the coverage ,i. e. the pale colours mark the highest posterior density interval (HPDI) and the full saturated colours mark the equally tailed interval (ETI). The same has also been done for the 95 % coverage, see the yellow and blue bars which again compares the old and new model coverage performance. The saturation in colours, like before, marks the different methods of coverage. Overall the new model outperforms the old model also in coverage.

Figure D.21.: Coverage of the WIMP mass m_χ=20 GeV (left) and the WIMP-nucleus cross-section $\sigma_\chi = 1 \times 10^{-8}$ pb (right) for different analysed configurations. The green and red bars compare the performance of the old (green) and new (red) models for the 68 % coverage, while the colour saturation differentiates the methods used to calculate the coverage ,i. e. the pale colours mark the highest posterior density interval (HPDI) and the full saturated colours mark the equally tailed interval (ETI). The same has also been done for the 95 % coverage, see the yellow and blue bars which again compares the old and new model coverage performance. The saturation in colours, like before, marks the different methods of coverage. Overall the new model outperforms the old model also in coverage.

List of Abbreviations

CDM   Cold Dark Matter

CL   Confidence Limit

CMB   Cosmic Microwave Background

DAQ   Data Acquisition

DM   Dark Matter

ETI   Equally Tailed Interval

HAX   Handy Analysis for Xenon

HDM   Hot Dark Matter

HPD   Highest Posterior Density

HPDI   Highest Posterior Density Interval

ΛCDM Λ-Cold Dark Matter

LSP   Lightest Supersymmetric Particle

LXe   liquid Xenon

MACHO   Massive Astrophysical Compact Halo Object

MCMC   Markov Chain Monte Carlo

MOND   MOdified Newtonian Dynamics

MSE   Mean Squared Error

PAX   Processor for Analysing Xenon

pdf   probability density function

pe   photo electrons

PL   Profile Likelihood

PMT   Photomultiplier Tube

PTR   Pulse Tube Refrigerator

QCD   Quantum Chromo Dynamics

RLCE   Relative Light Collection Efficiency

RMS   Root Mean Square

SHM   Standard Halo Model

SM   Standard Model

SPE   single photo electron

SUSY   Supersymmetry

TPC   Time Projection Chamber

WDM   Warm Dark Matter

WIMP   Weakly Interacting Massive Particle

List of Figures

List of Tables

Bibliography

[1] J. Aalbers. *Dark matter search with XENON1T*. en. 9789462339842, 2018. ISBN: 978-94-6233-984-2 (cit. on pp. 32, 39–41, 57, 65, 71, 115).

[2] Jelle Aalbers. *Single electrons in XENON1T*. Internal note. June 2016. URL: `https://xe1t-wiki.lngs.infn.it/doku.php?id=xenon:xenon1t:aalbers:first_single_electrons` (cit. on p. 60).

[3] P. a. R. Ade et al. "Planck 2013 results. XV. CMB power spectra and likelihood". en. In: *Astronomy & Astrophysics* 571 (Nov. 2014), A15. ISSN: 0004-6361, 1432-0746. DOI: `10.1051/0004-6361/201321573` (cit. on pp. ix, xi, 5).

[4] Christophe Andrieu et al. "An Introduction to MCMC for Machine Learning". en. In: *Machine Learning* 50.1 (Jan. 2003), pp. 5–43. ISSN: 1573-0565. DOI: `10.1023/A:1020281327116` (cit. on pp. 51–53).

[5] E. Aprile et al. "The XENON100 Dark Matter Experiment". In: *Astropart.Phys.* 35 (2012), pp. 573–590 (cit. on pp. 23, 33, 34).

[6] E. Aprile and T. Doke. "Liquid xenon detectors for particle physics and astrophysics". In: *Reviews of Modern Physics* 82.3 (July 2010), pp. 2053–2097. DOI: `10.1103/RevModPhys.82.2053` (cit. on p. 28).

[7] E. Aprile et al. "Analysis of the XENON100 dark matter search data". In: *Astroparticle Physics* 54.Supplement C (Feb. 2014), pp. 11–24. ISSN: 0927-6505. DOI: `10.1016/j.astropartphys.2013.10.002` (cit. on pp. 29, 31, 102).

[8] E. Aprile et al. "Conceptual design and simulation of a water Cherenkov muon veto for the XENON1T experiment". en. In: *Journal of Instrumentation* 9.11 (2014), P11006. ISSN: 1748-0221. DOI: `10.1088/1748-0221/9/11/P11006` (cit. on p. 34).

[9] E. Aprile et al. "Dark Matter Search Results from a One Ton-Year Exposure of XENON1T". en. In: *Physical Review Letters* 121.11 (Sept. 2018), p. 111302. ISSN: 0031-9007, 1079-7114. DOI: `10.1103/PhysRevLett.121.111302`. URL: `https://link.aps.org/doi/10.1103/PhysRevLett.121.111302` (visited on 04/10/2020) (cit. on pp. 41–43, 102).

[10] E. Aprile et al. "Lowering the radioactivity of the photomultiplier tubes for the XENON1T dark matter experiment". en. In: *The European Physical Journal C* 75.11 (Nov. 2015), p. 546. ISSN: 1434-6052. DOI: `10.1140/epjc/s10052-015-3657-5` (cit. on p. 35).

[11] E. Aprile et al. "Observation and applications of single-electron charge signals in the XENON100 experiment". en. In: *Journal of Physics G: Nuclear and Particle Physics* 41.3 (2014), p. 035201. ISSN: 0954-3899. DOI: `10.1088/0954-3899/41/3/035201` (cit. on pp. 60, 81).

[12] E. Aprile et al. "Performance of a cryogenic system prototype for the XENON1T Detector". In: *JINST* 7 (2012), P10001. DOI: `10.1088/1748-0221/7/10/P10001` (cit. on p. 36).

[13] E. Aprile et al. "Physics reach of the XENON1T dark matter experiment." en. In: *Journal of Cosmology and Astroparticle Physics* 2016.04 (2016), p. 027. ISSN: 1475-7516. DOI: `10.1088/1475-7516/2016/04/027` (cit. on p. 32).

[14] E. Aprile et al. "Simultaneous Measurement of Ionization and Scintillation from Nuclear Recoils in Liquid Xenon for a Dark Matter Experiment". In: *Physical Review Letters* 97.8 (Aug. 2006), p. 081302. DOI: `10.1103/PhysRevLett.97.081302` (cit. on pp. 28, 74).

[15] E. Aprile et al. "The XENON1T dark matter experiment". en. In: *The European Physical Journal C* 77.12 (Dec. 2017), p. 881. ISSN: 1434-6044, 1434-6052. DOI: `10.1140/epjc/s10052-017-5326-3`. URL: `http://link.springer.com/10.1140/epjc/s10052-017-5326-3` (visited on 04/10/2020) (cit. on pp. 23, 25, 27, 36–38).

[16] E. Aprile et al. "The XENON1T data acquisition system". en. In: *Journal of Instrumentation* 14.07 (July 2019), P07016–P07016. ISSN: 1748-0221. DOI: `10.1088/1748-0221/14/07/P07016`. (Visited on 12/01/2019) (cit. on pp. 39, 57).

[17] Kenath Arun, S. B. Gudennavar, and C. Sivaram. "Dark matter, dark energy, and alternate models: A review". In: *Advances in Space Research* 60.1 (July 2017). arXiv: 1704.06155, pp. 166–186. ISSN: 02731177. DOI: `10.1016/j.asr.2017.03.043` (cit. on p. 8).

[18] ATLAS Collaboration et al. "Search for new phenomena in final states with an energetic jet and large missing transverse momentum in pp collisions at sqrt(s)=13 TeV using the ATLAS detector". In: *Physical Review D* 94.3 (Aug. 2016), p. 032005. DOI: `10.1103/PhysRevD.94.032005` (cit. on p. 22).

[19] ATLAS Collaboration et al. "The ATLAS Experiment at the CERN Large Hadron Collider". In: *Journal of Instrumentation* 3.08 (Aug. 2008), S08003–S08003. ISSN: 1748-0221. DOI: `10.1088/1748-0221/3/08/S08003` (cit. on p. 22).

[20] P. Barrow et al. "Qualification tests of the R11410-21 photomultiplier tubes for the XENON1T detector". en. In: *Journal of Instrumentation* 12.01 (2017), P01024. ISSN: 1748-0221. DOI: `10.1088/1748-0221/12/01/P01024` (cit. on pp. 32, 35).

[21] K. G. Begeman, A. H. Broeils, and R. H. Sanders. "Extended rotation curves of spiral galaxies - Dark haloes and modified dynamics". In: *Monthly Notices of the Royal Astronomical Society* 249 (Apr. 1991), pp. 523–537 (cit. on p. 4).

[22] J. D. Bekenstein and R. H. Sanders. "A Primer to Relativistic MOND Theory". en. In: *EAS Publications Series* 20 (), pp. 225–230. ISSN: 1633-4760, 1638-1963. DOI: 10.1051/eas:2006075 (cit. on p. 9).

[23] Gianfranco Bertone and Dan Hooper. "History of dark matter". en. In: *Reviews of Modern Physics* 90.4 (Oct. 2018), p. 045002. ISSN: 0034-6861, 1539-0756. DOI: 10.1103/RevModPhys.90.045002. URL: https://link.aps.org/doi/10.1103/RevModPhys.90.045002 (visited on 04/10/2020) (cit. on pp. 9, 13).

[24] Gianfranco Bertone, Dan Hooper, and Joseph Silk. "Particle dark matter: evidence, candidates and constraints". en. In: *Physics Reports* 405.5-6 (Jan. 2005), pp. 279–390. ISSN: 0370-1573. DOI: 10.1016/j.physrep.2004.08.031 (cit. on p. 14).

[25] William M. Bolstad. *Introduction to Bayesian Statistics*. John Wiley & Sons, Apr. 2004. ISBN: 978-0-471-27020-1 (cit. on pp. 45, 47, 48).

[26] Adam Brown. *S2AreaFractionTop*. Feb. 2018. URL: https://xe1t-wiki.lngs.infn.it/doku.php?id=xenon:xenon1t:analysis:firstresults:s2_aft_cut_summary (cit. on p. 62).

[27] T. Bruch et al. "Detecting the Milky Way's Dark Disk". In: *The Astrophysical Journal* 696.1 (2009), p. 920 (cit. on p. 15).

[28] Dalong Cheng, M.-C. Chu, and Jiayu Tang. "Cosmological structure formation in Decaying Dark Matter models". en. In: *Journal of Cosmology and Astroparticle Physics* 2015.07 (2015), p. 009. ISSN: 1475-7516. DOI: 10.1088/1475-7516/2015/07/009 (cit. on p. 8).

[29] Andrea Cherubini and Angelo Bifone. "Hyperpolarised xenon in biology". en. In: *Progress in Nuclear Magnetic Resonance Spectroscopy* 42.1 (June 2003), pp. 1–30. ISSN: 0079-6565. DOI: 10.1016/S0079-6565(02)00052-3. URL: http://www.sciencedirect.com/science/article/pii/S0079656502000523 (visited on 12/01/2019) (cit. on p. 24).

[30] Dominick Cichon. *Xenon afterpulses visible in background data*. Internal note. June 2016. URL: https://xe1t-wiki.lngs.infn.it/doku.php?id=xenon:xenon1t:analysis:dominick:xenon1t_xenon_afterpulses.html (cit. on p. 61).

[31] Douglas Clowe et al. "A Direct Empirical Proof of the Existence of Dark Matter". en. In: *The Astrophysical Journal Letters* 648.2 (2006), p. L109. ISSN: 1538-4357. DOI: 10.1086/508162 (cit. on p. 9).

[32] CMS Collaboration et al. "Search for dark matter produced with an energetic jet or a hadronically decaying W or Z boson at sqrt(s)=13 TeV". en. In: *Journal of High Energy Physics* 2017.7 (July 2017), p. 14. ISSN: 1029-8479. DOI: 10.1007/JHEP07(2017)014 (cit. on p. 22).

[33] CMS Collaboration et al. "Search for dijet resonances in proton–proton collisions at s=13TeV and constraints on dark matter and other models". In: *Physics Letters B* 769 (June 2017), pp. 520–542. ISSN: 0370-2693. DOI: 10.1016/j.physletb. 2017.02.012 (cit. on p. 22).

[34] CMS Collaboration et al. "The CMS experiment at the CERN LHC". In: *Journal of Instrumentation* 3.08 (Aug. 2008), S08004–S08004. ISSN: 1748-0221. DOI: 10.1088/ 1748-0221/3/08/S08004 (cit. on p. 22).

[35] COBE/FIRAS. *Far infrared absolute pectrophotometer*. URL: https://lambda. gsfc.nasa.gov/product/cobe/about_firas.cfm (cit. on p. 5).

[36] Matthew Colless et al. "The 2dF Galaxy Redshift Survey: spectra and redshifts". en. In: *Monthly Notices of the Royal Astronomical Society* 328.4 (Dec. 2001), pp. 1039–1063. ISSN: 0035-8711. DOI: 10.1046/j.1365-8711.2001.04902.x (cit. on p. 9).

[37] Daniel Coderre, Cyril Grognon, and Christopher Tunnel. *XENON1T/Kodiaq: Production Release*. Nov. 2016. URL: https://zenodo.org/record/165486# .WZWplidLdhE (cit. on p. 37).

[38] Frederik Michel Dekking et al. "Efficiency and mean squared error". In: *A Modern Introduction to Probability and Statistics: Understanding Why and How*. Ed. by Frederik Michel Dekking et al. London: Springer London, 2005, pp. 299–311. ISBN: 978-1-84628-168-6. DOI: 10.1007/1-84628-168-7_20. URL: https://doi. org/10.1007/1-84628-168-7_20 (cit. on p. 104).

[39] P. S. Bhupal Dev, Anupam Mazumdar, and Saleh Qutub. "Constraining non-thermal and thermal properties of Dark Matter". English. In: *Frontiers in Physics* 2 (2014). ISSN: 2296-424X. DOI: 10.3389/fphy.2014.00026 (cit. on p. 12).

[40] Scott Dodelson and Lawrence M. Widrow. "Sterile Neutrinos as Dark Matter". In: *Physical Review Letters* 72.1 (Jan. 1994). arXiv: hep-ph/9303287, pp. 17–20. ISSN: 0031-9007. DOI: 10.1103/PhysRevLett.72.17 (cit. on p. 13).

[41] Albert Einstein. "LENS-LIKE ACTION OF A STAR BY THE DEVIATION OF LIGHT IN THE GRAVITATIONAL FIELD". In: *Science* 84.2188 (Dec. 1936), p. 506. DOI: 10.1126/science.84.2188.506 (cit. on p. 5).

[42] ESA and the Planck Collaboration. *A portrait of the cosmos as a young Universe*. Dec. 2017. URL: http://sci.esa.int/planck/53103-planck-cosmology/ (cit. on p. 7).

[43] B S Everitt and A Skrondal. *The Cambridge Dictionary of Statistics*. ISBN: 978-0-511-78827-7 (cit. on p. 52).

[44] C. H. Faham et al. "Measurements of wavelength-dependent double photoelectron emission from single photons in VUV-sensitive photomultiplier tubes". en. In: *Journal of Instrumentation* 10.09 (2015), P09010. ISSN: 1748-0221. DOI: 10.1088/ 1748-0221/10/09/P09010 (cit. on pp. 32, 33).

[45]   Jonathan L. Feng. "Dark matter at the Fermi scale". en. In: *Journal of Physics G: Nuclear and Particle Physics* 32.1 (2006), R1. ISSN: 0954-3899. DOI: 10.1088/0954-3899/32/1/R01 (cit. on p. 12).

[46]   Stephen E. Fienberg. "When did Bayesian inference become "Bayesian"?" EN. In: *Bayesian Analysis* 1.1 (Mar. 2006), pp. 1–40. ISSN: 1936-0975, 1931-6690. DOI: 10.1214/06-BA101 (cit. on p. 45).

[47]   Daniel Foreman-Mackey et al. "emcee: The MCMC Hammer". en. In: *Publications of the Astronomical Society of the Pacific* 125.925 (Feb. 2013), p. 306. ISSN: 1538-3873. DOI: 10.1086/670067 (cit. on pp. 56, 96).

[48]   C.s. Frenk and S.d.m. White. "Dark matter and cosmic structure". en. In: *Annalen der Physik* 524.9-10 (Oct. 2012), pp. 507–534. ISSN: 1521-3889. DOI: 10.1002/andp.201200212 (cit. on p. 8).

[49]   R. Gavazzi et al. "The Sloan Lens ACS Survey. IV. The Mass Density Profile of Early-Type Galaxies out to 100 Effective Radii". In: *The Astrophysical Journal* 667 (Sept. 2007), pp. 176–190. DOI: 10.1086/519237 (cit. on pp. 5, 9).

[50]   Margaret J. Geller and John P. Huchra. "Mapping the Universe". en. In: *Science* 246.4932 (Nov. 1989), pp. 897–903. ISSN: 0036-8075, 1095-9203. DOI: 10.1126/science.246.4932.897 (cit. on p. 9).

[51]   Andrew Gelman et al. *Bayesian Data Analysis, Third Edition*. en. Google-Books-ID: eSHSBQAAQBAJ. CRC Press, Nov. 2013. ISBN: 978-1-4398-9820-8 (cit. on p. 46).

[52]   Charles J. Geyer. "Practical Markov Chain Monte Carlo". EN. In: *Statistical Science* 7.4 (Nov. 1992), pp. 473–483. ISSN: 0883-4237, 2168-8745. DOI: 10.1214/ss/1177011137 (cit. on p. 50).

[53]   Gerd Gigerenzer et al. *The Empire of Chance: How Probability Changed Science and Everyday Life*. Apr. 1989. DOI: 10.1017/CBO9780511720482 (cit. on p. 45).

[54]   Jonathan Goodman and Jonathan Weare. "Ensemble samplers with affine invariance". In: *Communications in Applied Mathematics and Computational Science* 5.1 (Jan. 2010), pp. 65–80. ISSN: 2157-5452. DOI: 10.2140/camcos.2010.5.65 (cit. on pp. 54–56).

[55]   Francis Halzen and Dan Hooper. "The indirect search for dark matter with Ice-Cube". en. In: *New Journal of Physics* 11.10 (2009), p. 105019. ISSN: 1367-2630. DOI: 10.1088/1367-2630/11/10/105019 (cit. on p. 22).

[56]   W.K. Hastings. "Monte Carlo sampling methods using Markov chains and their applications." In: *Biometrika* 57 (1970), pp. 97–109 (cit. on p. 52).

[57]   Richard H. Helm. "Inelastic and Elastic Scattering of 187-Mev Electrons from Selected Even-Even Nuclei". In: *Physical Review* 104.5 (Dec. 1956), pp. 1466–1475. DOI: 10.1103/PhysRev.104.1466 (cit. on p. 19).

[58] G. Hinshaw et al. "Nine-year Wilkinson Microwave Anisotropy Probe (WMAP) Observations: Cosmological Parameter Results". en. In: *The Astrophysical Journal Supplement Series* 208.2 (2013), p. 19. ISSN: 0067-0049. DOI: 10.1088/0067-0049/208/2/19 (cit. on p. 5).

[59] Alejandro Ibarra, David Tran, and Christoph Weniger. "Indirect searches for decaying dark matter". In: *International Journal of Modern Physics A* 28.27 (Oct. 2013), p. 1330040. ISSN: 0217-751X. DOI: 10.1142/S0217751X13300408 (cit. on p. 22).

[60] J. Aalbers et al. *PAX: Raw Data Processor*. Apr. 2018. URL: https://github.com/XENON1T/pax (cit. on pp. 40, 57, 59).

[61] Gerard Jungman, Marc Kamionkowski, and Kim Griest. "Supersymmetric dark matter". In: *Physics Reports* 267.5 (Mar. 1996), pp. 195–373. ISSN: 0370-1573. DOI: 10.1016/0370-1573(95)00058-5 (cit. on p. 12).

[62] T. Lasserre and EROS Collaboration. "Not enough stellar Mass Machos in the Galactic Halo". In: *arXiv:astro-ph/0002253* (Feb. 2000). arXiv: astro-ph/0002253 (cit. on p. 11).

[63] J.D. Lewin and P.F. Smith. "Review of mathematics, numerical factors, and corrections for dark matter experiments based on elastic nuclear recoil". In: *Astroparticle Physics* 6.1 (1996), pp. 87–112 (cit. on p. 14).

[64] *LNGS overview*. en-gb. URL: https://www.lngs.infn.it/en/lngs-overview (cit. on p. 35).

[65] LUX Collaboration et al. "Results from a Search for Dark Matter in the Complete LUX Exposure". In: *Physical Review Letters* 118.2 (Jan. 2017), p. 021303. DOI: 10.1103/PhysRevLett.118.021303 (cit. on p. 43).

[66] A. Manzur et al. "Scintillation efficiency and ionization yield of liquid xenon for monoenergetic nuclear recoils down to 4 keV". In: *Physical Review C* 81.2 (Feb. 2010), p. 025808. DOI: 10.1103/PhysRevC.81.025808 (cit. on pp. 26, 81).

[67] Darryl Masson. *S1AreaFractionTop cut*. Mar. 2017. URL: https://xe1t-wiki.lngs.infn.it/doku.php?id=xenon:xenon1t:darryl:xe1t_s1_aft_map (cit. on p. 61).

[68] Wes McKinney. "Data Structures for Statistical Computing in Python". In: *Proceedings of the 9th Python in Science Conference*. Ed. by Stéfan van der Walt and Jarrod Millman. 2010, pp. 51–56 (cit. on p. 59).

[69] Y. Mei. "Direct Dark Matter Search with the XENON100 Experiment". PhD thesis. Rice University, Apr. 2011. URL: http://xenon.physik.uni-mainz.de/mainzTheses/Thesis_YuanMei201105.pdf (cit. on p. 17).

[70] P. Meszaros. "The behaviour of point masses in an expanding cosmological substratum". In: *Astronomy and Astrophysics* 37 (Dec. 1974), pp. 225–228. ISSN: 0004-6361 (cit. on p. 7).

[71] M. Milgrom. "A modification of the Newtonian dynamics as a possible alternative to the hidden mass hypothesis". In: *Astrophysical Journal* 270 (July 1983), pp. 365–370 (cit. on p. 9).

[72] *MongoDB for GIANT Ideas.* URL: https://www.mongodb.com/index (cit. on p. 37).

[73] S. A. Murphy and A. W. Van Der Vaart. "On Profile Likelihood". In: *Journal of the American Statistical Association* 95.450 (June 2000), pp. 449–465. ISSN: 0162-1459. DOI: 10.1080/01621459.2000.10474219. URL: https://www.tandfonline.com/doi/abs/10.1080/01621459.2000.10474219 (cit. on p. 47).

[74] Travis E. Oliphant. *Guide to NumPy.* 2nd. USA: CreateSpace Independent Publishing Platform, 2015. ISBN: 978-1-5173-0007-4 (cit. on p. 96).

[75] PandaX-II Collaboration et al. "Dark Matter Results from 54-Ton-Day Exposure of PandaX-II Experiment". In: *Physical Review Letters* 119.18 (Oct. 2017), p. 181302. DOI: 10.1103/PhysRevLett.119.181302 (cit. on p. 43).

[76] R. D. Peccei and Helen R. Quinn. "Constraints imposed by CP conservation in the presence of pseudoparticles". In: *Physical Review D* 16.6 (Sept. 1977), pp. 1791–1797. DOI: 10.1103/PhysRevD.16.1791 (cit. on p. 13).

[77] A. A. Penzias and R. W. Wilson. "Determination of the Microwave Spectrum of Galactic Radiation". en. In: *The Astrophysical Journal* 146 (Dec. 1966), p. 666. ISSN: 0004-637X. DOI: 10.1086/148944 (cit. on p. 5).

[78] Jaques Pienaar. *S1SingleScatter cut.* Jan. 2018. URL: https://xe1t-wiki.lngs.infn.it/doku.php?id=xenon:xenon1t:jacques:s1_single_scatter_cut_sr1 (cit. on p. 61).

[79] Planck Collaboration et al. "Planck 2015 results. XIII. Cosmological parameters". In: *Astronomy & Astrophysics* 594 (Oct. 2016). arXiv: 1502.01589, A13. ISSN: 0004-6361, 1432-746. DOI: 10.1051/0004-6361/201525830 (cit. on pp. 6–8, 11).

[80] *RabbitMQ - Messaging that just works.* URL: https://www.rabbitmq.com/ (cit. on p. 39).

[81] Leslie J Rosenberg and Karl A. van Bibber. "Searches for invisible axions". In: *Physics Reports* 325.1 (Feb. 2000), pp. 1–39. ISSN: 0370-1573. DOI: 10.1016/S0370-1573(99)00045-9 (cit. on p. 14).

[82] V. C. Rubin and Jr. W. K. Ford. "Rotation of the Andromeda Nebula from a Spectroscopic Survey of Emission Regions". In: *Astrophysical Journal* 159 (Feb. 1970), p. 379 (cit. on p. 3).

[83] V. C. Rubin, W. K. Ford Jr., and N. Thonnard. "Rotational properties of 21 SC galaxies with a large range of luminosities and radii, from NGC 4605 /R = 4kpc/ to UGC 2885 /R = 122 kpc/". In: *Astrophys. J.* 238 (June 1980), pp. 471–487. DOI: 10.1086/158003 (cit. on p. 4).

[84] Chris Savage, Katherine Freese, and Paolo Gondolo. "Annual modulation of dark matter in the presence of streams". In: *Physical Review D* 74.4 (Aug. 2006), p. 043531. DOI: 10.1103/PhysRevD.74.043531 (cit. on p. 16).

[85] Schindler, Stefan. "Bayesian approach to the analysis of XENON100 data". Diploma Thesis. Mainz: Johannes Gutenberg-Universität, June 2013 (cit. on pp. 20, 21).

[86] Peter Sorensen. "Anisotropic diffusion of electrons in liquid xenon with application to improving the sensitivity of direct dark matter searches". In: *Nuclear Instruments and Methods in Physics Research Section A: Accelerators, Spectrometers, Detectors and Associated Equipment* 635.1 (Apr. 2011), pp. 41–43. ISSN: 0168-9002. DOI: 10.1016/j.nima.2011.01.089 (cit. on p. 62).

[87] Volker Springel, Carlos S. Frenk, and Simon D. M. White. *The large-scale structure of the Universe*. En. Special Features. Apr. 2006. DOI: 10.1038/nature04805 (cit. on pp. 9, 10).

[88] G Steigman. "Cosmology Confronts Particle Physics". In: *Annual Review of Nuclear and Particle Science* 29.1 (Dec. 1979), pp. 313–338. ISSN: 0163-8998. DOI: 10.1146/annurev.ns.29.120179.001525 (cit. on p. 12).

[89] Louis E. Strigari. "Galactic searches for dark matter". In: *Physics Reports*. Galactic searches for dark matter 531.1 (Oct. 2013), pp. 1–88. ISSN: 0370-1573. DOI: 10.1016/j.physrep.2013.05.004 (cit. on p. 21).

[90] *The XENON Experiment | Enlightening the Dark*. en-US. URL: www.xenon1t.org (cit. on p. 23).

[91] The XENON100 Collaboration et al. "Dark Matter Results from 100 Live Days of XENON100 Data". In: *Physical Review Letters* 107.13 (Sept. 2011), p. 131302. DOI: 10.1103/PhysRevLett.107.131302 (cit. on pp. 76, 78, 79).

[92] P. Tisserand et al. "Limits on the Macho Content of the Galactic Halo from the EROS-2 Survey of the Magellanic Clouds". In: *Astronomy & Astrophysics* 469.2 (July 2007). arXiv: astro-ph/0607207, pp. 387–404. ISSN: 0004-6361, 1432-0746. DOI: 10.1051/0004-6361:20066017 (cit. on p. 11).

[93] Teresa Marrodán Undagoitia and Ludwig Rauch. "Dark matter direct-detection experiments". en. In: *Journal of Physics G: Nuclear and Particle Physics* 43.1 (2016), p. 013001. ISSN: 0954-3899. DOI: 10.1088/0954-3899/43/1/013001 (cit. on pp. 14, 15, 21).

[94] Steven Weinberg. "A New Light Boson?" In: *Physical Review Letters* 40.4 (Jan. 1978), pp. 223–226. DOI: 10.1103/PhysRevLett.40.223 (cit. on p. 14).

[95] Christian Weinheimer. "The neutrino mass direct measurements". In: *arXiv:hep-ex/0306057* (June 2003). arXiv: hep-ex/0306057 (cit. on p. 13).

[96] *Welcome to processor for Analyzing XENON1T's documentation! — Processor for Analyzing XENON1T 6.9.0 documentation*. URL: http://xenon1t.github.io/pax/ (cit. on p. 59).

[97] F. Wilczek. "Problem of Strong P and T Invariance in the Presence of Instantons". In: *Physical Review Letters* 40.5 (Jan. 1978), pp. 279–282. DOI: `10.1103/PhysRevLett.40.279` (cit. on p. 14).

[98] Julien Wulf. *PreS2Junk Cut for sciencerun0*. Feb. 2017. URL: `https://xe1t-wiki.lngs.infn.it/doku.php?id=xenon:xenon1t:yuehuan:analysis:0sciencerun_signal_noise` (cit. on p. 62).

[99] Julien Wulf. *PreS2Junk Cut for sciencerun1*. Oct. 2017. URL: `https://xe1t-wiki.lngs.infn.it/doku.php?id=xenon:xenon1t:julien:analysis:sciencerun1:s1_noise_cut` (cit. on p. 62).

[100] XENON Collaboration et al. "XENON100 dark matter results from a combination of 477 live days". In: *Physical Review D* 94.12 (Dec. 2016), p. 122001. DOI: `10.1103/PhysRevD.94.122001` (cit. on p. 33).

[101] XENON100 Collaboration et al. "Dark Matter Results from 225 Live Days of XENON100 Data". In: *Physical Review Letters* 109.18 (Nov. 2012), p. 181301. DOI: `10.1103/PhysRevLett.109.181301` (cit. on pp. 74, 76, 78, 82).

[102] Tianyu Zhu, Jelle Aalbers, and Yuehuan Wei. *S2Width cut*. Nov. 2017. URL: `https://xe1t-wiki.lngs.infn.it/doku.php?id=xenon:xenon1t:sim:notes:tzhu:width_cut_tuning#toy_fax_simulation` (cit. on p. 62).